ACS Catalysis

pubs.acs.org/acscatalysis Review

Electrocatalysis of Single-Atom Sites: Impacts of Atomic Coordination

Bingzhang Lu,† Qiming Liu,† and Shaowei Chen*

Cite This: *ACS Catal.* 2020, 10, 7584–7618 Read Online

ACCESS | Metrics & More | Article Recommendations | Supporting Information

ABSTRACT: Single metal atoms embedded within select supporting matrices have shown great potential in the development of high-efficiency, low-cost electrocatalysts because of maximal atom utilization and mass activity. As the single metal atoms are stabilized by coordination bonds with the substrate, the strong metal–support interactions can be exploited for ready manipulation of the electrocatalytic activity and selectivity toward target reactions. However, most single-atom catalysts (SACs) are prepared by pyrolysis and contain a wide range of coordination structures. Resolving the atomic configurations of the metal coordination moieties represents a critical first step in the establishment of an unambiguous correlation between the SAC structure and activity. In this Review, we summarize recent progress in the studies of single-atom electrocatalysts, with a focus on the impacts of the coordination structure of the single-atom sites on the electrocatalytic activities toward a series of reactions that are important for various electrochemical energy technologies, such as hydrogen evolution reaction, oxygen evolution reaction, oxygen reduction reaction, nitrogen reduction reaction, CO_2 reduction reaction, and so on. The survey entails a wide range of SACs, from noble metals (e.g., Pt, Pd, Ru, Ir, Au, etc.) to non-noble metals (e.g., Fe, Co, Ni, Cu, etc.), supported on a variety of substrate materials (e.g., pristine and doped carbon, metal, metal oxide, metal sulfide, etc.). Finally, the Review concludes with a perspective highlighting the promises and challenges in the further development of SACs within the context of coordination chemistry.

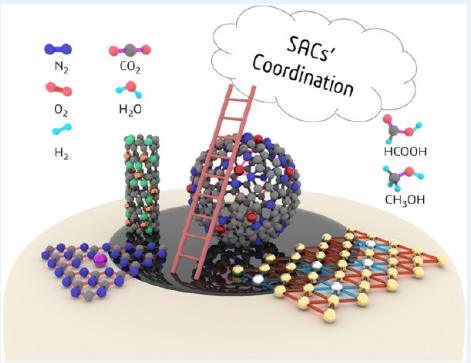

KEYWORDS: *single-atom catalyst, coordination moiety, atomic configuration, electrocatalytic activity, noble metal, non-noble metal*

1. INTRODUCTION

Development of new, sustainable energy technologies represents an important mission of modern chemistry, as manifested by the extensive interest in fuel cells, metal–air batteries, water electrolyzers, artificial carbon and nitrogen fixation, and so on.[1,2] The operation of these technologies all require appropriate advanced electrocatalysts,[3−5] and transition metals have been used extensively as the leading catalysts toward the wide range of important electrochemical reactions involved, such as hydrogen evolution reaction (HER), oxygen reduction reaction (ORR), oxygen evolution reaction (OER), formic acid oxidation reaction (FAOR), methanol oxidation reaction (MOR), nitrogen reduction reaction (NRR), carbon dioxide reduction reaction (CO_2RR), and so on.[6−11] The most commonly used electrocatalysts are based on noble metal nanoparticles, such as Pt, Pd, Ru, Au, Rh, and Ir. However, despite their apparent activity, their high costs and low natural abundance significantly hamper the commercialization process.[12] One intuitive strategy to mitigate such issues is to reduce the size of the nanoparticles and hence the costs of the catalysts, as the bulk atoms are not directly involved in the reactions, and single-atom catalysts (SACs) represent the ultimate solution.[13,14] Indeed, SACs have been attracting a great deal of attention because of their maximal atom utilization and, more importantly, unprecedented activity and selectivity toward various reactions.[15,16]

SACs are generally stabilized within a support matrix involving an unsaturated coordination configuration,[17,18] which allows the binding of reaction intermediates and facilitates the catalytic reactions. Yet the plentiful variations of the coordination structures inevitably influence the binding energy of reaction intermediates, leading to a dramatic difference of the electrocatalytic activity.[19−23] In addition, the strong metal–support interaction (SMSI) is maximal in SACs,[24,25] where the activity of the metal sites may be enhanced by the supporting substrate, and concurrently, additional contributions may arise from the neighboring atoms of the substrate.[26] Both of these vary with the exact coordination configurations surrounding the metal sites.

Some of these results have been highlighted in several recent review articles.[14,27−33] Herein, we will summarize recent

Received: April 30, 2020
Revised: June 10, 2020
Published: June 11, 2020

https://dx.doi.org/10.1021/acscatal.0c01950
ACS Catal. 2020, 10, 7584–7618

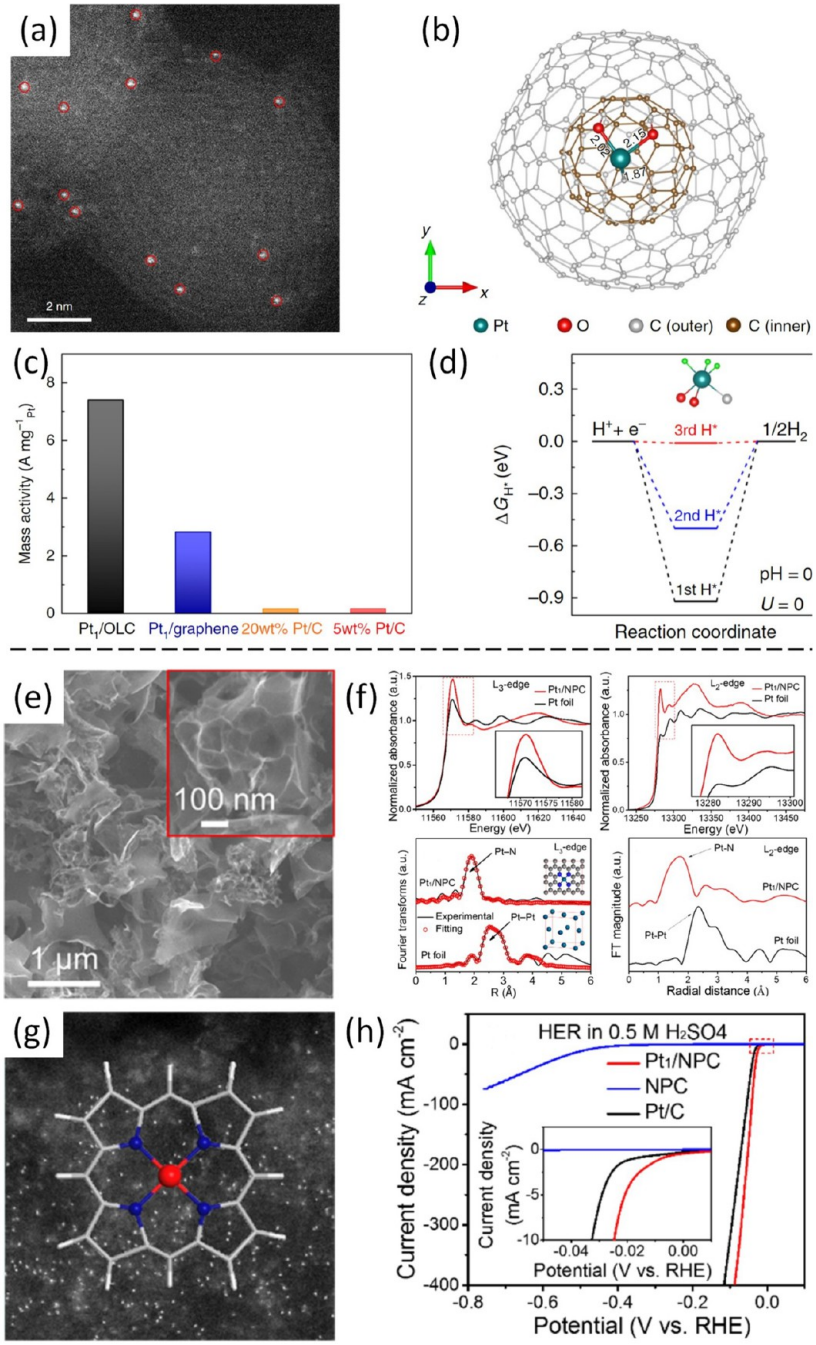

Figure 1. (a) HAADF-STEM image of Pt_1/OLC with Pt single atoms identified by the red circles. (b) Optimized atomic model of PtO_2C_{295}. (c) Comparison of mass activity of Pt_1/OLC with other samples at the overpotential of −38 mV. (d) Calculated free-energy diagram of HER. Inset shows the model of H adsorption on the Pt SA site. (e) SEM image of Pt_1/NPC. Inset is a high-resolution image. (f) XAS spectra of Pt_1/NPC. (g) HAADF-STEM image of Pt_1/NPC, with a proposed structure of the active site. (h) HER polarization curves of Pt_1/NPC. Inset is the zoom in at potential close to zero. Panels a−d are adapted with permission from ref 44. Copyright 2019 Springer Nature. Panels e−h are adapted with permission from ref 38. Copyright 2018 American Chemical Society.

progress of SAC electrocatalysis with a specific focus on the impact of the atomic coordinating structure on the electrocatalytic activity and selectivity. We will survey a range of SACs (including both noble metals and non-noble metals) that are anchored on different substrates, such as metals, metal (hydro)oxides, metal sulfides, metal phosphides, (pristine or doped) carbon, MXene, among others, involving different coordination configurations (e.g., M−M_x, M−C_x, M−O_x, M−S_x, M−P_x, M−N_x, M−C_xN_y, etc.). Careful correlation between the activity and the atomic coordination yields fundamental insights that are critical in the rational design and engineering of high-performance catalysts toward a wide range of reactions. Within this context, a perspective is also included to highlight the challenges and strategies in future research.

2. NOBLE METALS

The immediate benefits of noble metal SACs are the minimal cost and maximal mass activity due to maximum atom utilization. In addition, the electrocatalytic activity may be significantly enhanced, as compared with the nanoparticle or

https://dx.doi.org/10.1021/acscatal.0c01950
ACS Catal. 2020, 10, 7584−7618

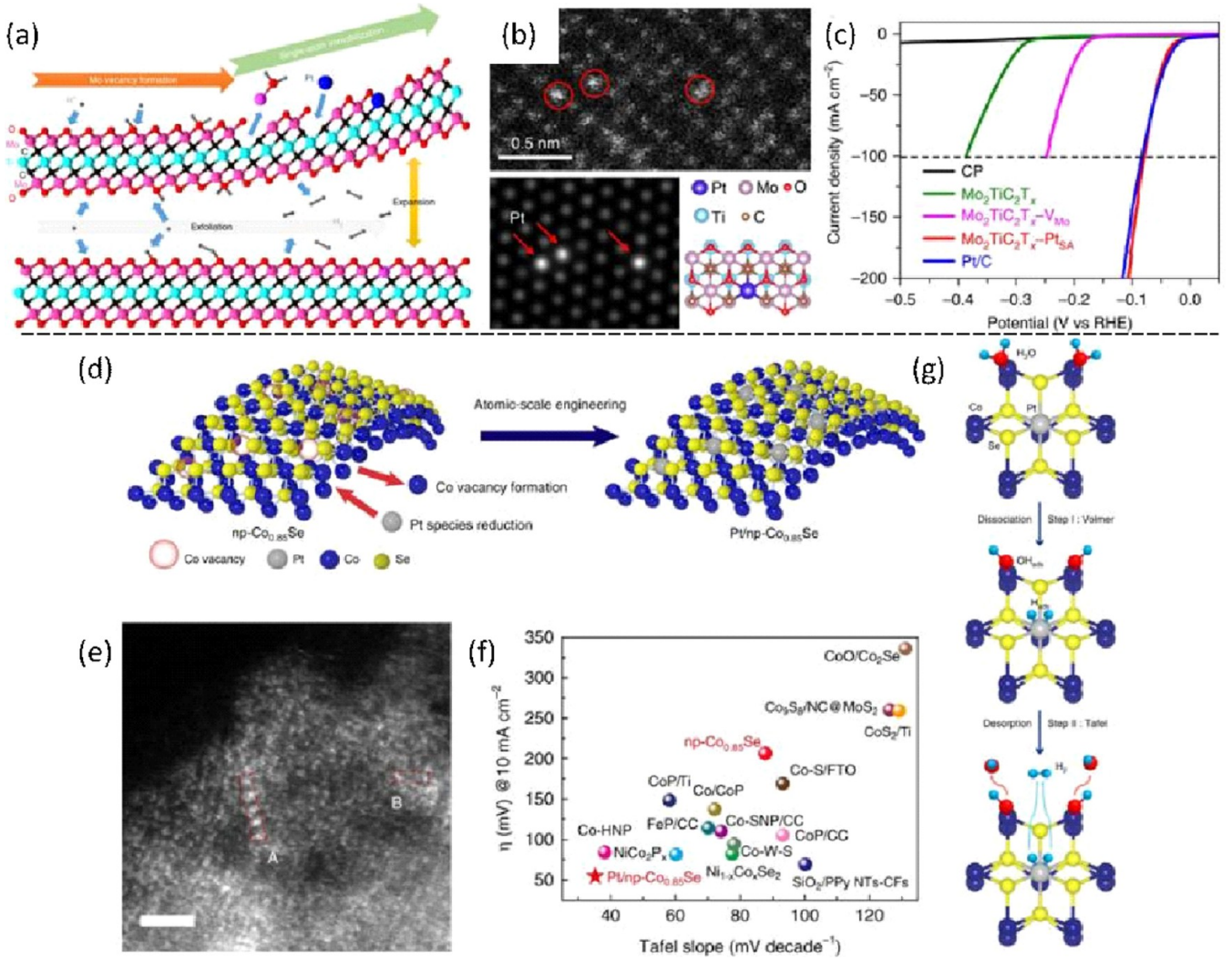

Figure 2. (a) Schematic illustration of the synthesis of $Mo_2TiC_2T_x$-Pt_{SA} for HER. (b) HAADF-STEM images of $Mo_2TiC_2T_x$-PtSA and proposed coordination structure. (c) HER polarization of $Mo_2TiC_2T_x$-Pt_{SA}. (d) Schematic illustration of the fabrication procedure of Pt/np-$Co_{0.85}Se$. (e) HAADF-STEM image of Pt/np-$Co_{0.85}Se$. (f) HER activity of Pt/np-$Co_{0.85}Se$ in comparison to relevant results in the literature. (g) HER mechanism determined by in situ XAS analysis. Panels a–c are adapted with permission from ref 48. Panels d–g are adapted with permission from ref 54. Copyright 2018–2019 Springer Nature.

bulk forms. For instance, Pt SACs have been found to exhibit remarkable activity toward HER, H_2O_2 production, and FAOR; Ru SACs are active for HER, OER, and NRR; Ir SACs can catalyze OER; Au SACs can serve as NRR catalysts and assist in HER and OER; and Rh SACs are effective catalysts for FAOR. Notably, the electrocatalytic activity depends sensitively on the coordination configuration, which may explain some of the conflicting results reported in the literature.

2.1. Pt SACs. Pt SACs have been found to exhibit apparent electrocatalytic activity toward a range of important reactions (except for OER[34]). Below is a survey of the latest progress.

2.1.1. HER. The most prominent application of Pt SACs is for HER.[35,36] The typical support materials include N- or S-doped carbon, graphitic carbon, graphdiyne, transitional metal oxide, chalcogenide, phosphide, MXene, and metal nanoparticle. Accordingly, Pt SAs are coordinated with different atoms within the supporting matrix. Interestingly, it is consistently observed that the coordination of Pt with atoms of high electronegativity leads to a high valence state and enhanced HER performance.[37−39]

Pyrolyzed carbon has been one of the most commonly used substrates to anchor Pt SAs for HER[40−42] because of ready manipulation of the electron density by strong interfacial interaction, high electrical conductivity, and ease of synthesis and doping.[12] In one of the first studies of Pt SACs toward HER, Cheng et al.[43] prepared Pt SACs by atomic layer deposition (ALD) and observed a better performance than that of Pt clusters, even though the detailed coordination structure was not fully revealed then. The overpotential ($\eta_{10,HER}$) needed to reach the current density of 10 mA/cm^2 in 0.5 M H_2SO_4 was close to −50 mV for the Pt SACs, comparable to that of Pt clusters and Pt/C, but the mass activity was 7.8 times that of Pt clusters and 37.4 time that of Pt/C. This motivated a number of subsequent studies, and the coordination structure became increasingly clear. For instance, Liu et al.[44] also adopted the ALD method to load Pt SAs onto a pyrolyzed onion-like-carbon support (Pt_1/OLC, Figure 1a). The Pt SAs were found to reside on the surface of a fullerene-like C_{295} cage (Figure 1b), with a tetrahedral coordination configuration of Pt−O_2C_1, according to results from extended X-ray absorption fine structure (EXAFS) analysis. Such a structure was stable

https://dx.doi.org/10.1021/acscatal.0c01950
ACS Catal. 2020, 10, 7584−7618

because of a high diffusion energy (3.2 eV) of Pt atoms by DFT calculations. Moreover, the Pt SAs were positively charged, with a valence state between Pt(0) and Pt(IV). This catalyst showed an apparent HER activity, with $\eta_{10,HER} = -38$ mV and a mass activity 43 times higher than that of commercial Pt/C (Figure 1c). However, it is noticed that the bare surface of Pt−O_2C_1 was inert for HER because of a very negative adsorption energy of H (ΔG_H, Figure 1d). However, the ΔG_H of the adsorption of the third H was very close to 0 (Figure 1d). This suggests that the actual active site was $H_2PtO_2C_1$. Another noticeable factor is the out-of-plane geometric arrangement of the Pt atoms. Such a structure with a strong local electric field can promote proton mass transfer. In another study, Yin et al.[37] adopted the impregnation-annealing method to load Pt SAs onto graphdiyne. The best sample showed a Pt coordination structure of Pt−C_2Cl_2, in which the Pt 5d orbitals had a high unoccupied density of state (DOS). Similarly, Ji et al.[45] loaded Pt atoms onto multiwall carbon nanotubes via an irradiation method, where the positively charged Pt atoms were bonded to four oxygen atoms connected to the nanotube. All these samples show apparent HER activity in an acid electrolyte.

In addition to pristine carbon, heteroatom-doped carbon has also been widely used to anchor metal single atoms. Notably, binding of heteroatoms to Pt SAs can influence the electronic structure of the metal sites and increase the Pt valence state, which is in favor of the HER process. For instance, within a pyrolyzed carbon structure, nitrogen dopants are believed to enhance the stability of Pt SAs through Pt−N coordination bonds. In an early study, Li et al.[38] synthesized Pt SACs on nitrogen-doped carbon by UV radiation, which was denoted as Pt_1/NPC (Figure 1e). Results from X-ray photoelectron spectroscopy (XPS) and X-ray absorption spectroscopy (XAS) measurements suggest a square-planar-type Pt−N_4 structure (Figure 1f,g) and the pyridine-type Pt−N_4 (normal Pt−N_4) was the major structure in the catalyst, instead of pyrrolic Pt−N_4 (Stone−Wales Pt−N_4), because of a lower binding energy as well as a better consistency of the bond length between experiment and theory of the former structure. Furthermore, because of charge transfer from Pt to the coordinated N atoms, the resulting vacancy of the Pt 5d orbits induced efficient H adsorption and high stability of the Pt SAs, a key factor of the excellent HER performance. Experimentally, the HER mass activity was 16-fold greater than that of commercial Pt/C at −0.025 V in 0.5 M H_2SO_4, and $\eta_{100,HER}$ shifted only by 1 mV after 3000 test cycles.

S-doped carbon has also been used to stabilize Pt SAs, where the HER activity is ascribed to the relatively high valence state of Pt SAs by charge transfer from Pt to S. Yet the HER activity of Pt−S_4 moiety is not as good as that of Pt nanoclusters.[46] Interestingly, unlike most SACs, the Pt−S coordinate structure shows unique CO resistance during alkaline HER.[47] Kwon et al.[47] showed that Pt^{2+} centers embedded in S-doped carbon formed a Pt−S_4 structure, with two strong Pt−S bonds and two labile ones. During alkaline HER, CO or H_2O would replace the labile S to form a tetrahedral Pt−X_2S_2 (X = H_2O or CO) structure. Unlike most metal active sites (bulk materials or single atoms) that are prone to CO poisoning, the alkaline HER activity of the Pt−S_4 moiety became unexpectedly promoted by CO adsorption. This was ascribed to the CO-terminated Pt that had a higher valence state because CO worked like a π-acceptor and withdrew electrons from Pt. It is noticeable that this unexpected CO promotion only works for the Pt−S_4 center in alkaline electrolytes, but not in acidic or neutral electrolytes.

Pt SACs supported on other substrates have also been widely used as efficient HER catalysts, such as other noble metals, metal oxides, metal sulfides, metal phosphides, and so on. Similar to Pt SAs supported on heteroatom-doped carbon, an increasing Pt valence state leads to an improved HER activity. Zhang et al.[48] adopted the electrochemical exfoliation method to deposit Pt SAs onto an exfoliated $Mo_2TiC_2T_x$ layer forming a triangular antiprism Pt−C_3O_2 structure in Mo vacancy. The best sample was labeled as $Mo_2TiC_2T_x$-Pt_{SA} (Figure 2a−c). In this sample, Pt SAs were partially positively charged because of charge transfer from Pt to the $Mo_2TiC_2T_x$ nanosheets. This sample exhibited an $\eta_{10,HER}$ of −30 mV in 0.5 M H_2SO_4 and a mass activity 40 times better than that of commercial Pt/C catalyst because of the low ΔG_H on Pt (−0.08 eV) and an improved d-electron domination by Pt atom doping.

Noble metals can also be used as suitable supports of Pt SACs. For example, Zhang et al.[49] adopted ALD to load Pt SAs onto Pd octahedra prepared a priori to form a Pt/Pd single-atom alloy. The resulting sample showed a better specific activity than commercial Pt/C, as well as an ultrahigh mass activity that was 54.6 times higher than the latter in 0.5 M H_2SO_4. EXAFS analysis showed that the Pt atoms were situated on the surface of Pd octahedra, with an average coordination of Pt−$O_{2.5}Pd_{0.8}$. The remarkable HER activity was ascribed to the high unoccupied density of Pt 5d orbitals, consistent with Pt SACs on other supports. In a similar case, Chao et al.[50] load Pt SAs on PdCu nanorings by an ultrasonic bath method. EXAFS measurements showed an average coordination structure of Pt−$Cu_{3.6}Pd_{5.1}O_{1.4}$. These two studies clearly show that Pt SAs on Pd has an HER activity much better than Pd itself and commercial Pt/C in acidic electrolyte.

Metal oxide is another common support material, with the surface oxygen atoms as strong coordination sites to stabilize Pt SAs and induce efficient Pt to O charge transfer. For instance, Liu et al.[39] synthesized Pt SAs on a MoO_3 nanosheet by the formation of Pt−O coordination bonds. With apparent charge transfer from Pt to O, the resulting sample showed an HER activity similar to that of commercial Pt/C in 0.5 M H_2SO_4. In another study, Gao et al.[51] loaded Pt SAs onto CeO_2 nanowires/nanorods by the dealloy method, where Pt SAs were bonded to the oxygen of CeO_2, leading to a remarkable HER activity and stability in 0.5 M H_2SO_4.

Metal sulfides, phosphides, and selenides represent another option of support materials. These substrates alone have been known to have obvious activity toward HER. The rich surface defects can be exploited to stabilize Pt SAs, and the ensuing SMSI effects can lead to enhanced intrinsic activity and hence an overall excellent HER performance. For example, Guan et al.[52] deposited Pt SAs onto MoS_2/NiS_2 heteronanostructures by a calcination method, which showed an excellent HER activity in acid, with an $\eta_{10,HER}$ of −34 mV as well as good stability. The active sites were ascribed to the Pt atoms adsorbed onto the S atoms of the MoS_2 surface. Similarly, Feng et al.[53] synthesized a Pt SAC on a NiS/Al_2O_3 surface and observed a high HER specific activity that was comparable to that of commercial Pt/C. X-ray absorption near-edge spectroscopy (XANES) measurements confirmed the cationic state of the Pt atoms, while EXAFS analyses revealed the formation of Pt−S coordination bonds. DFT calculations suggested that with Pt atoms adsorbed onto the surface of NiS, both Pt and S

https://dx.doi.org/10.1021/acscatal.0c01950
ACS Catal. 2020, 10, 7584−7618

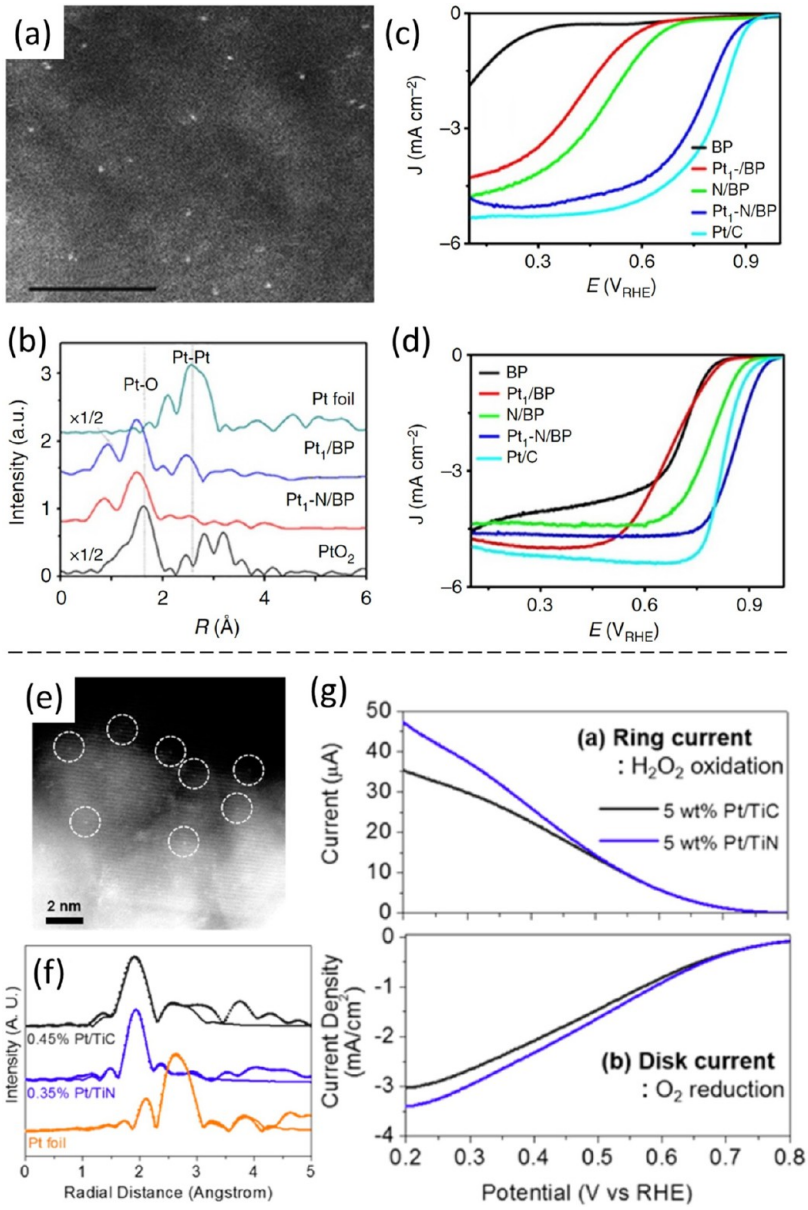

Figure 3. (a) HAADF-STEM image of Pt_1−N/BP. (b) R space FT-EXAFS spectra of Pt_1−N/BP, Pt_1/BP, Pt foil, and PtO_2. RRDE polarization curves of Pt_1−N/BP and control samples in (c) 0.1 M $HClO_4$ and (d) 0.1 M KOH. (e) HAADF-STEM image of 0.2 wt % Pt_1/TiC. (f) FT-EXAFS spectra of Pt/TiC, Pt/TiN and Pt foil. (g) ORR polarization curves of Pt_1/TiC and Pt_1/TiN in 0.1 M $HClO_4$. Panels a−d are adapted with permission from ref 56. Copyright 2017 Springer Nature. Panels e−g are adapted with permission from ref 62. Copyright 2017 American Chemical Society.

of NiS were active toward HER. Moreover, if Pt substituted Ni beneath the surface layer, the surface S sites remained activated. This suggests that the excellent HER performance arose from the Pt−S centers, and the significant synergistic interaction between the Pt SAs and metal sulfide support.

Similar behaviors were observed with metal selenides. Jiang et al.[54] synthesized a Pt SAs/np-$Co_{0.85}S$ nanoporous composite by an electrochemical etching method (Figure 2d−g). During the cyclic process, Co atoms of $Co_{0.85}Se$ were dissolved forming vacancies where Pt atoms were trapped. The Pt SAs were found to be positively charged and coordinated to six Se atoms, forming an octahedral Pt−Se_6 structure. The resulting sample showed an excellent HER activity in neutral electrolyte, with an $\eta_{10,HER}$ of only −55 mV. In situ XAS measurements showed that water molecules were adsorbed on the Co sites and became dissociated into H and OH, which were then bound to Pt and Co atoms, respectively (Volmer reaction); and two H atoms on the Pt site were combined to form H_2 (Tafel reaction). Results from DFT calculations showed a strong charge redistribution after Pt addition into the system. Meanwhile, H adsorption on Pt and Co was very close to that on Pt(111) surface, indicating a synergistic effect of the Pt SA dopants.

Similarly, as one of the best nonprecious metal catalysts for HER, CoP has also been adopted to be a support of Pt SAs to further enhance the performance. Zhang et al.[55] loaded Pt SAs onto a CoP nanotube-Ni foam by an electrochemical potential-cycling method. With positively charged Pt SAs, the resulting samples showed a good HER activity in neutral electrolyte, with a mass activity ca. 4 times that of commercial Pt/C.

https://dx.doi.org/10.1021/acscatal.0c01950
ACS Catal. 2020, 10, 7584−7618

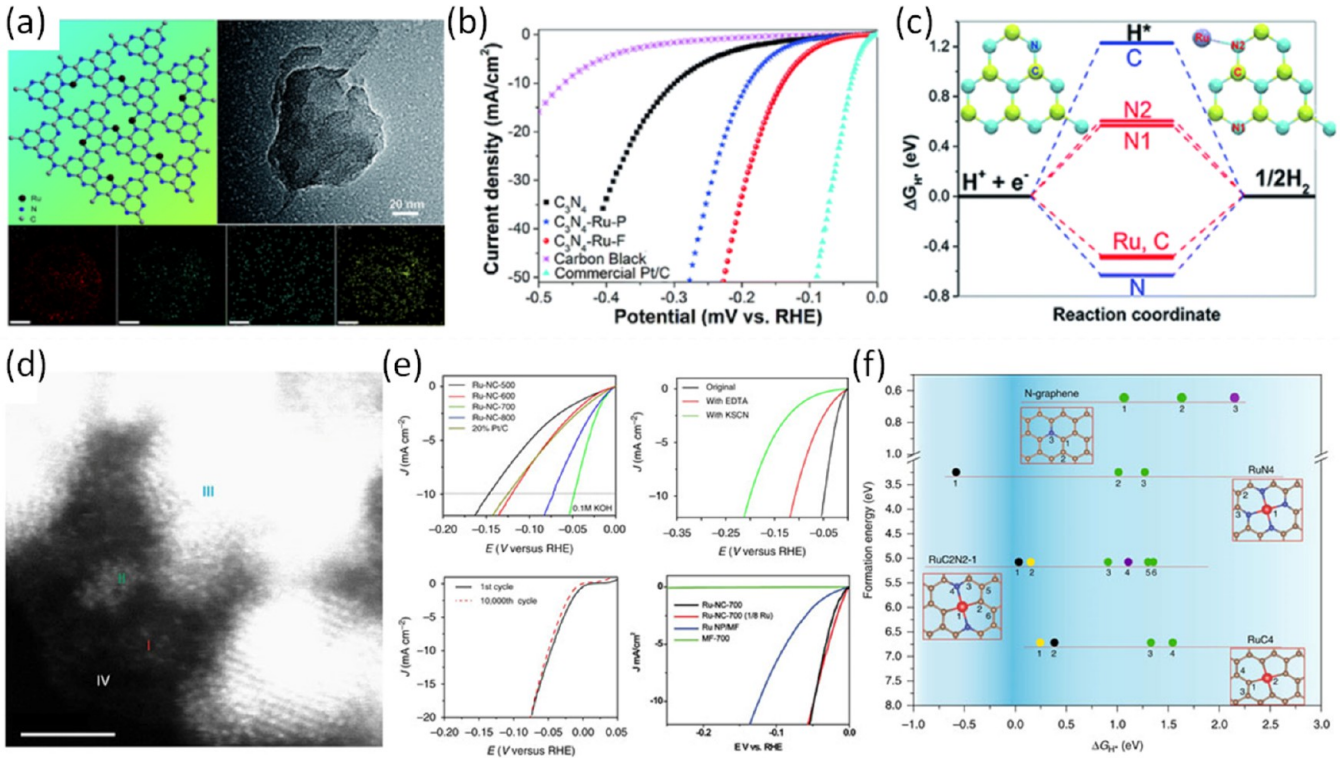

Figure 4. (a) Schematic structure, TEM image and elemental maps of C_3N_4−Ru-F. (b) Polarization curve of HER catalyzed by various samples in 0.5 M H_2SO_4. (c) Calculated Gibbs free energy of HER at equilibrium for different bonding sites in undoped C_3N_4 and C_3N_4−Ru-F. (d) HAADF-STEM image of Ru-NC-700 with both Ru SAs and Ru NPs in nitrogen-doped carbon. The scale bar is 2 nm. Zone I is Ru SAs, zone II is Ru clusters, zone III is Ru nanoparticles, and zone IV is the carbon background. (e) (clockwise) LSV curves of the series of samples in 0.1 M KOH, EDTA and KSCN poisoning tests, stability tests after 10 000 cycles, and control experiments with samples with a lower content of Ru nanoparticles and with Ru nanoparticles alone (no Ru SACs). (f) Energy diagram of RuC_xN_y structure from first principle calculations. Panels a−c are adapted with permission from ref 67. Copyright 2017 Royal Society of Chemistry. Panels d−f are adapted with permission from ref 69. Copyright 2019 Springer Nature.

In summary, Pt SACs can be prepared with a range of supporting substrates for effective HER electrocatalysis in acid and neutral media. The common key factor is that Pt SAs are coordinated to atoms of high electronegativity, which withdraw electrons from the Pt 5d orbitals. For carbon and metal supports, Pt SAs are coordinated with high-electronegativity elements like O, N, or Cl and the coordination structures become the active centers. For metal sulfides, selenides, and phosphides, the Pt-substrate coordination moieties not only serve as the active sites but also activate neighboring atoms of the support materials for additional contributions to the activity. The HER performances of these Pt SACs are also summarized in Table S1.

2.1.2. ORR. ORR is an essential reaction of fuel cells and metal−air batteries. Currently, Pt-based nanoparticles are the catalysts of choice. While development of Pt SACs is seemingly a most promising way to reduce the Pt use by its maximum atomic utilization, most Pt SACs are found to be active for ORR only in alkaline solutions and rarely catalyze $4e^-$ reduction of oxygen, and the active sites remain under debate. In one of the earliest studies, Liu et al.[56] loaded Pt atoms on N-doped carbon by controlled pyrolysis (Figure 3a−d). XAS analyses of the resulting sample, Pt_1−N/BP, showed that the Pt atoms were coordinated with C and N atoms and with a coordination number of 3 and 2, respectively (i.e., Pt−C_3N_2). Electrochemically, Pt_1−N/BP exhibited a high ORR activity with a half-wave potential ($E_{1/2}$) at +0.87 V vs reversible hydrogen electrode (RHE) in 0.1 M KOH, even better than commercial Pt/C. Nevertheless, the ORR performance in 0.1 M $HClO_4$, while one of the best for Pt SACs, was not as good as that of Pt/C, with $E_{1/2}$ = +0.76 V. Note that in this study the ORR in both acidic and alkaline media was argued to proceed via the $4e^-$ pathway, and the sample without Pt−N coordination showed only a low activity. Similarly, Li et al.[38] observed that Pt−N_4 sites were efficient for ORR in alkaline solution, with $E_{1/2}$ = +0.89 V, but exhibited a poor activity in acid, involving $4e^-$ in the former and only $2e^-$ in the latter. In another study, Choi et al.[57] showed that Pt SACs with Pt−S_4 sites were effective for H_2O_2 production in 0.1 M $HClO_4$, with a charge transfer number (n) of 2.1, where the $E_{1/2}$ was as negative as +0.3 V and varied with the concentration of S. They showed that the $2e^-$ pathway, rather than the $4e^-$ one, was kinetically favorable for the Pt−S_4 sites in carbon. However, contradictory results are rampant in the literature. In one study,[58] Pt SACs were found to predominantly catalyze the reduction of oxygen to H_2O_2 even in alkaline solution. In another study,[59] Pt SAs in carbon vacancies forming a Pt−C_4 structure were found to catalyze the $4e^-$ ORR in 0.1 M $HClO_4$ with an activity that was even better than that of Pt/C. Similar results were observed with Pt−N_4 moieties embedded in carbon.[60]

Different from carbon-based Pt SACs, Pt SACs supported on TiC or TiN show a consistently high H_2O_2 yield. Yang et al.[61] prepared Pt SAs (0.35 wt %) onto the surface of TiN by the incipient wetness impregnation method, where the Pt atoms were coordinated to Ti and Cl, with a coordination

https://dx.doi.org/10.1021/acscatal.0c01950
ACS Catal. 2020, 10, 7584−7618

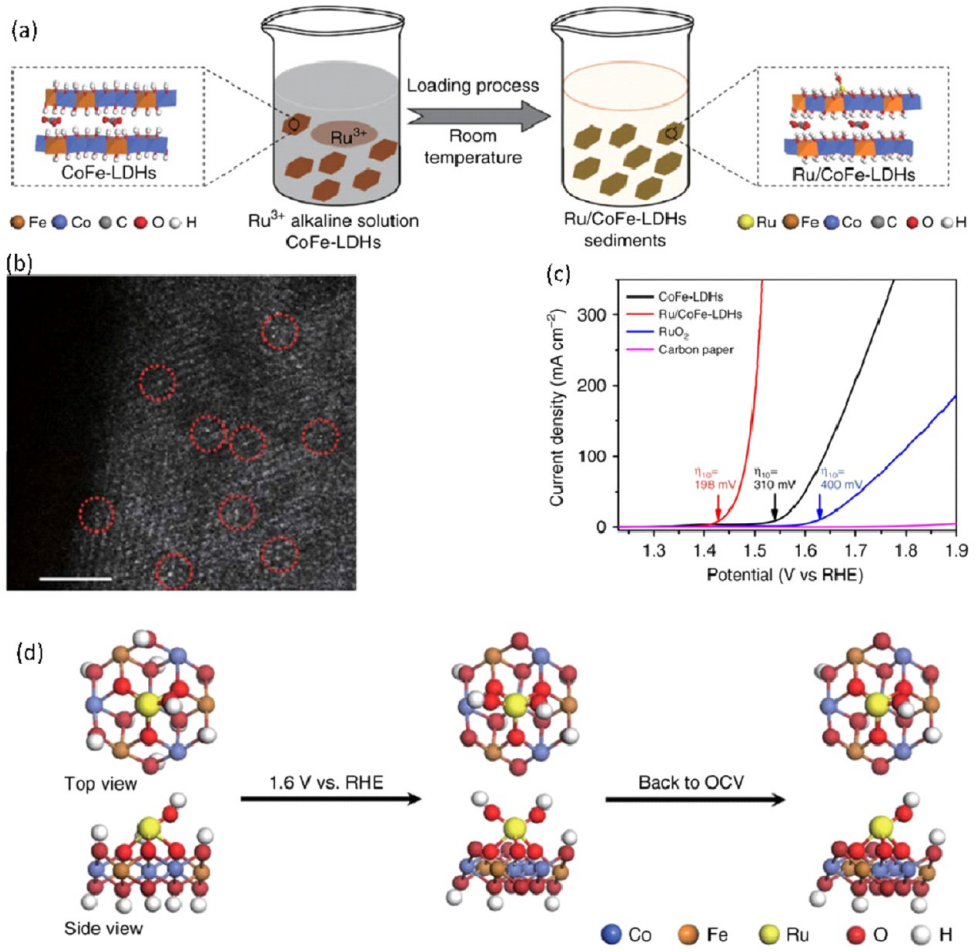

Figure 5. (a) Schematic illustration of the synthesis of Ru/CoFe-LDH catalysts. (b) Cs-corrected STEM image showing atomic dispersion of Ru on the surface of LDHs. (c) LSV curves of Ru/CoFe-LDHs and other control samples in 1 M KOH. (d) Schematic illustration of Ru/CoFe-LDHs during OER based on the results of in situ XAS studies. Adopted with permission from ref 73. Copyright 2019 Springer Nature.

number of 0.573 and 3.038, respectively. The resulting samples exhibited a high H_2O_2 yield in 0.1 M $HClO_4$, with an $E_{1/2}$ as low as +0.6 V. By contrast, for the samples prepared with a high Pt concentration, the formation of Pt nanoparticles led to effective $4e^-$ ORR and a more positive $E_{1/2}$. An even higher H_2O_2 yield was observed with ORR catalyzed by Pt SACs supported on TiC in 0.1 M $HClO_4$,[62] with the Pt atoms involved in a coordination structure of $Pt-Cl_{2.4}Ti_{0.4}$ (Figure 3e–g). Consistently, Kim et al.[63] prepared Pt SACs on Sb-doped SnO_2, where the Pt atoms took the place of Sb, bonded with Sn and O atoms with a coordination number of 2.61 and 0.77, respectively. The resulting samples showed an $E_{1/2}$ of ca. +0.6 V and obvious H_2O_2 yield (20–30%) for ORR in 0.1 M $HClO_4$.

From the results presented above, one can see drastic discrepancy of the ORR performance even for Pt SACs in seemingly similar coordination configurations. It is generally argued that Pt SAs catalyze only the $2e^-$ pathway because of a lack of neighboring bind sites to induce the breaking of the O–O bond. Yet this cannot account for the $4e^-$ ORR behaviors observed in some of the studies, and further in-depth studies, in particular, structural characterizations, are strongly desired. These results are also summarized in Table S2.

2.1.3. Fuel Oxidation. Pt SACs have also shown remarkable electrocatalytic activity for the anodic oxidation of fuel molecules. As mentioned above, Kim et al.[63] prepared Pt SACs supported on Sb-doped SnO_2, with an average Pt coordination of $Pt-Sn_{2.61}O_{0.77}$. In addition to the good ORR activity of H_2O_2 production, the sample also showed high activity toward FAOR with a current density of 3350 A/g at +0.6 V via a direct pathway (direct oxidation of HCOOH to CO_2), while commercial Pt/C followed an indirect pathway (HCOOH first dehydrated to CO_{ads} and then oxidized to CO_2), with a current density of only 180 A/g at +0.6 V. As a comparison, Pt nanoparticles (diameter 3 nm) on the same Sb-doped SnO_2 showed no FAOR activity. By contrast, the Pt SACs showed no activity toward MOR. Consistently, Yang et al.[64] deposited Pt SAs epitaxially on the surface of gold octahedral nanocrystals by an electrochemical method and observed an ultrahigh mass activity for FAOR at 62600 A/g, almost 170 times that of commercial Pt/C (370 A/g). It has been argued that only 1 to 2 Pt atoms are needed for the activation of O–H bond, such that FAOR proceeds via the direct pathway on Pt SACs, whereas Pt ensemble is conducive for the indirect pathway, which facilitates the adsorption of CO intermediate and C–O bond activation. For MOR, as the adsorption of CO intermediate species is inevitable, Pt ensemble is required for MOR. On the contrary, Gao et al.[51] observed a high MOR mass activity with Pt SACs supported on TiO_2 (1184 A/g), almost 5 times that of commercial Pt/C (210 A/g). The discrepancy of the MOR activities by Pt SACs is most likely due to the different coordination configurations.

https://dx.doi.org/10.1021/acscatal.0c01950
ACS Catal. 2020, 10, 7584–7618

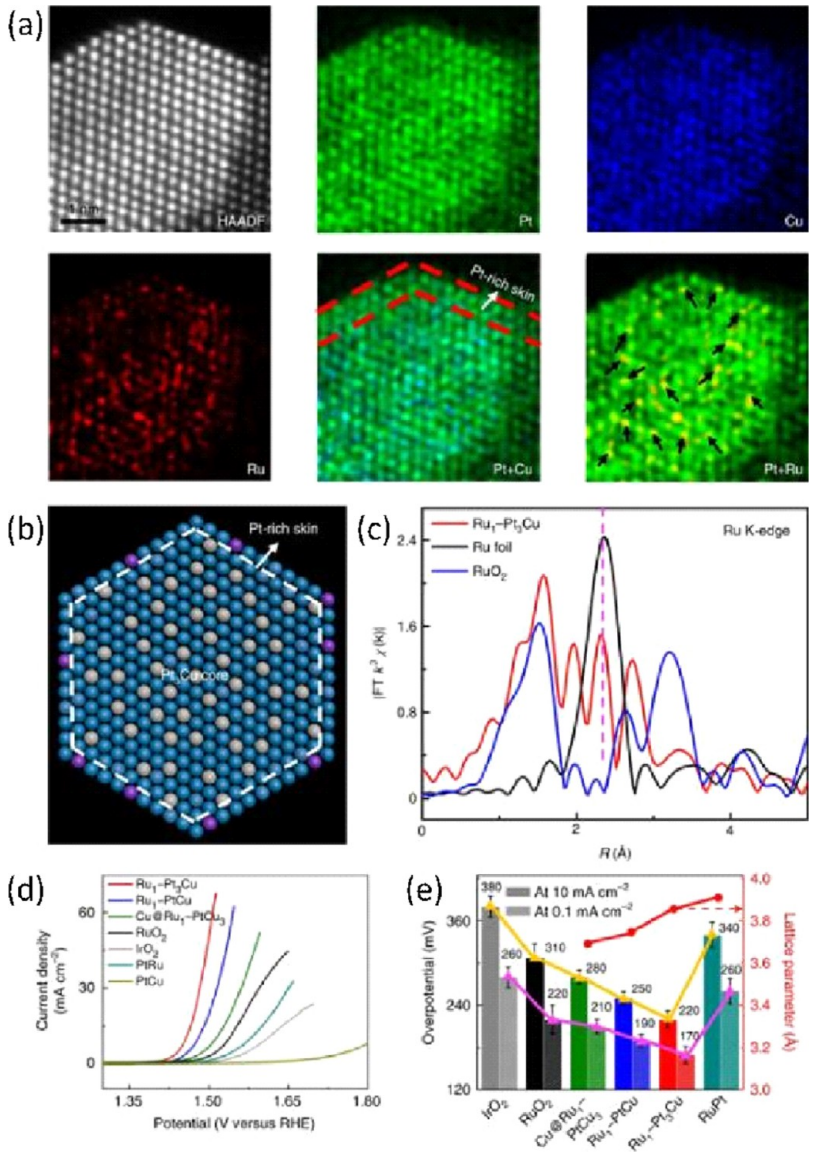

Figure 6. (a) Atomically resolved elemental maps of Ru_1-Pt_3Cu. (b) Schematic atom model. Blue, gray, and purple balls represent Pt, Cu, and Ru, respectively. (c) FT−EXAFS spectra of the Ru K edge of the various samples. (d) LSV curves of Ru_1-Pt_3Cu, Ru_1-PtCu, $Cu@Ru_1-Pt_3Cu$, and other control samples in 0.1 M $HClO_4$. (e) Comparison of the overpotentials to reach 0.1 and 10 mA/cm^2 and lattice parameters for various catalysts. Adopted with permission from ref 75. Copyright 2019 by Springer Nature.

2.2. Ru SACs. Ru SACs have been found to show significant activity toward HER and OER in water splitting, and some even show electrocatalytic activity for NRR and ORR.

2.2.1. HER. Recent years have witnessed rapid development of Ru-based HER catalysts, with excellent activity in a wide range of pH, in particular, in alkaline media. In early studies, Ru embedded in N-doped carbon is shown to have high HER activity.[65,66] However, the activity is mostly attributed to Ru nanoparticles, while the contribution of isolated atoms is unnoticed. In a recent study with Ru(II) ions embedded within a graphitic carbon nitride (g-C_3N_4) matrix forming Ru−N_2 coordination moieties, the resulting Ru SACs exhibited apparent HER activity, with $\eta_{10,HER}$ = −140 mV (Figure 4a−c),[67] which was attributed to the combined contributions of the Ru center and adjacent N and C atoms. Zhang et al.[68] also argued that Ru SAs were responsible for the HER activity observed with pyrolyzed ruthenium−carbon catalysts. In a more recent study, we synthesized N-doped carbon nanowires embedded with both Ru nanoparticles and Ru SAs (Ru-NC-700), and we observed a record-high HER activity in 1 M KOH, with a low $\eta_{10,HER}$ of only −12 mV, markedly better than that of Pt/C (Figure 4d−f).[69] Careful experimental measurements and DFT calculations showed that Ru SAs were the dominant active sites, with minor contributions from Ru nanoparticles. Importantly, results from DFT calculations suggested that the Ru SACs were mostly involved in Ru−C_xN_y coordination, with Ru−C_2N_2 being the most active one, within the context of both H adsorption energies and formation energies.

Ru SAs supported on other support materials also show high HER activity. For instance, Yang et al.[70] deposited Ru SAs onto phosphorus nitride imide nanotubes (PN) by a pyrolysis method. The Ru atoms were coordinated with 4 nitrogen atoms in the PN matrix forming a tetrahedral structure. In such a coordination structure, charge transfer occurred from Ru to

https://dx.doi.org/10.1021/acscatal.0c01950
ACS Catal. 2020, 10, 7584−7618

N, leading to positively charged Ru SAs. The resulting sample showed a high activity in 0.5 M H_2SO_4, with a low $\eta_{10,HER}$ of −24 mV and excellent stability. Ramalingam et al.[71] annealed $RuCl_3$, thiourea and $Ti_3C_2T_x$ MXene to prepare a Ru SAC embedded in N,S-codoped $Ti_3C_2T_x$. XAS analysis showed that the Ru SAs were bonded to the N, S, and S atoms, forming a structure of $Ru-N(O)_3S_1$. HER tests showed an $\eta_{10,HER}$ of −76, −99 and −275 mV in 0.5 M H_2SO_4, 0.5 M NaOH, and 0.5 M Na_2SO_4, respectively. In another study, Zhang et al.[72] deposited Ru SAs onto MoS_2 nanosheets forming Ru−S linkages and observed a high activity in 1 M KOH, with $\eta_{10,HER}$ = −76 mV.

From these studies, one can see that Ru SACs are effective HER catalysts (Table S3). The activity can also be ascribed to the binding of Ru to atoms of high electronegativity (especially nitrogen), which leads to charge redistribution and manipulation of the adsorption of important reaction intermediates.

2.2.2. OER. Ru SACs can also be good OER catalysts. Such Ru SAs are usually coordinated with oxygen atoms and loaded on a substrate of metal (hydro)oxide, metal, or carbon. The most straightforward synthetic strategy is to load Ru SAs on a substrate with a fundamentally high OER activity. Within this context, Fe-, Co-, and Ni-based layered double hydroxides (LDHs) are attractive supports because of their intrinsic OER activity and abundant anchoring sites. For instance, Li et al.[73] adopted a coprecipitation procedure to deposit Ru SAs (0.45 wt %) onto CoFe LDHs, forming Ru−O−M (M = Fe or Co) coordination moieties in the resulting sample Ru/CoFe-LDHs (Figure 5). Specifically, the Ru atoms were located on the sample surface, each bonded to four oxygen atoms with three of the oxygen atoms linked to Fe or Co atoms. The strong electron coupling between Ru and Fe/Co through the O bridge, as manifested by the obvious charge transfer from Co/Fe to Ru, endowed the Ru−O−M structure with a high OER activity, which showed an ultralow overpotential ($\eta_{10,OER}$) of only +198 mV to reach the current density of 10 mA/cm^2 in 1 M KOH. Moreover, this structure also showed marked stability, with no change of the activity after 1000 CV cycles and the dissolved Ru atoms below 0.005 ppb in the solution (in comparison to 53 ppb for commercial RuO_2). In situ XANES measurements showed that the Ru atoms of Ru−O−M maintained an oxidation state lower than 4 without transformation into unstable higher oxidation states. In situ EXAFS measurements showed an obvious shrinkage of the Ru−O−M bond during OER, which further stabilized the Ru atomic structure. Consistent results were obtained in DFT calculations, which showed a much lower *OOH formation energy (the rate determine step) on the Ru sites of Ru−O−M than on the Fe sites of Fe−O−M.

Ru,N-codoped carbon composites also show apparent OER activity. Cao et al.[74] prepared Ru SAs confined in carbon nitride derived N-doped carbon by impregnation of $RuCl_3$ into phosphide carbon nitride followed by controlled pyrolysis. The Ru SAs were in the form of $Ru-N_4$, while the P atoms are not bonded to Ru, only for the enhancement of the electrical conductivity. The resulting nanocomposite showed a high OER activity in 0.5 M H_2SO_4 ($\eta_{10,OER}$ = +267 mV). In situ XAS and SR-FTIR measurements showed that the actual active site was $O-Ru-N_4$, which was further confirmed by DFT calculations.

Ru SACs embedded within a metal matrix represent another unique group of electrocatalysts toward OER. Yao et al.[75] synthesized a series of core−shell $PtCu_x$/Pt structures with Ru SAs incorporated into the surface (Figure 6). The OER activity of the Ru SACs was readily tuned by the lattice strain of the Pt skins induced by the $PtCu_x$ alloy core, as manifested in DFT calculations. The best sample, Ru_1-Pt_3Cu, showed an $\eta_{10,OER}$ of +220 mV in acid, as well as a 10-fold increase of lifetime, as compared with commercial RuO_2. Interestingly, the higher the strain, the better the OER activity. Notably, the oxidation state of Ru SAs remained virtually invariant, as confirmed by in situ XAS studies. This work opens up a new avenue to the design and engineering of the coordination structure of SACs for enhanced catalytic activity.

2.2.3. NRR. Ru SAC also show an excellent activity toward nitrogen reduction for ammonia electrosynthesis. Geng et al.[76] synthesized Ru SACs supported on N-doped carbon by pyrolysis of Ru-containing ZIF-8 derivatives. The Ru SAs are formed in a coordination structure of $Ru-N_4$, and exhibited a record-high NRR activity with an NH_3 yield of 120.9 ug/(mg_{cat}h). At −0.2 V, the Faradaic efficiency was found to reach the astonishing level of 29.6% with a partial current density of 0.13 mA/cm^2. In a later study, Tao et al.[77] pyrolyzed UiO-66 and $RuCl_3$ to prepare Ru SACs supported on ZrO_2 and N-doped carbon. The resulting catalyst showed an even higher NH_3 yield at 3.665 mg/(mg_{Ru}h) at −0.21 V, with the Faradaic efficiency as high as 21%. In this study, ZrO_2 was used to suppress the competitive HER. DFT calculations showed that Ru SAs anchored to the oxygen vacancies in ZrO_2 or in a $Ru-C_2N$ structure embedded in carbon were favorable for NRR. However, the former has a higher Faradaic efficiency, whereas the latter has a higher NH_3 yield.

In comparison with those for HER, some fundamental insights can be obtained about these two competitive reactions catalyzed by Ru SACs. First, in N-doped carbon, thermodynamically the $Ru-C_xN_y$ structures may have activity toward both HER and NRR. In practice, however, the activity varies with the specific structure. For instance, 4-coordinate $Ru-C_2N_2$ and defected $Ru-C_x$ may be active toward HER, whereas others work for NRR or even for both (e.g., 3-coordinated $Ru-C_2N$). It is typically easier to achieve a high activity for HER than for NRR, and N-rich coordination can increase the NRR performance. For example, $Ru-N_4$ is known to be effective catalysts for NRR and not so much for HER, whereas Ru nanoparticles and (defected) $Ru-C_x$ in general show a high activity for HER but a low activity for NRR. Second, for NRR applications, Ru SAs needs a supporting scaffold to suppress the HER activity (e.g., ZrO_2). Since research has shown that Ru SAs are good HER catalysts when coordinated to N, O, and S, the success of finding an effective HER-suppressing agent represents a key direction for the development of Ru SACs for NRR.

2.2.4. Other Reactions. Ru SAs also show activity for other electrochemical reactions. Wang et al.[78] synthesized Ru SAs on a monolayer NiFe LDHs, with a Ru coordinated to four oxygen atoms and three of them linked to Ni or Fe atoms, at the Ru loading of ca. 7.0 wt %. The sample exhibited a low potential for hydrazine electrooxidation.

The report of Ru SACs toward ORR has been scarce. Zhang et al.[79] reported that $Ru-N_4$ moieties might be good for ORR in acid. The catalyst was prepared by annealing a Ru salt and graphene oxide under an NH_3 atmosphere, with the Ru SAs in the form of $Ru-N_4$. During ORR, the Ru SAs were converted to $Ru-N_4O$. The nanocomposites showed a high activity for ORR in acid, with an onset potential (E_{onset}) of +0.89 V, $E_{1/2}$ of +0.76 V, and a 4e$^-$ pathway.

https://dx.doi.org/10.1021/acscatal.0c01950
ACS Catal. 2020, 10, 7584−7618

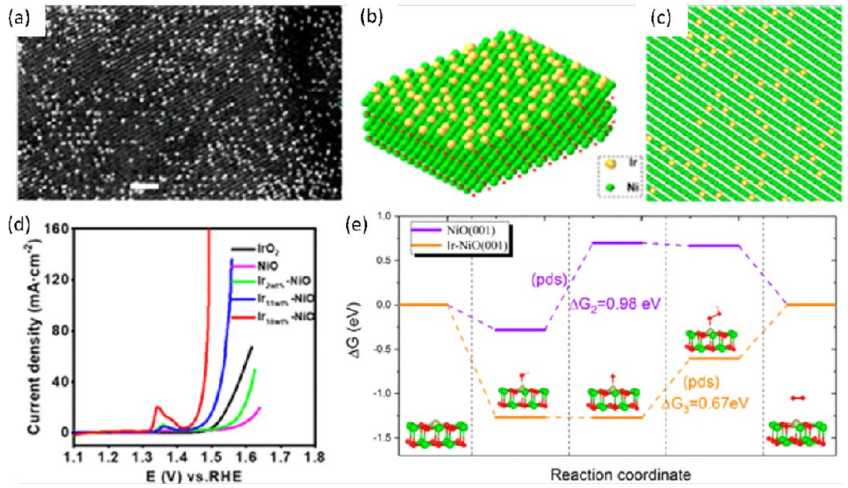

Figure 7. (a) HAADF-STEM image of the Ir-NiO catalyst, in which the bright spots are Ir single atoms. (b,c) Atomic models in different orientations. (d) Polarization curves for OER in 1 M KOH. (e) Free energy diagram of OER at +1.23 V for Ir SAs-doped NiO(001). Adopted with permission from ref 26. Copyright 2020 American Chemical Society.

In summary, one can see that the rich coordination chemistry of Ru endows Ru SAs with unique electrocatalytic activity toward a range of important reactions, which can be regulated by the nitrogen coordination linkages. Specifically, the nitrogen-rich Ru−N_4 moieties are good catalytic sites for NRR, ORR, and OER. At decreasing nitrogen loading, Ru−C_xN_y may be active toward HER (e.g., Ru−C_2N_2) and NRR (e.g., Ru−C_2N) with an appropriate HER-suppressing agent (e.g., ZrO_2). For Ru−N_2, Ru−N_4P, and Ru−N(O)S, in general only apparent HER, not NRR, activity is observed.

2.3. Ir SACs. Ir SACs are primarily used as high-efficiency OER catalysts, although studies have remained limited thus far. In one study, Zhang et al.[80] placed Ir SAs into defect-rich cobalt hydroxide nanosheets by a $NaBH_4$ reduction process and observed an apparent OER activity in neutral electrolyte, with $\eta_{10,OER}$ = +373 mV, significantly outperforming commercial IrO_2. This catalyst also showed a low $\eta_{10,OER}$ of +235 mV in 1 M KOH. EXAFS measurements suggested the formation of Co−Ir and Ir−O bonds, and the high OER activity was ascribed to the high-valence Ir species and CoOOH with unsaturated coordination. In a similar structure, Wang et al.[26] deposited Ir SAs onto NiO/carbon cloth by calcination in air (Figure 7). XANES measurements showed a +4 oxidation state of Ir in Ir−O−Ni bonding linkage in an octahedral Ir−O_6 structure. The oxygen atoms were connected to other Ni atoms in the NiO host. Such a structure exhibited a high OER activity in 1 M KOH, with $\eta_{10,OER}$ = +215 mV. In addition, DFT calculations showed that Ir atoms served as the active sites and concurrently activated the adjacent Ni atoms because of charge transfer from Ir to Ni.

Results from these studies highlight the promising outlook of Ir SACs supported on metal oxides (especially those with intrinsic OER activity) for efficient OER. In comparison to Ru SACs, it is believed that the A−O−M (A = Ru, Ir; M = Fe, Co, Ni) coordination plays a key role in determining the OER activity, where Ru/Ir serves as active sites as well as activators of the support materials.

Note that Ir SAs (e.g., in the configuration of Ir−N_4) can also be active toward ORR,[81] with a performance comparable to that of Pt/C. Further and more systematic studies are needed to advance our understanding of the mechanistic origin for further improvement of the electrocatalytic performance.

2.4. Au SACs. While rarely used directly as electrocatalysts, Au SAs have been shown to significantly influence the local electronic structure and enhance the catalytic activity of the support materials, in particular, toward OER. Similar to earlier studies with Ru SAs on LDHs, Zhang et al.[82] deposited Au SAs onto Ni−Fe LDHs forming Au−O−Ni(Fe) bonds and observed marked enhancement of the OER activity in alkaline electrolyte. The Au−O−Ni(Fe) coordination moiety was found to lead to charge redistribution, with 0.32 e transferred from Au to the nearby Fe, O, and Ni atoms, which served as the OER active sites. Au SAs supported on Co_3O_4,[83] Ni_2P,[84] or $CoSe_2$[85] have also shown obvious enhancement of the OER activity, as compared to the pristine substrate. Similar enhancement of the HER activity by Ru nanoparticles has also been observed with Au SAs because of charge transfer from Ru to Au.[86]

In addition to the assistive effect, Au SAs can serve as active sites for NRR. Wang et al.[87] prepared an NRR catalyst with Au−C_3N_4 moieties. The Au atoms were trapped in the g-C_3N_4 rings and coordinated with three nitrogen atoms. The resulting nanocomposites showed a high NH_4^+ yield rate of 1305 $\mu g/(mg_{Au}h)$, 22.5 times better than that with Au nanoparticles deposited on g-C_3N_4.

2.5. Pd SACs. Studies of Pd SACs are relatively scarce, although Pd SAs supported on a metal oxide forming Pd−O bonds have been known to exhibit electrocatalytic activity toward ORR and HER. Xiang et al.[88] prepared Pd SACs supported on MnO_2 nanowires (NWs)-carbon nanotubes (CNTs) networks by a one-pot hydrothermal method. XAS measurements showed that Pd SAs were positively charged with a valence state of +2 and coordinated with 4 oxygen atoms, involving two main structures, one with Pd−O_4 on carbon and the other with Pd−O_4 on the surface of the MnO_2 host. The resulting sample showed a high mass activity toward ORR (484 A/g_{pd}), 20 times better than that of commercial Pd/C in alkaline electrolyte, and a high n of 3.84. In another study, Li et al.[89] synthesized Pd SAs on MoO_3 nanoparticles and claimed that the atomically dispersed Pd atoms significantly increased the number of active sites and facilitated electron transfer in HER.

In another study, Kim et al.[90] prepared Pd SAs supported on N-doped carbon, where the Pd SAs were bonded to C or N

https://dx.doi.org/10.1021/acscatal.0c01950
ACS Catal. 2020, 10, 7584−7618

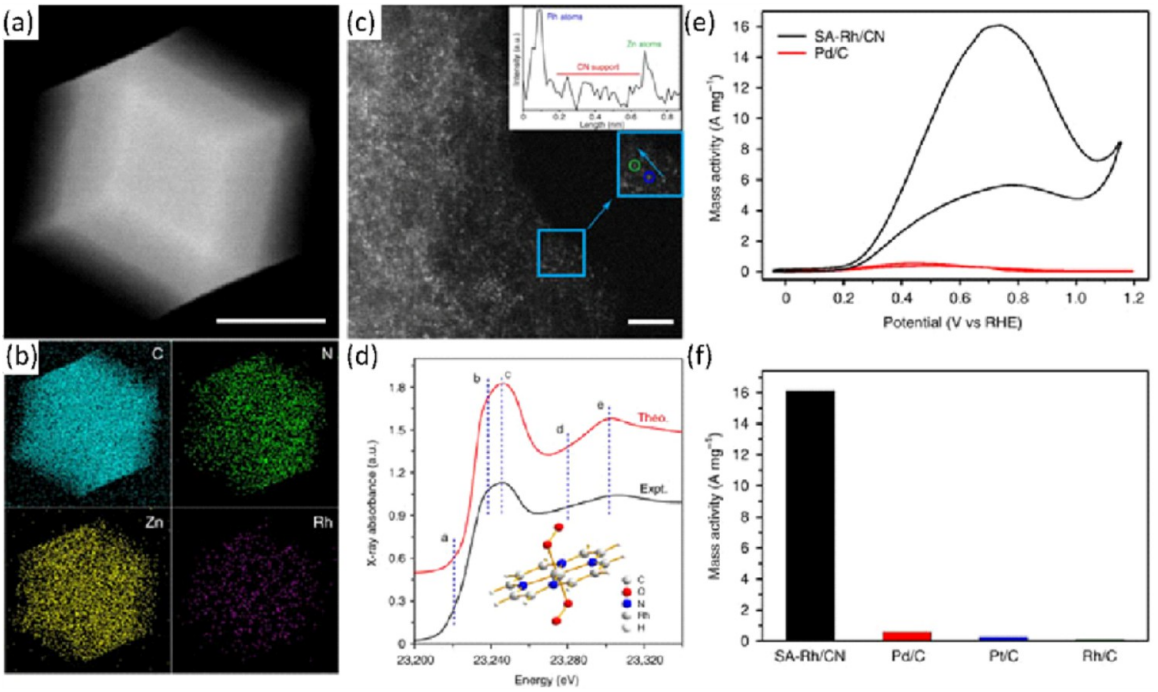

Figure 8. (a) HAADF-STEM image and (b) corresponding EDS maps of the SA-Rh/CN catalyst. (c) AC-HAADF-STEM image and corresponding Z-contrast analysis (inset). The Rh and Zn atoms are marked by blue and green circles, respectively. (d) Comparison between the experimental Rh K-edge XANES spectrum of SA-Rh/CN and the theoretical spectrum calculated for the depicted structure. (e) CV curves for SA-Rh/CN and commercial Pd/C in 0.5 M H_2SO_4 with 0.5 M HCOOH at the scan rate of 10 mV/s. (f) Comparison of the mass activity of various samples. Adopted with permission from ref 91. Copyright 2020 Springer Nature.

atoms, with a total coordination number around 4, as manifested in XAS studies. Interestingly, the resulting Pd SACs were active toward ORR, catalyzing the $2e^-$ reduction of O_2 to H_2O_2 in high yields, with E_{onset} = +0.67 V and $E_{1/2}$ = +0.50 V. Such a behavior is similar to that of Pt SACs (section 2.1). Notably, the activity toward other reactions (e.g., HER, HOR, FAOR, and MOR) was relatively poor, in contrast to Pt SACs. This was largely accounted for by the weak H adsorption, and lack of interaction with CO by Pd SACs (manifested in CO stripping) that rendered it difficult to generate the CO_{ads} intermediate, hence blocking the indirect pathways of MOR and FAOR.

2.6. Other Noble Metals. Reports of other noble metal SACs are very rare. In a recent study, Xiong et al.[91] prepared a Rh SAC by pyrolysis of ZIF-8 with $Rh(acac)_3$, where $Rh-N_4$ moieties were embedded in N-doped carbon, and the Rh SAs displayed a valence state of +3. The resulting sample showed an ultrahigh activity for FAOR, with a mass activity of 16100 A/g, 67 and 805 times higher than those of Pt/C and Rh/C, respectively (Figure 8). Moreover, the stability was outstanding, with only a 11% activity loss after 30 000 cycles. The $Rh-N_4$ active sites also showed unique CO resistance. CO stripping experiments and DFT calculations showed that the $Rh-N_4$ site facilitated the direct oxidation of HCOO* to CO_2. This reaction pathway is similar to that of Pt SAs in section 2.1.3.

3. NON-NOBLE METALS

Most conventional electrocatalysts are based on noble metals; yet their high costs and limited natural abundance have become a major bottleneck that impedes the widespread practical applications of the technologies. Therefore, extensive research has been devoted to the development of highly active and economical substitutes by non-noble metal elements. SACs based on such elements represent a unique family of effective electrocatalysts, owning to the dramatic change of the electronic states when the size of the metals is minimized to isolated atoms and coordination with nonmetal atoms (e.g., C, N, O, and S). This leads to an electrocatalytic performance that can even rival that of state-of-the-art noble metal catalysts.[22,23,92−97] Similar to the noble metal counterparts, the electrocatalytic activity can be readily manipulated by the specific coordination configurations of the SACs. This has been demonstrated in a number of studies involving various transition metals for different reactions, e.g., Fe (ORR, CO_2RR), Co (ORR, HER, OER, CO_2RR), Ni (HER, OER, CO_2RR), Cu (ORR), Zn and Cr (ORR), Mo (H_2O_2 production), Mn (ORR, OER, CO_2RR), and even main group metals like Al and Mg (ORR). Below we will summarize recent progress in these areas of research.

3.1. Fe SACs. *3.1.1. ORR.* Unlike noble metals (e.g., Pt and Pd), bulk Fe does not have an apparent catalytic activity toward ORR. Yet, its macrocycle complexes with $Fe-N_4$ coordination, such as iron(III) phthalocyanine (FePc) and iron(III) porphyrin, have been known to be efficient molecular ORR catalysts (via the $4e^-$ pathway) for decades.[98−101] However, such molecular catalysts are not sufficiently robust for practical applications.[101] Although efforts like thermal pyrolysis of these macrocycles have been carried out to enhance the structural integrity, the pristine $Fe-N_4$ structure typically becomes decomposed and aggregated, leading to a reduced ORR performance.[100,102−104] To mitigate this issue, other strategies have been explored. For instance, Lee et al.[105] utilized plasma-enhanced chemical vapor deposition (CVD) to grow CNTs modified with $Fe-N_x$ moieties, which displayed apparent ORR activity, as compared with pristine CNTs. Fe−

https://dx.doi.org/10.1021/acscatal.0c01950
ACS Catal. 2020, 10, 7584−7618

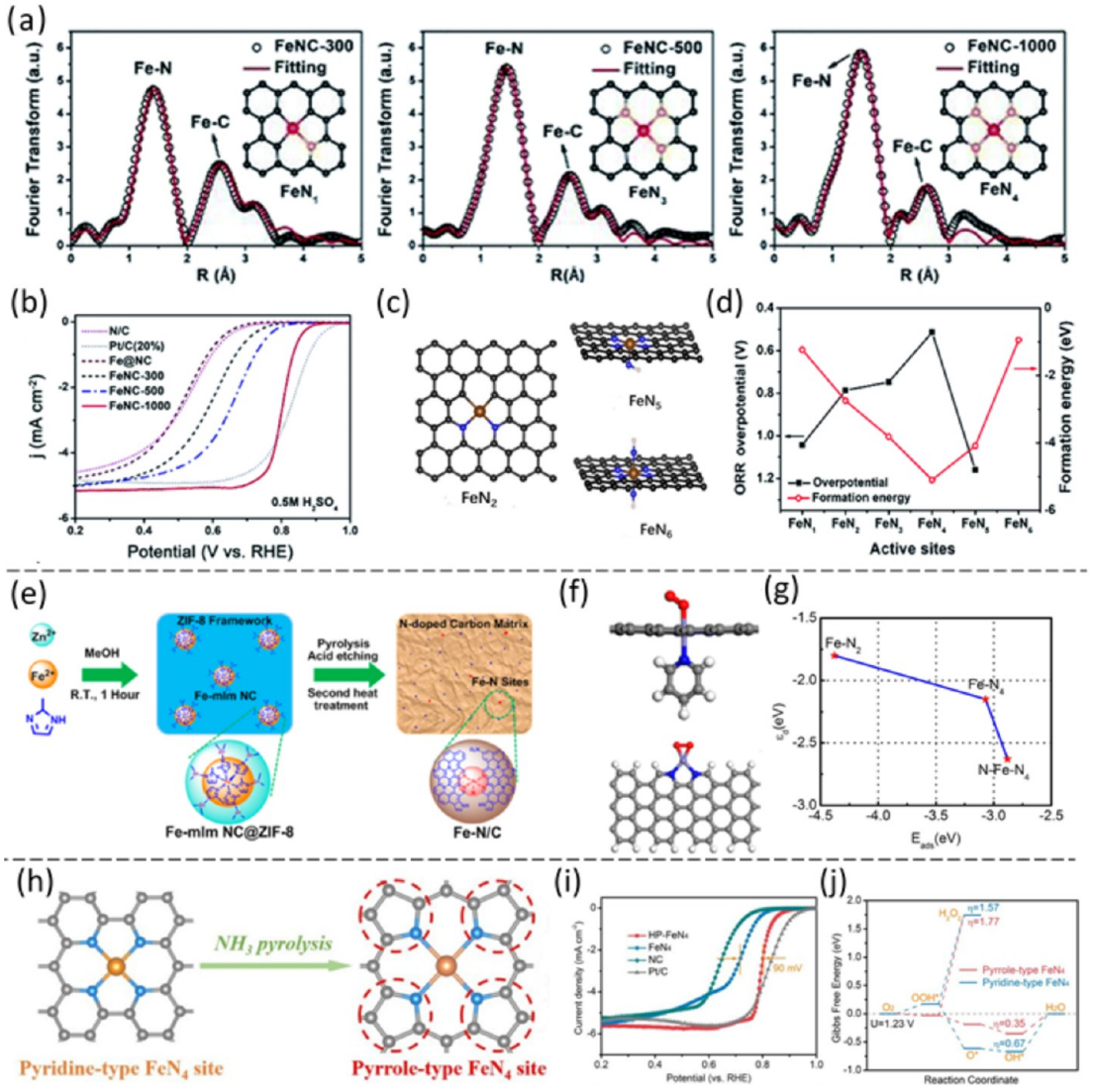

Figure 9. Representative examples of Fe−N_x−C catalysts with various coordination structures. (a) EXAFS data and active site models of FeNC-300/500/1000. (b) ORR polarization curves of FeNC-300/500/1000 catalysts and Pt/C in O_2-saturated 0.5 M H_2SO_4 at the rotating rate of 1600 rpm. (c) Theoretical models of Fe−$N_{2/5/6}$−C. (d) Formation energies and ORR overpotentials of Fe−N_x-C (x = 1−6) moieties determined by DFT calculations. Adopted with permission from ref 113. Copyright 2019 Royal Society of Chemistry. (e) Synthetic scheme of Fe−N−C catalyst with Fe−N_5 (Fe−$N_{4\text{-pyridine}}$−N_{pyridine}) moieties. (f) Models of Fe−N_5 and Fe−N_2 moieties. (g) Adsorption energy of OH intermediate on different Fe−N_x sites. Adopted with permission from ref 114, copyright 2017 American Chemical Society. (h) Preparation scheme of high-purity (HP) pyrrole-type FeN_4 structure. (i) ORR polarization curves of HP-FeN_4, FeN_4, and NC catalysts in O_2-saturated 0.5 M H_2SO_4 and 20% Pt/C in 0.1 M $HClO_4$ at the rotating rate of 1600 rpm. (j) Free energy diagram of ORR on pyrrole-type FeN_4 and pyridine-type FeN_4. Adopted with permission from ref 121. Copyright 2020 Royal Society of Chemistry.

N_4 was argued to be the main structural moiety on the basis of the atomic ratio of Fe to N from XPS measurements. DFT calculations of the band structure indicated that the Fe−N_4 moieties helped CNTs form a new state above the Fermi level (≈0.3 eV), which enhanced the electrical conductivity of CNTs and facilitated the adsorption of oxygen intermediates. However, XPS studies alone cannot determine that all Fe species were in the Fe−N_4 (pyridine-type) configuration, as other nitrogen vacancies like N_3 or N_2 can also serve as coordination sites to chelate Fe atoms during CVD, and other nitrogen dopants, like pyrrolic N, can also form Fe−N_4 and contribute to the ORR activity as well. In addition, unlike conventional metal macrocycle complexes, the Fe−N_x moieties may activate the surrounding C and N atoms as active sites.[22,106] These issues have been the foci of a range of recent studies.[23,107−111]

In an earlier study, Wang et al.[108] carried out poisoning experiments in acidic media with various ions and gas (e.g., Cl^-, F^-, SCN^-, and SO_2) and argued that the ORR active site of the Fe−N_x−C catalysts derived from poly *m*-phenylenediamine was most likely the Fe^{III} center of the Fe−N_x moiety. However, in some other studies in alkaline media, no significant variation of the activity is observed with the poisoning ions,[109,112] suggesting that the neighboring non-metal atoms (i.e., C and N atoms) might serve as the actual active sites in the Fe−N−C catalysts. This is also aided by results from DFT calculations. For example, in a combined experimental and theoretical study, Lu et al.[22] suggested that the Fe centers of both normal pyridine-type and Stone−Wales

https://dx.doi.org/10.1021/acscatal.0c01950
ACS Catal. 2020, 10, 7584−7618

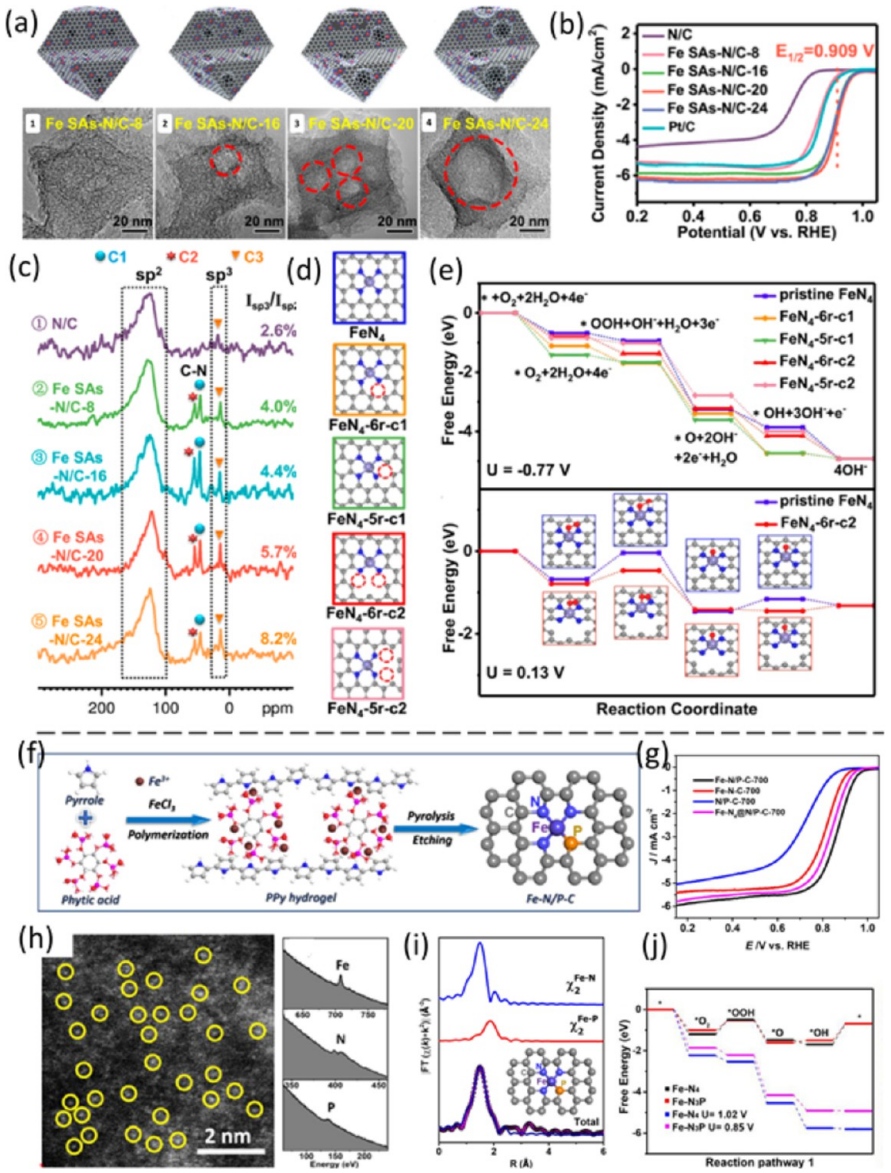

Figure 10. Representative examples of Fe−N_x−C catalysts with the Fe−N−C coordination moieties at the edge or with second dopants. (a) Schematic models and corresponding TEM images of Fe SAs-N/C-*x* catalysts. (b) ORR polarization curves of the Fe SAs-N/C-*x* catalysts in 0.1 M KOH, in comparison to the metal-free N/C and commercial Pt/C. (c) Solid-state ^{13}C NMR spectra of Fe SAs-N/C-*x* catalysts. C1 and C2 refer to two different types of *N*-alkyl carbons, and C3 to sp^3-hybridized carbons. (d) Five possible Fe−N_x atomic configurations with different cracking degrees. (e) Free energy diagrams at $U = -0.77$ V (upper) and 0.13 V (lower). Adopted with permission from ref 125. Copyright 2018 American Chemical Society. (f) Schematic of the synthesis process of the Fe−N/P−C catalyst. (g) ORR polarization curves of Fe−N/P−C-700, Fe−N−C-700, N/P−C-700, and Fe−N4@N/P−C-700 catalysts at the rotation speed of 1600 rpm in 0.1 M KOH solution. (h) HAADF-STEM image and the corresponding EELS atomic spectra of Fe, N, and P elements. (i) EXAFS data of Fe−N−P−C catalyst and the proposed model (inset). (j) Free energy diagram of ORR on Fe−N_3P moiety. Adopted with permission from ref 132. Copyright 2020 American Chemical Society.

pyrrole-type FeN_4 moieties were the predominant active sites of ORR, rather than the coordinated N atoms. Interestingly, in the Stone−Wales Fe−N_4, the neighboring C atoms of Fe−N_4 could also serve as ORR active sites, suggesting that Fe centers might activate the neighboring nonmetal atoms as well. Yang et al.[106] reached a similar conclusion. That is, regarding the active sites of the Fe−N−C catalysts, the Fe, C, and N atoms involved should all be taken into account.

One may note that Fe−N−C catalysts derived by pyrolysis of polymer or graphene precursors inevitably contain various Fe−C_xN_y configurations, which have different contributions to the ORR activity. For example, Li et al.[113] prepared a series of Fe−C_xN_{4-x} samples (x = 1, 3, 4, as evidenced in EXAFS measurements, Figure 9a) and observed that the ORR performance decreased in the order of Fe−N_4 > Fe−C_1N_3 > Fe−C_3N_1 both in acidic and alkaline media (Figure 9b). This was in line with results from DFT calculations, where the ORR activity diminished in the order of Fe−N_4 > Fe−C_1N_3 > Fe−C_2N_2 > Fe−C_3N_1 > Fe−N_5 (Figure 9a,c,d).

Although calculations suggested that Fe−N_5, with the Fe center coordinated to four coplanar pyridine-type N atoms and one vertical dangling N atom, was the least active moiety for ORR, some experimental results suggest that Fe−N_5 may actually exhibit good activity.[114−117] For example, Zheng et al.[117] showed that the Fe−N_5 (Fe−$N_{4\text{-pyridine}}$−N_{pyrrole}) type coordination was a promising ORR active site with a low

https://dx.doi.org/10.1021/acscatal.0c01950
ACS Catal. 2020, 10, 7584−7618

overpotential. Meanwhile, their calculations showed that planar Fe−N_4 tended to transform into more stable square-pyramid Fe−N_5. However, other square-pyramid centers with five coordinates, such as Fe−C_2N_3, Fe−C_3N_2, and Fe−CN_4, would all be favorable for H_2O_2 production instead. Experimentally, Huang et al.[116] embedded FePc onto 4-aminopyridine functionalized graphene oxide (GO) to form abundant Fe−N_5 (Fe−$N_{4\text{-pyrrole}}$−$N_{\text{pyriddine}}$) moieties and observed markedly enhanced ORR performance in alkaline media, as compared with that of Pt/C. They proposed that the axial pyridine N could stabilize the Fe center. Lai et al.[114] pyrolyzed and etched Fe^{2+}-impregnated ZIF-8 to yield Fe−N−C materials (Figure 9e), which contained abundant Fe−N_x moieties with x ranging from 2 to 6. To examine the contributions of these different coordination configurations, they theoretically compared the square-pyramid Fe−N_5 (Fe−$N_{4\text{-pyridine}}$−N_{pyridine}, Figure 9f), edged-site pyridine-type Fe−N_2 (Figure 9f) and conventional planar pyridine-type Fe−N_4. The results suggested that at 1.23 V, the Fe−N_5 coordination showed a lower energy barrier (0.67 eV) than Fe−N_4 (0.75 eV) or Fe−N_2 (1.99 eV), meaning that Fe−N_5 should have the best activity. In addition, as depicted in Figure 9g, they also compared the adsorption energy of OH (E_{OH}) of these three structures, which varied in the order of Fe−N_2 (4.38 eV) > Fe−N_4 (3.07 eV) > Fe−N_5 (2.88 eV), and argued that the low E_{OH} of Fe−N_5 could protect the active sites from deactivation and damaging radicals, in good correlation with the good stability observed experimentally in acidic electrolyte. A later study from Lin et al.[118] also supported the argument that the Fe−N_5 (Fe−$N_{4\text{-pyridine}}$−N_{pyridine}) coordination moiety was better than solvated Fe−N_4−OH and pristine Fe−N_4, with the most optimal calculated E_O and lowest energy barrier of the rate-determining step (RDS). Yet in some other studies, it has been argued that the Fe−N_2-type coordination performed better than Fe−N_4.[119,120] Taking the solvation effect into account, Shen et al.[119] reconfigured their DFT model of Fe−C_2N_2 with an additional dangling hydroxy ligand that was connected vertically to the Fe center and found that Fe−C_2N_2 was more beneficial for ORR in alkaline media than Fe−N_4 both theoretically and experimentally because of its reduced overpotential and enhanced electron transport. Zhu et al.[120] also observed a superior ORR activity of Fe−N_2-type catalysts with an $E_{1/2}$ of +0.927 V in alkaline media, and the catalysts even resisted the poisoning of SCN^- because of the high affinity to O_2, in contrast to leading results in the literature.

In the various Fe−N−C structures discussed above, it should be noted that pyridine-type Fe−N_4 coordination on graphene is the most prevalent model in theoretical calculations, while pyrrole-type Fe−N_4 may actually be more catalytically active. In a recent experimental study, Zhang et al.[121] compared the ORR activity of these two configurations. They used ammonia gas to convert the carbon materials embedded with pyridine-type Fe−N_4 moieties into the one with pyrrole-type Fe−N_4 moieties (Figure 9h), as evidenced by soft X-ray absorption spectroscopy measurement of the N 1s electrons. Further electrochemical measurements (Figure 9i) showed that the pyrrole-type Fe−N_4-C had a better performance with an $E_{1/2}$ of +0.8 V in acid than the pyridine-type one. This was consistent with results from theoretical study (Figure 9j), where the pyrrole-type Fe−N_4 had preferred oxygen adsorption with a lower overpotential from O_2 to OOH* than the pyridine-type. Consistent behaviors were observed by Peng et al.,[122,123] where covalent organic frameworks (COFs) embedded with uniform pyrrole-type Fe−N_4 exhibited an excellent ORR activity in alkaline media, with $E_{1/2}$ = +0.91 V. In a theoretical study, Liu et al.[124] investigated and compared three carbon structures for ORR electrocatalysis, Fe−N_4−C_{12} (pyrrolic), Fe−N_4−C_{10} (pyridinic), and Fe−N_4−C_8 (pyridinic Fe−N_{2+2}) and found that Fe−N_4−C_8 was the optimal site with the lowest activation energy for the breakage of the O−O bonds. Taken together, these results suggest that to unravel the mechanistic origin of ORR activity, the local carbon structures must also be taken into account, along with the Fe−N coordination configuration.

In most calculations, the structural model includes a N-doped graphene layer as a defect-free plane embedded with the Fe−N−C moiety. Yet, actual samples may contain substantial structural defects, such as edges, cavities, and carbon or nitrogen vacancies, which can significantly impact the ORR activity of the Fe−N−C moieties.[111,125,126] For instance, Jiang et al.[125] prepared porous Fe−N−C carbon by pyrolysis of ZIF-8/FePc (Figure 10a) and observed that the best sample reached an $E_{1/2}$ of +0.909 V (vs RHE) in alkaline media (Figure 10b). ^{13}C solid-state nuclear magnetic resonance (ssNMR, Figure 10c) measurements showed that the ratio of sp^3 to sp^2 carbon increased gradually with increasing pore size, suggesting enhanced cleavage of the C−N bonds. DFT calculations were then employed to compare several kinds of cleavages of the C−N bonds adjacent to the Fe−N_4 moiety, including the perfect Fe−N_4, Fe−N_4-6r-c1, Fe−N_4-5r-c1, Fe−N_4-6r-c2, and Fe−N_4-5r-c2 (5r or 6r denotes 5 or 6 members of the Fe−N-heterocyclic ring, and c1 or c2 refers to 1 or 2 cleavages in the models in Figure 10d). From the free energy diagrams in Figure 10e, one can see that defective Fe−N_4-6r-c2 was the best one with the lowest overall reaction free energy change (0.32 eV at U = 0.13 V), in comparison to 0.64 eV for the pristine Fe−N_4, suggesting that the pore defects indeed altered the electronic properties of the Fe−N_4 moiety and enhanced the ORR activity.

In addition to the pore effect, Fu et al.[111] also took the location of the Fe−N_4 moiety into consideration by making a comparison among four types of Fe−N_4 moieties (i.e., Fe−N_4 in bulk, Fe−N_4 in defective bulk, Fe−N_4 at the zigzag edge, and Fe−N_4 at the defective zigzag edge) using DFT calculations. The results showed that the thermodynamic limiting potential calculated at the Fe center of Fe−N_4 increased when the location changed from the bulk to the edge, and then increased further when a pore was introduced near the Fe−N_4 moiety, suggesting that high-porosity Fe−N−C was favorable for the ORR process. The theoretical argument was indeed supported by the experimental performance of porous Fe−N−C catalysts in 0.5 M H_2SO_4 with an $E_{1/2}$ of +0.8 V, which was better than that of the nonporous one (+0.78 V). A similar conclusion was reached by Wang et al.[126] that the edge sites might facilitate electron transfer in the catalytic reaction and lower the energy barrier. Indeed, experimental results showed that concentrated single Fe atoms performed comparably with commercial Pt/C in 0.1 M $HClO_4$. Therefore, one can see that neighboring defects can effectively alter and enhance the ORR activity of the Fe−N−C moieties.

The significance of Fe−N_4 catalysts toward ORR was also demonstrated in our recent studies with the coordination moieties supported on nanowrinkled carbon aerogels. The samples were prepared by controlled pyrolysis using a biomass hydrogel as the template and precursor.[23,127] The Fe−N_4 sites

https://dx.doi.org/10.1021/acscatal.0c01950
ACS Catal. 2020, 10, 7584−7618

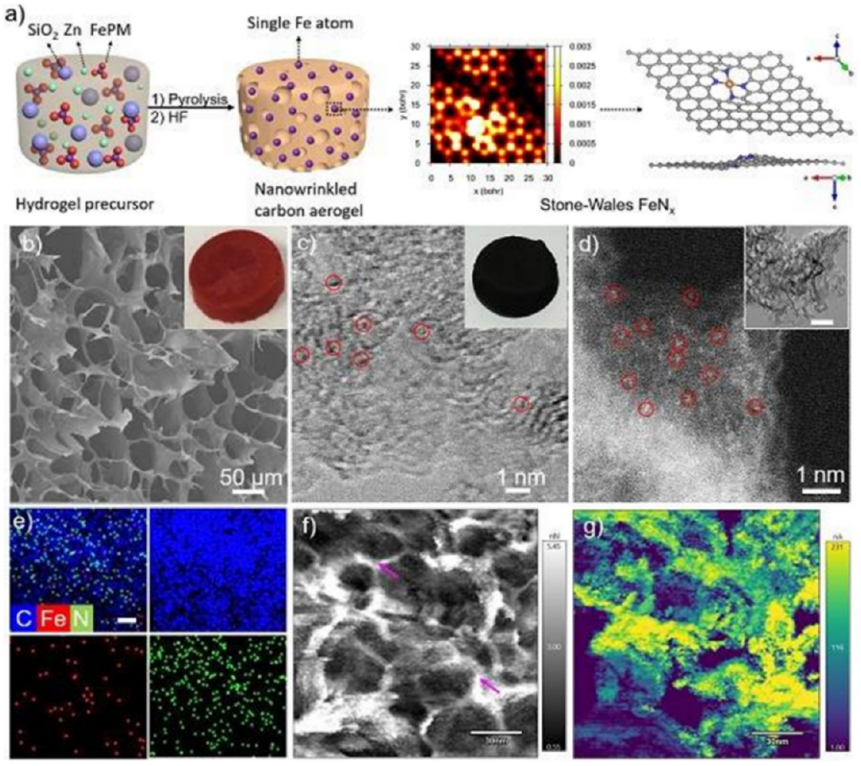

Figure 11. Synthesis and morphological characterization of Fe,N-codoped carbon aerogel. (a) Schematic of the synthesis of the NCA_{C-Zn}/Fe carbon aerogel. (b) SEM image of freeze-dried CS_{Si-Zn}/FePM hydrogel. (c) Bright-field STEM image of the NCA_{C-Zn}/Fe aerogel. Insets to panels b and c are the digital photographs of the corresponding samples. (d and inset) Dark-field STEM images, (e) elemental maps, (f) AFM topograph, and (g) adhesion force image of the NCA_{C-Zn}/Fe aerogel. Adopted with permission from ref 127. Copyright 2019 by the authors.

were mostly the Stone−Wales type out of the carbon plane, and more favorable for ORR than the normal FeN_4 sites (Figure 11). Electrochemically, the resulting composites exhibited a remarkable ORR activity in alkaline media that was comparable to that of commercial Pt/C, and could be used as the oxygen catalysts for metal-air batteries.

Other doping elements (e.g., S and P) have also been used to prepare carbon composites for ORR electrocatalysis.[94,128−131] For example, Yuan et al.[132] prepared Fe−N/P-C composites by pyrolysis of polypyrrole with $FeCl_3$ and phytic acid, which outperformed the P-free counterparts and commercial Pt/C toward ORR in 0.1 M KOH (Figure 10f,g). Results from TEM (with electron energy loss spectroscopy, EELS) (Figure 10h) and EXAFS measurements (Figure 10i) showed that Fe centers were coordinated to three pyridinic N atoms and one P atom of a six-membered ring, forming a $Fe−N_3P$ coordination moiety. DFT calculations showed that O_2 molecules could be easily absorbed and form a bond with the Fe center of the $Fe−N_3P$ moiety, in comparison to the P-free $Fe−N_4$. As for the RDS shown in Figure 10j, the detachment of OH* into OH^- was more endothermic on $Fe−N_4$ (1.02 eV) than on $Fe−N_3P$ (0.85 eV), indicating a better catalytic performance of the latter. In addition, even the uncoordinated P dopants could accelerate the kinetic process of O_2 adsorption onto the Fe center because of the optimized charge distribution.

Similar behaviors have also been observed with S-doped Fe−N−C. Mun et al.[94] varied the amount of S dopants in the Fe−N−C catalysts and found that too much S doping that formed a thiophene structure (C−S−C) near the $Fe−N_4$ moieties (Fe−N−C−S-C) would decrease the ORR activity, while an optimal amount of S dopants formed oxidized S ($−SO_2$) moieties as a member of the Fe−N-heterocyclic ring (Fe−N−C-SO_2−C) could boost the activity in 0.1 M $HClO_4$. DFT calculations indeed showed opposite electronic effects by $−SO_2$ (withdrawing e^-) and C−S−C (donating e^-) on the charge distribution of the $Fe−N_4$ moiety, and hence the adsorption of oxygen species on the Fe centers.

However, if the location of S relative to $Fe−N_4$ changes, the catalytic activity may vary accordingly. Li et al.[129] prepared a S-doped Fe−N−C catalyst, which featured a coordination structure of $Fe−N_4S_2$ with two S atoms directly coordinated with two diagonal N atoms of $Fe−N_4$. The resulting sample exhibited a high ORR activity with an $E_{1/2}$ of +0.896 V in alkaline media. DFT calculations showed that the S dopants induced a negative charge on N which repelled the adsorption of OH* and eased the reductive release of OH^-. Shen et al.[128] found that the thiophene structure could lower the ORR overpotential of the zigzag edge-site $Fe−N_2$ moiety by 40% when the two structures were separated by a distance of 7.3 Å, because sulfur could reduce the electron localization around the Fe center and enlarge the availability of electronic states around its Fermi level, leading to enhanced interaction between the Fe center and oxygen species. However, if the moiety was too close to the thiophene structure (e.g., 2.4 or 4.9 Å), no improvement of the catalytic activity was anticipated. Thus, in comparison with the work by Mun et al.,[94] one can see that the distance of the dopants and structure of the functional moiety both play a critical role in determining whether the dopants are beneficial to the ORR activity or not.

In summary, a range of structural parameters have been identified that can impact the ORR activity of $Fe−C_xN_y$

https://dx.doi.org/10.1021/acscatal.0c01950
ACS Catal. 2020, 10, 7584−7618

nanocomposites, such as the number of coordination, the coordination bonds, the geometric shape of the moiety, the defects adjacent to the moiety (porosity), as well as doping by second nonmetals. Results from leading Fe SACs for ORR are summarized in Table S4.

3.1.2. CO_2RR. Fe−N−C nanocomposites also exhibit apparent electrocatalytic activity toward CO_2 reduction to CO, with the activity varying with the coordination configuration of the Fe single atoms. Earlier studies have been mostly focused on FePc or Fe−N_4 on N-doped carbon.[7,133−140] Despite their appealing activities, one drawback of the Fe−N_4 moieties is that CO can strongly bind to the Fe center of Fe−N_4, leading to a sluggish last step of CO* desorption. In one study, Zhang et al.[133] observed that the additional graphitic N atoms around the Fe−N_4 moieties could facilitate COOH* adsorption and CO* desorption, as compared with naked Fe−N_4, because of the raised Fermi level and d-band center induced by the graphitic N atoms. Qin et al.[140] showed that the Fe−N_4 moiety near a pore defect (Fe−N_{2+2}) was much better than that in the bulk or at the edge, displaying higher tolerance to CO poisoning, as the pore defect induced a negative shift of the d-band center of Fe relative to the Fermi level, which further weakened the Fe−CO bond. In a recent study, Zhang et al.[141] showed that Fe−N_5 (pyridine-type Fe−N_4 with an axially connected pyrrolic N) was better than Fe−N_4 toward CO_2RR. Experimentally, Fe−N_5 moieties were embedded into graphene by pyrolysis of hemin-linked melamine complex with graphene, which manifested a high Faradaic efficiency for CO production (FE_{CO}) of 97% at a low onset potential of +0.35 V. DFT studies showed that the extra axial pyrrolic N ligand delocalized the electron density of the Fe center and hence reduced the Fe-CO π back-donation, prompting the desorption of CO. This suggests that the design of Fe−N−C catalysts for CO_2 reduction to CO should focus on a coordination that is beneficial for weak Fe-CO binding and hence CO* desorption.

3.2. Co SACs. *3.2.1. ORR.* Similar to FePc, cobalt phthalocyanine (CoPc) also exhibits good ORR activity.[98] In an earlier study, Yuasa et al.[142] directly impregnated cobalt ions into polypyrrole in methanol at a mild temperature of 60 °C to yield Co−N−C catalysts, which showed a clear pyrrole-type Co−N_4 coordination, as evidenced in EXAFS measurements. The catalyst showed an apparent ORR activity in alkaline media, and the activity was further improved after pyrolysis treatment at 700 °C, which was ascribed to the preservation of closely packed Co−N_4 moieties, rather than the partial formation of metallic Co in the samples. At the higher temperature of 1000 °C, the severe loss of Co−N moieties led to aggregation of metallic Co and substantially diminished the activity, suggesting that Co−N_4 moieties indeed dominated the activity. Nevertheless, as EXAFS measurements only provided averaged structural information, it was unclear if all Co−N_4 coordination moieties remained the same under pyrolysis at elevated temperatures.

Thus, extensive studies have been carried out to unravel the Co−N_x coordination configurations from both experimental and theoretical perspectives.[100] For instance, Ziegelbauer et al.[143] pyrolyzed Co porphyrins at different temperatures, which, based on XANES measurements, entailed an axial O adsorbed on Co−N_4, axial or planar O on Co−N_3, and planar O on Co−N_2(without Co−C bonds). Electrochemical measurements showed that higher pyrolysis temperatures resulted in the loss of N atoms and the formation of Co−$N_{2/3}$ moieties, whose planar adsorption of O atom would skew the ORR from the $4e^-$ process to the $2e^-$ one of H_2O_2 production. More recently, Zitolo et al.[144] prepared several types of defective Co−N_x moieties, and operando XAS analysis showed that the structure of the Co−N−C moieties remained unchanged at the applied electrochemical potentials, suggesting high structural robustness of the Co−N−C coordination during catalysis. In a theoretical study conducted by Kattel et al.,[145] the bonding interaction between Co and C was also taken into account in the coordination, and it was reported that formation of Co−N_4 was energetically more favorable than Co−N_2, suggesting that Co−N_4 was the dominant active site of ORR. Note that Co−N_4 and Co−N_2C_2 would have different binding geometries of O_2, where O_2 tends to bind in an end-on configuration to the Co center of Co−N_4 (O−O−Co) but prefers a side-on adsorption on Co−N_2C_2 (Co = O_2, with O_2 parallel to the graphene plane). Hence a different reduction pathway would follow on these two coordination types. However, further calculations show that peroxide intermediate (OOH*) can efficiently adsorb onto Co−N_2 but not on Co−N_4, implying that a second site was needed for the main active sites (Co−N_4 moieties) to reduce H_2O_2 into H_2O. This was consistent with results from another study by Sun et al.[146] All these calculations lead to a similar conclusion that Co−C_2N_2 moieties would serve as the second active sites to reduce H_2O_2 previously formed on Co−N_4. Meanwhile, while not very stable, the Co−C_2N_2 moiety itself could directly reduce O_2 into H_2O, suggesting that the formation of Co−N_2 moieties inside Co−N−C should enhance the ORR activity.

Experimental studies by Yin et al.[147] seemed to corroborate the above calculations. They prepared Co−N−C by pyrolysis of Co-containing ZIF at elevated temperatures and found that the Co SACs prepared at 900 °C featured a structure of Co−C_2N_2, which exhibited a remarkable ORR activity ($E_{1/2}$ = +0.881 V in 0.1 M KOH), outperforming the Co−N_4 counterpart ($E_{1/2}$ = +0.863 V). Zhu et al.[120] also observed a high $E_{1/2}$ of +0.878 V with Co−N_2-type SACs in alkaline media, which even resisted SCN^- poisoning without any decay of the activity. This was rarely reported with Co−N_4 SACs in the literature,[148,149] suggesting that O_2 adsorption to Co−N_x might change with the coordination configuration. From a theoretical perspective, Sun et al.[150] embedded Co-CN_3 moieties into graphene as a promising ORR catalyst to replace Pt, where the energy barrier of RDS was much lower on Co-CN_3 (0.38 eV) than that on a Pt (111) slab (0.80 eV) or Co−C_2N_2 (0.58 eV). Although Co−N_4 has been argued to be unfavorable for OOH* adsorption based on theoretical calculations,[145,146] Sun et al.[151] prepared a series of Co SACs, examined the overall ORR pathway of the Co−$C_{4-x}N_x$ (x = 1−4) moieties in alkaline media and observed that the overpotential increased in the order of Co−N_4 < Co−C_1N_3 < Co−C_2N_2 < Co−C_3N_1. This indicates that Co−N_4 coordination was likely the dominant active sites.

Although it remains debatable which Co−C_xN_y coordination is the best for ORR catalysis, Co−N_4 coordination has been the most frequently used model in the literature, similar to Fe−N_4.[149,152−154] Overall, Co−N_4 coordination is energetically more favorable and stable than Fe−N_4 under various potentials, as evidenced by operando XAS study.[144] Electrochemical measurements also showed better structural stability of Co−N_4 than that of Fe−N_4,[149] and the former exhibited

https://dx.doi.org/10.1021/acscatal.0c01950
ACS Catal. 2020, 10, 7584−7618

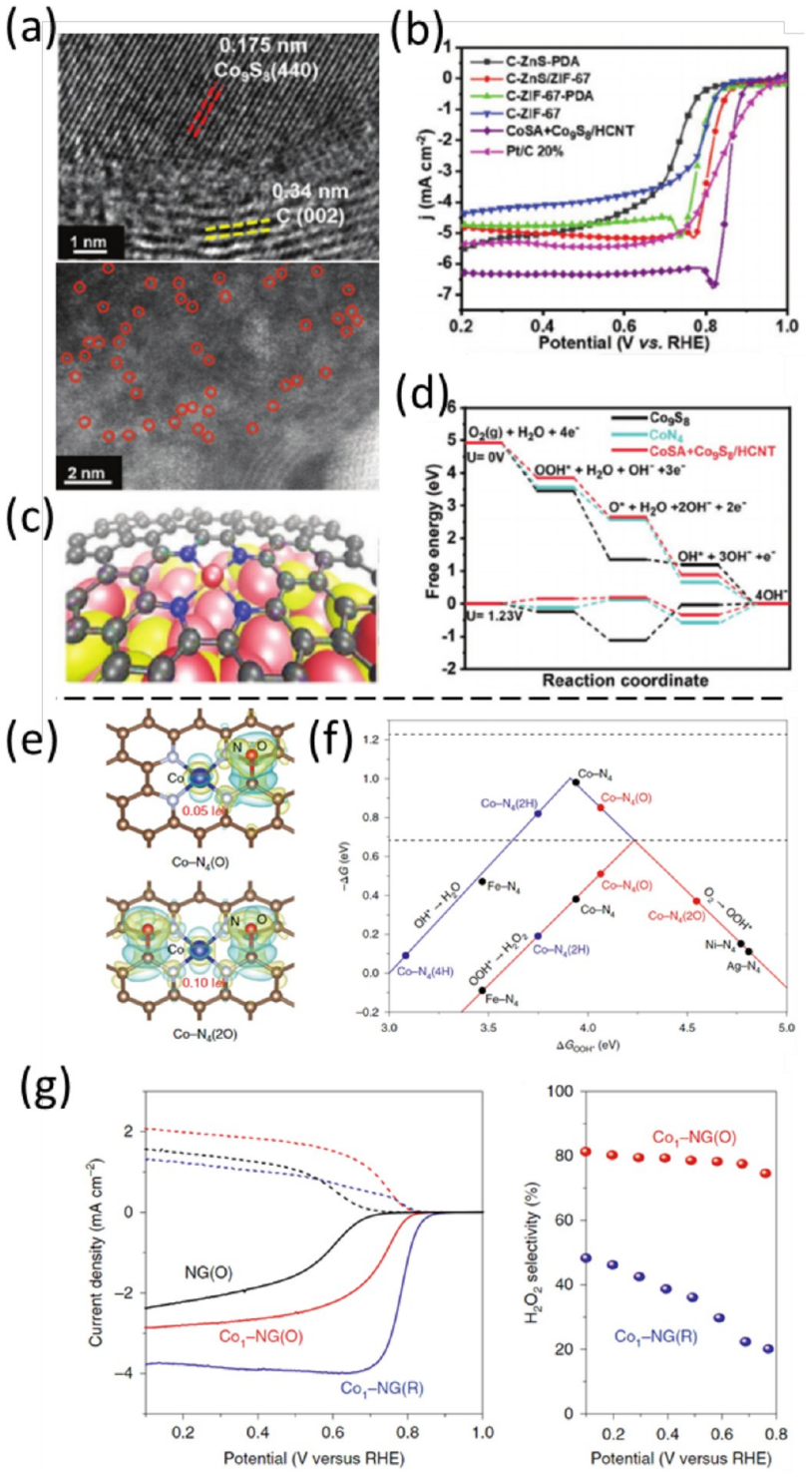

Figure 12. (a) (top) HRTEM image and (bottom) HADDF-STEM image of Co_9S_8 particles and Co single atoms. (b) ORR polarization curves of CoSA+Co_9S_8 catalyst and comparative samples in 0.1 M KOH at 1600 rpm. (c) Theoretical model of Co−N_4 on Co_9S_8. (d) Free energy diagram for the thermodynamic limiting potentials of the ORR steps. Adopted with permission from ref 158. Copyright 2020 Wiley-VCH. (e) Models of Co−N_4(O) and Co−N_4(2O) moieties and their respective charge densities. (f) Volcano plots of calculated ORR catalytic activity to produce H_2O (blue) and H_2O_2 (red). (g) (left) Comparison of ORR performance at 1600 rpm (solid lines) and the simultaneous H_2O_2 detection current densities at the ring electrode (dashed lines) for NG(O), Co$_1$−NG(O), and Co$_1$−NG(R) catalysts in 0.1 M KOH and (right) calculated H_2O_2 yield (%). Adopted with permission from ref 159. Copyright 2020 Springer Nature.

better resistance against SCN^- poisoning than the latter, consistent with the results from DFT calculations that O_2 increased the stability of Co−N_4 but not for Fe−N_4. Wan et al.[155] prepared a Co−N−C catalyst by pyrolysis of Co-histidine complex and attributed the high ORR activity ($E_{1/2}$ = +0.85 V) and antipoisoning ability in alkaline media, but not acidic, to the formation of Co−N_4 moieties. They further argued that the N sites coordinated to the Co center served as

https://dx.doi.org/10.1021/acscatal.0c01950
ACS Catal. 2020, 10, 7584−7618

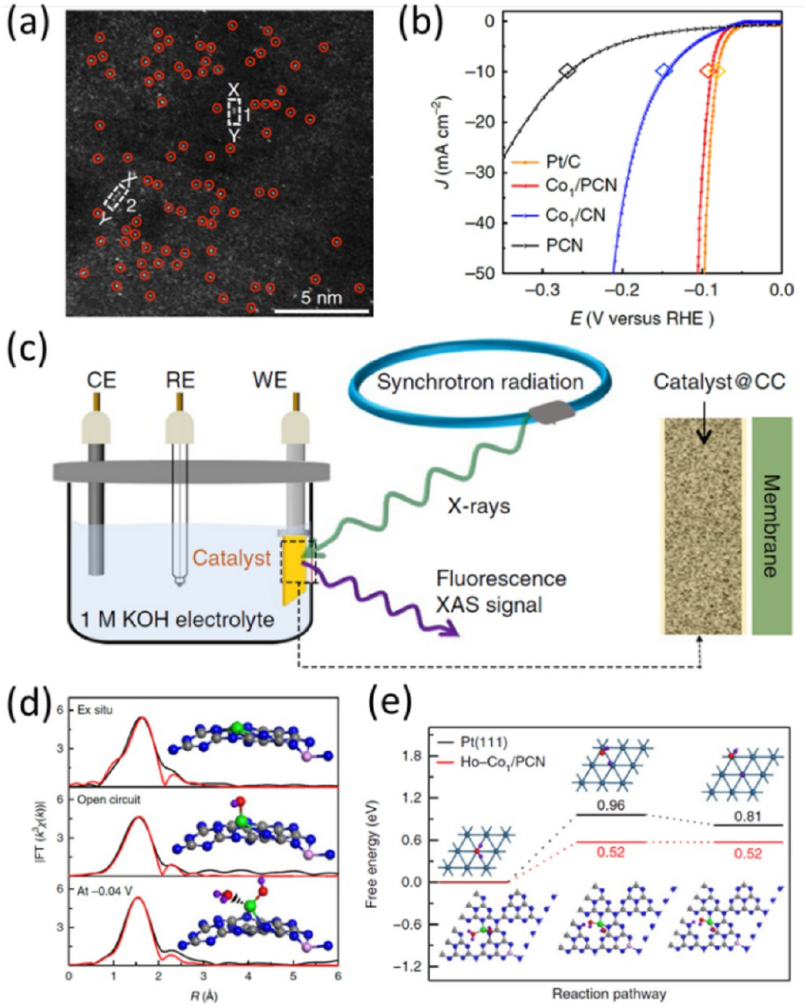

Figure 13. Operando XAS study of the coordination structure of Co−N−C HER catalyst. (a) HAADF−STEM image of Co_1/PCN with Co single atoms in red circles. (b) HER polarization curves of Co_1/PCN and compared samples in 1.0 M KOH. (c) Schematic of the operando electrochemical cell setup for the identification of the active site of Co_1/PCN. (d) EXAFS spectra of different fitting paths for the sample under ex situ and open-circuit conditions and at −0.04 V. The corresponding geometric configurations are shown in the panels: H, purple; C, gray; N, blue; O, green; P, pink; Co, red. (e) Calculated energy diagrams for H_2O dissociation for the Volmer step. Adopted with permission from ref 164. Copyright 2018 Springer Nature.

the main active sites when SCN^- ions blocked the Co centers, while Co SAs played a more critical role in acidic media, owning to the discrepancy of reaction pathways and intermediates between the reactions in alkaline and acidic media. Amiinu et al.[148] prepared Co−N−C nanorod arrays based on ZIF-67 and found that SCN^- could block the Co−N_4 centers and markedly decrease the ORR activity. Acid leaching was then carried out to remove Co species on nanorod arrays, which caused a negative shift of the $E_{1/2}$ by almost 50 mV, as compared with the as-prepared ones. Meanwhile, the resistivity against SCN^- ions was improved markedly with only a trivial loss of activity in alkaline media, suggesting that after acid leaching, the limited number of Co coordination moieties remained catalytically active and accessible for SCN^- poisoning. Their poisoning tests and acid treatment together validated that Co centers were crucial for the ORR activity. Notably, they then carried out theoretical studies to compare the pyrrole-type and pyridine-type Co−N_4 and found that Co−$N_{pyridine}$ produced a higher HOMO energy (−4.647 eV) than Co−$N_{pyrrole}$ (−4.765 eV), suggesting that the former could easily donate electrons and thus be more favorable toward ORR. Moreover, Co−$N_{pyridine}$ led to a higher DOS neighboring the Fermi level than Co−$N_{pyrrole}$, leading to a higher reactivity and electron mobility. This confirmed that the pyridine-type Co−N_4 coordination was more likely the active site. Taken together, these results suggest that the primary active site in alkaline media is the Co center in Co−N_4, with the coordinated N atoms being the coactive sites. Note that in Fe−N−C, the coordinated C sites may be coactive sites as well.

In another study, He et al.[156] fabricated microporous Co−N−C with abundant Co−N_{2+2} sites. The catalyst exhibited an $E_{1/2}$ of +0.84 V and excellent stability in corrosive acidic electrolyte. Further DFT study revealed that $4e^-$ ORR was thermodynamically more favorable on Co−N_{2+2} than on Co−N_4, as the RDS of OOH* dissociation entailed a much lower activation energy on the Co−N_{2+2} site (0.69 eV) than on Co−N_4 (1.11 eV).

The ORR activity of the Co−N−C ternary system can be further improved by doping with secondary nonmetal atoms due to a change of the coordination configuration.[157,158] For instance, Zhang et al.[157] pyrolyzed Co-thiourea complex and

https://dx.doi.org/10.1021/acscatal.0c01950
ACS Catal. 2020, 10, 7584−7618

produced a Co−N−C-S catalyst, which showed a high $E_{1/2}$ of +0.86 V in 0.1 M KOH. Unlike the coordination structure of Fe−N_4S_2,[129] Co atoms were argued to bond with S atom forming Co−N_3S_1 moieties as the active sites. This was thermodynamically more favorable than Co−N_4S_2, based on DFT calculations. Furthermore, Co−N_4 can be affected by the surrounding substrates like cobalt sulfide. Li et al.[158] constructed a hollow carbon nanotubes (HCNT) composite with Co_9S_8 nanoparticles encapsulated within the Co−N−C layers (CoSA+Co_9S_8/HCNT) (Figure 12a) that showed an ORR activity ($E_{1/2}$ = +0.855 V in 0.1 M KOH, Figure 12b) higher than that without S dopants and commercial Pt/C. In DFT calculations (Figure 12c,d), Co_9S_8 was found to reduce the adsorption free energy of oxygen intermediates on the Co center of Co−N_4 (0.35 eV), as compared to the pristine Co−N_4 (0.57 eV) at U = 1.23 V. This facilitated the desorption of OH*, the RDS of the overall ORR pathway.

In addition to the Co−N−C catalysts that favor the 4e$^-$ ORR discussed above, cobalt SACs have also been found to exhibit selectivity toward the 2e$^-$ ORR of H_2O_2 production, when oxygen functional moieties are around the Co SAs.[92,159,160] Jung et al.[159] employed DFT calculations to screen the reaction energetics of H_2O_2 production on a variety of metal−N_4C coordination structures. None of them was near the peak of the volcano plot of H_2O_2 production (Figure 12e,f), based on the adsorption energy (ΔG_{*OOH}) of *OOH (the most important intermediate of 2e$^-$ ORR). However, if functional groups like O* (electron-rich species) were added adjacent to the Co−N_4 moiety (Co_1−NG(O), Figure 12e), ΔG_{*OOH} could be increased from 3.9 to 4.1 eV and become closer to the optimal value for H_2O_2 production (Figure 12f). Addition of other electron-rich species like OH* leads to a similar result. Within this theoretical context, they treated Co-containing graphene oxide (GO) under mild reduction (NH_3 gas at 500 °C) to prepare Co−N_4(O) catalysts, which exhibited high H_2O_2 selectivity (∼80%) and mass activity (155 A/g at +0.65 V), as shown in Figure 12g. By contrast, Co−N_4 on GO formed at 900 °C with fewer O species (Co_1−NG(R)) had a strong tendency to react with O_2 via the 4e$^-$ pathway to produce H_2O. Li et al.[160] also found that when the Co−N_x moieties were modified with O functional groups, the selectivity of ORR could be varied from the 4e$^-$ to 2e$^-$ pathway.

In general, the engineering methods of the Co−N−C catalysts are similar to those for Fe−N−C, where coordination structures of the Co−N−C moieties can be modified and controlled, so as to improve the activity and control the selectivity of ORR. Table S5 summarizes the ORR performances of select Co SACs.

3.2.2. Water Splitting. Co SAs embedded in g-C_3N_4 or N-doped carbon have been reported as good HER catalysts for electrochemical water splitting.[96,144,152,161−163] For example, Fei et al.[162] pyrolyzed GO with Co salts at a high weight ratio of 125:1 under NH_3 gas to form Co−N−C catalysts, which exhibited an $\eta_{10,HER}$ of −147 mV in acid, much better than that without N dopants. This suggested the critical role of Co−N linkage in HER. In a later study, Cao et al.[164] embedded Co SAs in P-doped g-C_3N_4 (Co_1PCN), as evidenced by HAADF-STEM studies (Figure 13a), which displayed an $\eta_{10,HER}$ of −89 mV in 1 M KOH (Figure 13b). Operando XAS studies (Figure 13c) showed that the as-produced sample contained Co−N_4 as the initial coordination; yet when an electrochemical potential was applied for HER, Co−N_4 would spontaneously bind to OH$^-$ from the electrolyte forming a high-valence HO−Co−N_2 moiety. This suggested that the HO−Co−N_2 moiety was the actual active coordination (Figure 13d). In DFT calculations (Figure 13e), HO−Co−N_2 indeed was favorable for the dissociation of water molecules because of charge transfer from Co to the coordinated N and OH$^-$ groups, leading to a higher oxidation state of the Co center and a lower energy barrier (0.52 eV) for the Volmer step than that on Pt(111) (0.96 eV). In another study, Sa et al.[96] prepared Co−N−C with Co−N_x moieties embedded in CNT for HER and calculated several plausible Co−N_4 structures (i.e., CoPc, pyridine-type and pyrrole-type Co−N_4, Co−N_{2+2}, and various Co−N_5 configurations). Compared with Co nanoparticles encapsulated in graphene, all atomic Co moieties showed a lower $|\Delta G_H|$, with pyridine-type Co−N_4 being the optimal structure.

Recent studies of Co SAs on MoS_2 or MXene have also demonstrated striking HER performance.[95,165] For instance, Qi et al.[95] used a simple sonication and leaching method to prepare Co SAs on distorted 1T MoS_2 and observed a Pt-like HER activity with a low $\eta_{10,HER}$ of −42 mV in acid. In DFT calculations, Co SA was built into MoS_2 with a Co−S_3 coordination in a tetrahedral configuration. The results showed that the d-peak level at the Fermi level was stronger when the surface coverage of Co SAs on MoS_2 increased by varying the supercell from 4 × 4 to 3 × 3. Meanwhile, H* adsorption on the tilted top site of Co toward the adjacent S atom on the surface was better than that at the upright position of Co, suggesting that neighboring S could facilitate the adsorption of H* leading to enhanced HER activity.

Co SAs supported on carbon are also active toward OER.[166−168] Zhang et al.[166] prepared a Co−N−C catalyst with a good OER performance in alkaline media (onset overpotential ≈ + 210 mV) and theoretically analyzed the OER free energy diagrams for the Co−C_2N_2, Co−N_4, and Co−N_3 coordination moieties. It was found that both Co−C_2N_2 and Co−N_4 had a lower theoretical overpotential of +0.53 and +0.41 V, respectively, than Co−N_3 (0.90 V). In another study, Dou et al.[168] prepared porous carbon embedded with atomic Co−O_x species by O_2 plasma of ZIF-67, where the formation of the Co−O bonds was confirmed by EXAFS measurements. The formation of Co−O_x species led to a remarkable OER activity, with a potential ($E_{10,OER}$) of +1.548 V needed to deliver 10 mA cm^{-2} in alkaline media. This performance was comparable to that of commercial RuO_2 but markedly better than that of ZIF-67 ($E_{10,OER}$ = +1.63 V).

3.2.3. CO_2RR. As a versatile catalyst, Co SACs will not be absent from the catalysis of CO_2RR, where the electrocatalytic activity also varies with the exact coordination structure of the Co−N−C moiety.[169−172] Wang et al.[169] showed that at high temperatures, the Co−N_4 coordination in N-doped carbon might be gradually transformed into Co-CN_3 and then Co−C_2N_2, as observed previously for ORR.[147] The CO_2RR activity and CO selectivity decreased in the order of Co−C_2N_2 > Co−CN_3 > Co−N_4, indicating that Co−C_2N_2 was the optimal structure for CO_2RR. DFT calculations further revealed that adsorption of COO* onto Co−C_2N_2 was easier than onto Co−N_4, and the release of CO* was prompted on Co−C_2N_2 bound with two CO molecules because of a decrease of the desorption energy. In another study, Pan et al.[172] demonstrated that Co−N_5 coordination (CoPc with a pyrrolic N connected to the Co center) to be the best catalyst among CoPc, Co−N_4, and Co−N_3 with a FE_{CO} exceeding 90% in a wide potential range from −0.57 to −0.88 V, suggesting

https://dx.doi.org/10.1021/acscatal.0c01950
ACS Catal. 2020, 10, 7584−7618

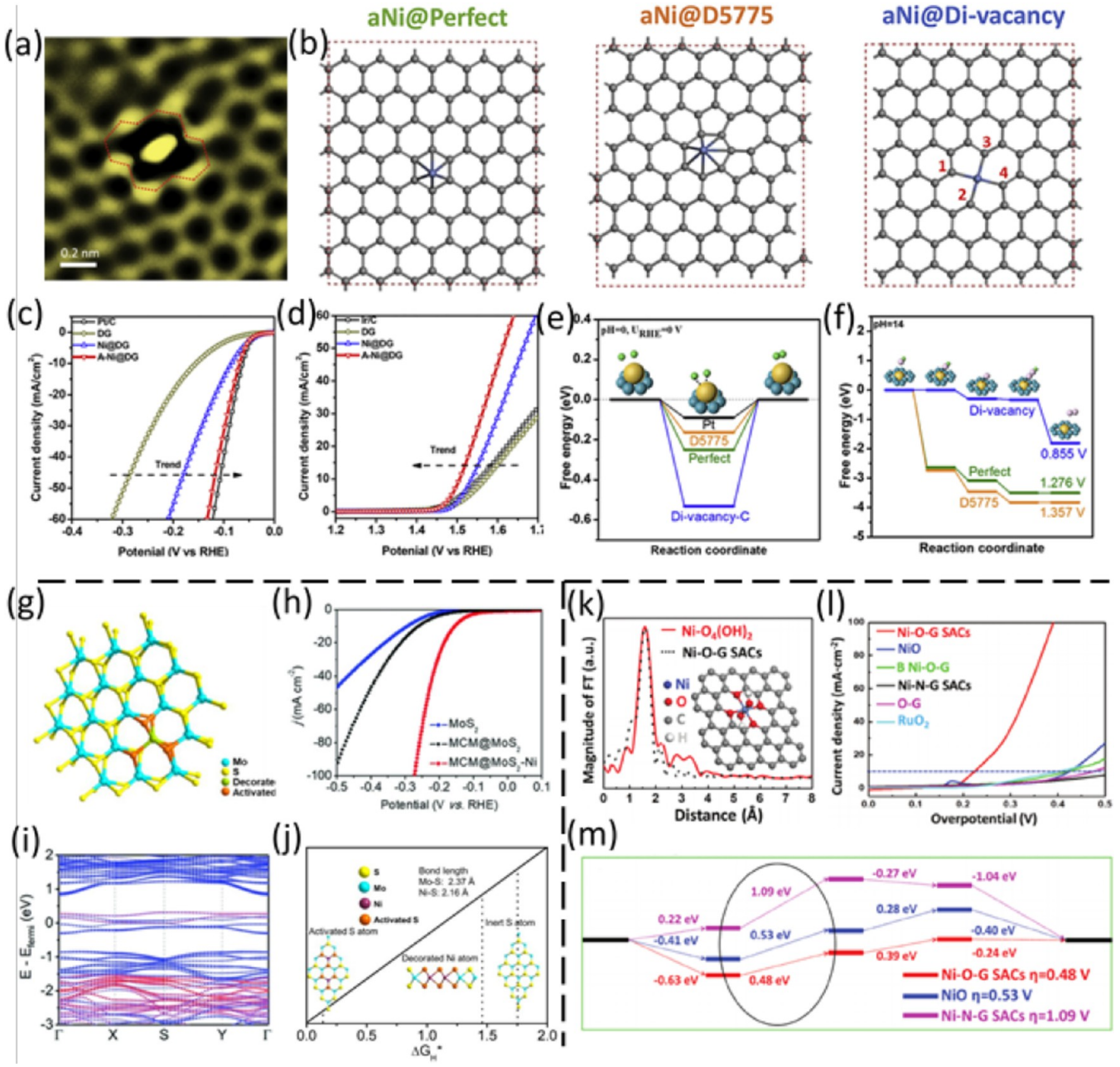

Figure 14. (a) HADDF-STEM image of A-Ni@DG. (b) Three possible models of Ni SAs of A-Ni@DG. (c) HER polarization curves of A-Ni@DG and compared samples in 0.5 M H_2SO_4. (d) OER polarization curves of A-Ni@DG and compared samples in 1 M KOH. Energy profiles of the three configurations for (e) HER and (f) OER. Adopted with permission from ref 173. Copyright 2018 Elsevier Ltd. (g) Model of a Ni SA on MoS_2. (h) HER polarization curves for different catalysts in 0.5 M H_2SO_4. (i) Band structure of Ni SA decorated MoS_2. (j) Theoretical calculations for the effects of Ni decoration on the HER activity of MoS_2. Adopted with permission from ref 97. Copyright 2018 Wiley-VCH. (k) EXAFS data of the proposed Ni−$O_4(OH)_2$ structure (inset). (l) OER polarization curves of Ni−O-G SACs and compared samples in 1 M KOH. (m) Free-energy diagrams of OER pathways and theoretical overpotential of Ni−O-G SACs, Ni−N-G SACs, and NiO nanoparticles. Adopted with permission from ref 187. Copyright 2020 by the authors.

effective suppression of the competitive HER. This was consistent with results from the aforementioned study by Sa et al.[96] that pyrrole-type Co−N_5 was the least favorable for to H* adsorption.

3.3. Ni SACs. *3.3.1. HER.* Ni SACs have been widely used for HER, in various coordination configurations in a range of substrate supports, such as graphene, graphdiyne, MoS_2, Mo_2C, etc.[97,173−184] In an early study, Qiu et al.[175] prepared Ni SAs on nanoporous graphene by the CVD and leaching method. The resulting nanocomposite exhibited an $\eta_{10,HER}$ of −50 mV in 0.5 M H_2SO_4, which was much lower than that of bulk Ni. In DFT calculations, ΔG_H in three possible coordination configurations (i.e., Ni−C_3 in the graphene lattice, Ni at the hollow site of a benzene ring, and Ni−C_2 at the defective site) were estimated and compared. The results showed that the three surrounding C atoms of Ni−C_3 had a ΔG_H similar to that of a Pt slab. Further electronic structure studies showed that Ni had a strong binding with C atoms, resulting in an empty Ni−C hybrid orbital close to the Fermi level and strong adsorption of H*, as compared to the naked

https://dx.doi.org/10.1021/acscatal.0c01950
ACS Catal. 2020, 10, 7584−7618

graphene layer. Fan et al.[180] prepared an atomic Ni−C catalyst by pyrolysis of a Ni-MOF and reached a similar conclusion that Ni SACs might be a cost-effective substitute for Pt/C toward HER. In a later study, Zhang et al.[173] utilized vacancies of defective graphene to trap Ni^{2+} ions and construct a bifunctional Ni SAC by high-temperature annealing. Notably, a divacancy-graphene defect was observed to chelate a Ni atom, as evidenced in HAADF-STEM studies (Figure 14a). Three coordination moieties were then proposed (Figure 14b) to account for the excellent HER and OER activity ($\eta_{10,HER}$ = −70 mV in 0.5 M H_2SO_4, and $\eta_{10,OER}$ = +270 mV in 1 M KOH, Figure 14c,d): Ni at the center of a benzene ring of the graphene, Ni at the center of a seven-membered C ring (aNi@D5775), Ni at the divacancy defect with a coordination of NiC_4 (aNi@Divacancy). From the free energy diagrams in Figure 14e,f, the best HER catalyst appeared to be aNi@D5775, which featured the optimal adsorption of H and highest DOS near the Fermi level, while the best OER was aNi@Divacancy, with the most optimal interaction with intermediates and the narrowest Gibbs free energy. That is, Ni−C coordination can be appealing for HER (and OER), if the location is appropriate.

Unlike conventional graphene scaffolds discussed above, Xue et al.[182] loaded zero-valence Ni SAs on graphdiyne, which showed an $\eta_{10,HER}$ of −88 mV in 0.5 M H_2SO_4, much better than that of graphdiyne alone ($\eta_{10,HER}$ = −578 mV). Two possible sites of Ni SAs were examined: the corner of the triangular lattice and the hexagonal lattice, where the former might be the anchoring site for Ni to form $Ni−C_4$ coordination based on EXAFS results. The calculation results showed that the sp-hybridized orbitals of graphdiyne had an abnormal strong overlap with the d orbitals of Ni and hence reduced the initially positively charged Ni^{2+} to Ni^0, meaning that Ni−C was due to a mutual charge overlap but not a realistic bond. With such a unique interaction, further calculations of H adsorption suggested that the nearby C atoms were the active sites for efficient HER.

In addition to these carbon-based Ni SAs, Zhang et al.[97] substituted Mo atoms on the MoS_2 nanosheet surface with Ni SAs to form isolated $Ni−S_6$ sites (Figure 14g), which exhibited an $\eta_{10,HER}$ of −161 mV in 0.5 M H_2SO_4, much lower than that of MoS_2 (−297 mV) (Figure 14h). It was found that after Ni decoration, some new hybridized electronic states were generated near the Fermi level of MoS_2 (Figure 14i), which were localized around Ni-activated S sites, leading to strengthened H binding and an enhanced HER performance, as compared with the pristine MoS_2 (Figure 14j). In another study, Wang et al.[179] deposited Ni SAs onto the basal planes or edges of MoS_2 and observed an $\eta_{10,HER}$ of −110 mV. The ΔG_H was then calculated and compared at different atomic sites, such as Ni at the top Mo site (T) or the center of the hexagonal site (H) of the MoS_2 basal plane, Ni atom at the S-edge or Mo-edge of MoS_2, and Ni substituting Mo atom of the basal plane or the edge site. The results showed that without Ni decoration, effective desorption of H_2 was difficult from the S-edge of MoS_2, but with the introduction of Ni SAs at the S-edge, the catalytic activity of the S-edge sites was significantly increased. That is, for single atoms on even the same substrate, the position of the active sites may vary, and careful characterizations are needed both experimentally and theoretically.

Note that the $Ni−N_x$ moiety can also have good catalytic activity toward OER.[163,185,186] For example, Fei et al.[163] used GO to chelate various metal ions, and thermal annealing under NH_3 gas produced various metal-N_4 moieties. Interestingly, $Ni−N_4$ had the highest activity toward OER with an $\eta_{10,OER}$ of +331 mV in 1 M KOH. DFT calculations showed that both the N and neighboring C acted as dual catalytic sites to facilitate reactions on the Ni centers, especially the OH* to O* step, where OH* was transformed into O* on the C site and then transferred to the Ni center for OOH* adsorption and release of O_2. Notably, the dual site mechanism showed a lower limiting barrier of 0.42 eV than the single-site mechanism, where OER happened solely on the Ni center of $Ni−N_4$ (1.24 eV). Similar results were obtained both experimentally and theoretically by Zhang et al.,[185] where $Ni−N_4$ moieties were anchored on N-doped carbon spheres.

The HER activity of the Ni−N−C catalysts can be further enhanced by the addition of secondary dopants. For instance, Hou et al.[186] doped S into Ni−N−C for HER in the coordination of $Ni−N_3S_1$, based on results from XAS measurements. With such a unique coordination of the Ni SAs, the catalyst delivered an $\eta_{10,HER}$ of −280 mV in alkaline media. They then estimated and compared the formation energies of all possible moieties, such as $Ni−N_4$, $Ni−N_3S_1$, $Ni−N_2S_2$, $Ni−S_1C_1$, and $Ni−N_1S_3$, and argued that $Ni−N_3S_1$ and $Ni−N_4$ represented the most thermodynamically stable structures. Additionally, the calculations showed that S and C sites neighboring the N atoms of $Ni−N_4$ and $Ni−N_3S_1$ could be ruled out because of their high free energy of OOH* generation, indicating that the Ni center alone should be the active site. Finally, $Ni−N_3S_1$ had a more favorable DOS distribution than $Ni−N_4$, because the S atom enhanced electron-transfer from Ni, leading to a lower overpotential.

Normally, O rarely appears in the coordination of SACs; yet in a recent study, Li et al.[187] prepared graphene-supported Ni SACs that were derived from NaCl-templated sucrose, and observed a relatively low $\eta_{10,HER}$ of −224 mV in alkaline media with the $Ni−O_4(OH)_2$ coordination (Figure 14k,l), in contrast to that of oxygen-deficient Ni−N−C. From the free energy diagram (Figure 14m), $Ni−O_4$-$(OH)_2$ can be seen to exhibit a lower energy barrier (0.48 eV) in the reaction pathways than both $Ni−N_4$ (1.09 eV) and bulk NiO (0.53 eV), suggesting the unique contributions of Ni−O bonds. In another study, Xu et al.[188] also found that Ni SAs coordinated to O atoms (Ni−O−C at edge sites of graphene) had a better performance than $Ni−N_4$ both in experimental measurements and DFT calculations.

3.3.2. CO_2RR. Extensive studies have been carried out with Ni SACs for CO_2RR, among which Ni−N−C typically displays a high efficiency.[189−200] Like $Fe−N_4$ and $Co−N_4$ discussed above, $Ni−N_4$ is also highly active and selective for CO_2 reduction to CO because of the low HER activity.[184] Note that the potential determining step of the overall reaction on $Ni−N_4$ is the first proton-coupling electron-transfer reaction that transforms CO_2 into COOH*. This can be mitigated by a manipulation of the coordination of the $Ni−N_x$ moieties. For example, Yan et al.[196] prepared Ni−N−C catalysts by pyrolysis of ZIF-8 containing varying ratios of Zn to Ni. The resulting samples exhibited a high Ni loading of 5.44 wt %, a high FE_{CO} of 92−98%, and a current density of 71.5 ± 2.9 mA/cm^2 at −1.03 V. They then did a detailed study of the effect of the coordination configurations on the activity and selectivity by building several models, such as $Ni−N_4$, $Ni−N_3$, $Ni−CN_3$, $Ni−N_3−V$, and $Ni−N_2−V_2$ (V denotes vacancy). The results showed that $Ni−N_4$ had the highest limiting potential but

https://dx.doi.org/10.1021/acscatal.0c01950
ACS Catal. 2020, 10, 7584−7618

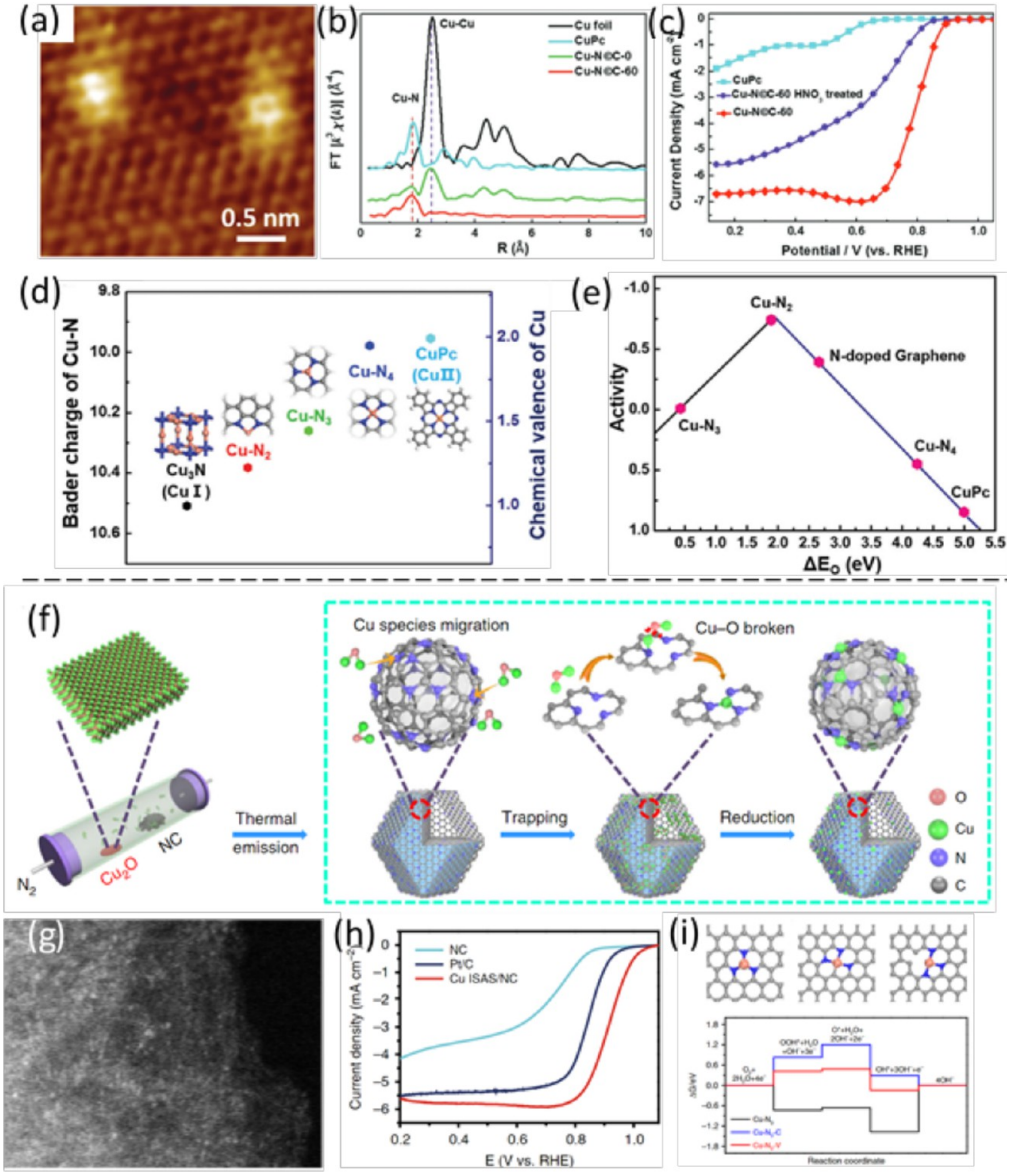

Figure 15. (a) STM image of Cu−N@C-60. (b) Cu−K edge EXAFS spectra of Cu−N©C-60 and compared samples. (c) ORR polarization curves of Cu−N©C-60, in comparison with CuPc and Cu−N©C-60 after HNO_3 treatment from the RDE test at the rotating speed of 2500 rpm and potential scan rate of 10 mV/s. (d) Bader charge (left *y*-axis) and the corresponding chemical valence (right *y*-axis) of Cu atoms in bulk Cu_3N, Cu−N©C structures (with Cu−N_2, Cu−N_3, and Cu−N_4 configurations), and CuPc molecule. (e) Volcano plot of the relationship between ORR activity and ΔE_O. Adopted with permission from ref 217. Copyright 2016 Elsevier Ltd. (f) Scheme of the formation of isolated copper sites (Cu ISAS/N−C). (g) HAADF-STEM image of Cu ISAS/NC. (h) ORR LSV curves of NC, Cu ISAS/NC, and Pt/C catalysts in 0.1 M KOH solution at the potential sweep rate of 10 mV/s and rotation rate of 1600 rpm. (i) Free energy diagram for ORR process on these three models at the equilibrium potential (U = +0.40 V or +1.23 V) at pH = 14. Adopted with permission from ref 221. Copyright 2019 Springer Nature.

lowest HER activity, while for the rest of the coordination moieties, their limiting potentials were all apparently lower, suggesting a higher CO_2RR activity. However, as Ni−N_3, Ni−N_3−V, and Ni−CN_3 also exhibited apparent activity toward HER, as compared with Ni−N_4, the corresponding FE_{CO} would be lower. Thus, the only promising coordination was Ni−N_2−V_2. The theoretical activity and selectivity of Ni−N_3−C coordination was consistent with results from another experimental study by Zhao et al.[198] It was observed that although the activity of Ni−CN_3 was very high with a current density of 10.48 mA/cm^2 V, the FE_{CO} was only 71.9% because of HER. In short, for CO_2RR catalyzed by Ni−N−C, an optimal coordination should meet the following requirements: (i) low potential barrier and (ii) low activity toward HER, as observed above with SACs based on other metal centers.

3.4. Cu SACs. Copper metalloenzymes have been widely investigated as ORR catalysts.[201,202] Typically, the unsaturated coordination of the copper centers and amino acid residues within these molecules of copper oxidases, such as laccase, ceruloplasmin, and cytochrome c, are considered as the ORR active sites.[203−206] Therefore, materials containing atomic Cu−N moieties may serve as promising alternatives to rival commercial Pt/C toward ORR. To this end, one simple method is to attach these molecules onto a support like carbon black and graphite physically for ORR electrocatalysis. For instance, Thorum et al.[207] used 3,5-diamino-1,2,4-triazole (Hdatrz) ligands to chelate two Cu(II) atoms (Cu-Hdatrz)

https://dx.doi.org/10.1021/acscatal.0c01950
ACS Catal. 2020, 10, 7584−7618

in a bridge-like fashion, where each copper center formed two Cu−N bonds with each azole molecule. After mixing with Vulcan XC-72 carbon, the resulting composite was observed to catalyze 4e$^-$ ORR with an E_{onset} of +0.86 V in alkaline media. In addition to this Cu−N_2 catalyst, other complexes with Cu−N_3, Cu−N_4, and Cu−N_5 coordination have also been studied.[208−211] However, as these catalysts are prepared by simple mixing of the copper complexes with carbon supports, the samples lack stability during electrochemical reactions, and are not sustainable for practical applications. To mitigate this issue, one plausible strategy is to incorporate the Cu−N moieties into the carbon matrix. For example, Iwase et al.[212] synthesized conductive covalent triazine frameworks (CTF) by polymerization of 2,6-dicyanopyridine. The CTF contained abundant pyridinic nitrogen to chelate metal ions by, for instance, wet impregnation. The resulting Cu-CTF nanocomposites possessed atomically dispersed Cu−N_2 and Cu−N_3 moieties, which were resolved by XAS analysis and exhibited a good ORR activity, with E_{onset} = +0.91 V in alkaline media. Cu-CTF also exhibited robust stability, where the current decreased only by 32% after 1000 CV cycles, in comparison to 94% with the Cu-Hdatrz complexes alone. DFT calculations showed that the adsorption energy of oxygen atom (ΔE_O) on the copper atom of Cu−N_2 (−4.20 eV) was slightly lower than that of a Pt slab (−4.40 eV), suggesting that these Cu−N_2 moieties were the active sites, based on the Sabatier principle. Interestingly, calculations of ΔE_O for the copper atom of Cu−N_4 macrocycle suggested that this saturated coordination corresponded to a weaker binding with oxygen atom (−2.75 eV). This was consistent with the experimental results that showed a poor activity with Cu-porphyrin or Cu-phthalocyanine (CuPc), both of which featured a coordination configuration of Cu−N_4 (pyrrole-type N).[98,99,211,213]

Both examples discussed above are based on atomic chelation of Cu(II) ions by nitrogen moieties. Yet during ORR, the Cu (II) ions may be converted to Cu(I), and studies have shown that Cu(I) is more favorable than Cu(II) for the binding and activation of O_2.[209,214−216] Within this context, Wu et al.[217] prepared N-doped carbon embedded with abundant Cu(I)-N moieties (Figure 15a) by pyrolysis of dicyandiamide (DCDA) with CuPc. XPS measurements showed that most Cu species existed as Cu(I) and had a coordination number of 2.2, as determined by XAS measurements (Figure 15b). The resulting Cu-NC catalysts exhibited an $E_{1/2}$ of ca. + 0.8 V, close to that of commercial Pt/C. Yet after oxidation of the Cu(I) species by HNO_3 to Cu(II), the $E_{1/2}$ negatively shifted by over 100 mV, meaning that Cu(I)-N was more active than Cu(II)-N toward ORR (Figure 15c). DFT study of the Bader charge (Figure 15d) suggested that the valence state of Cu atom in Cu−N_2 was close to that of bulk $Cu(I)_3N$, while Cu−N_4 had a valence state of Cu(II), no matter whether the coordinated N was pyrrole or pyridine-type. As for Cu−N_3 coordination, its valence state fell between those of Cu−N_2 and Cu−N_4, but the coordination was less stable than other configurations. Notably, Cu−N_2 was located at the summit of the Sabatier volcano plot of ΔE_O, indicating that Cu−N_2 moieties were most likely the active sites (Figure 15e). A similar conclusion was reached by Li et al.[218] They observed that the Cu−N−C catalyst even outperformed commercial Pt/C in alkaline media with an $E_{1/2}$ of +0.869 V. In DFT calculations, it was found that the adsorption of O_2 on the Cu atom of Cu−N_2 was more favorable than that of Cu−N_4. Another recent work from Wang et al.[219] also supported that Cu−N_2 at edge sites was better than Cu−N_4 moieties toward ORR. They first synthesized Cu−N−C with abundant Cu−N_4 moieties and then sulfurized the sample to produce Cu−N_2 moieties, as evidenced by XAS measurements. XPS studies demonstrated that the content of Cu(I) species increased after sulfurization. The ORR activity of the sulfurized Cu−N−C increased accordingly, as compared to the original Cu−N−C.

Interestingly, in an experimental study, Qu et al.[220] showed that Cu−N_4 moieties in pyrolyzed ZIF-8 also had an excellent ORR activity in alkaline media, with an $E_{1/2}$ of +0.895 V. XPS analysis revealed that the valence state of Cu was between 0 and 2. It should be noted that ZIF-8-derived carbons contained prevalent micropores and defects, leading to different carbon domains, as compared to graphene oxide or carbon nitride. Thus, other factors may also change the nature of the Cu−N_4 moieties toward ORR. In a recent study, Yang et al.[221] examined how the vacancy near the Cu−N active sites impacted the catalytic activity. By gas transformation (Figure 15f), Cu(I) atoms of Cu_2O were evaporated onto the defect-rich carbon skeleton of pyrolytically derived ZIF-8 to form Cu−N coordination moieties (Figure 15g), with a coordination number close to 3, as determined by EXAFS analysis. The resulting Cu−N−C nanocomposites exhibited an $E_{1/2}$ of +0.92 V in alkaline media (Figure 15h), competitive to that of state-of-the-art Fe−N−C catalysts. However, when N-doped reduced graphene oxide (N-rGO) was used as the support for Cu SAs, with a coordination number of 4 (Cu−N_4), the sample showed only a moderate activity, possibly because N-rGO did not have abundant defects like that derived from ZIF-8. In theoretical calculations (Figure 15i), the ORR activity of the Cu−N−V (vacancy, without C coordination), Cu−CN_3, and Cu−N_3 coordination was analyzed and compared, and the results showed that the formation of OOH* was the RDS of the Cu−N_3−V and Cu−CN_3 structures, whereas the removal of OH* was the RDS of Cu−N_3. In addition, the vacancy defect of Cu−N_3−V was argued to decrease the theoretical ORR overpotential (0.42 eV), which was much lower than that of Cu−CN_3 (0.83 eV) and Cu−N_3 (1.37 eV). Therefore, one can see that for a simple Cu−N−C system, the atomic coordination is capable of varying the electronic structure, leading to a change of the adsorption of oxygen species on the Cu centers. Furthermore, defects like vacancy can even alter the RDS on select Cu−N coordination, which may be exploited as a promising way to enhance the ORR activity.

The ORR performances of these Cu SACs are summarized in Table S6.

3.5. Other Metals. SACs based on other nonprecious transition metals, such as Zn,[222,223] Cr,[224] and Mo,[225] have also been used for ORR electrocatalysis. For instance, Li et al.[223] prepared Zn−N−C catalysts by pyrolysis of mixed precursors of poly(o-phenylenediamine) with $ZnCl_2$ at a slow ramping rate of 1 °C/min to retain as many Zn active sites as possible. The Zn−N−C catalyst contained mostly Zn−N_4 moieties with an ultrahigh Zn loading of 9.33 wt %, as evidenced in XAS and XPS measurements. Electrochemically, the sample exhibited a high $E_{1/2}$ of +0.873 V toward ORR in 0.1 M KOH. However, the activity remained slightly subpar as compared with that of Fe−N−C prepared in the same manner. DFT calculations showed that the Zn−N_4 moiety was less active to bind *OH, which would corrode the active sites than Fe−N_4, and hence was more anticorrosive and stable. In another study, Luo et al.[224] annealed Cr-soaked ZIF-8 to yield Cr SACs with Cr−N_4

https://dx.doi.org/10.1021/acscatal.0c01950
ACS Catal. 2020, 10, 7584−7618

coordination, and observed an $E_{1/2}$ of +0.773 V in acid and superb stability with only a 15 mV shift of $E_{1/2}$ after 20 000 CV cycles.

Mo SACs have also been used toward oxygen reduction for H_2O_2 production. Tang et al.[225] embedded a high loading of Mo SAs (13.47 wt %) into porous O,S-codoped graphene by MgO-templated pyrolysis and leaching treatment and observed a high H_2O_2 selectivity over 95% in 0.1 M KOH. XAS studies resolved that the Mo SAs were in a mixture of Mo−O and Mo−S coordination. In DFT calculations, three coordination types (i.e., Mo−O_4, Mo−S_4, and Mo−O_3S on a graphene layer) were examined and compared in terms of their adsorption energy of *OOH. Surprisingly, the active site was found to be the neighboring C atom of the six-membered ring (coordinated with S), which was activated by the electrons donated from the Mo atom upon the adsorption of OOH*. While Mo−O_4 has the highest free energy of OOH* adsorption, the adsorption energy on the C site decreased to 0.35 eV when one O atom was substituted by S to form Mo−O_3-S, suggesting more favorable adsorption for OOH*. As for the fully S coordinated Mo−S_4, the adsorption energy was decreased further to 0.14 eV. These results indicate that sometimes transition metal atoms do not need to be the active sites, but they can activate surrounding nonmetal sites to be the active sites.

Mn SACs have also been prepared and used as high-performance catalysts for ORR, OER, and CO_2RR.[226−228] Similar to Fe and Co, carbon composites loaded with abundant Mn−N moieties were found to exhibit an apparent ORR activity ($E_{1/2}$ = +0.80 V) in acidic media that was comparable to that of commercial Pt/C, as manifested in a recent study by Wu and co-workers.[228] DFT studies were then carried out to screen nine possible Mn−N_xC structures, and Mn−N_4 (pyrrolic N) was identified as the optimal active sites, consistent with results from XAS analysis. In another study by Guan et al.,[226] Mn SAs were loaded onto the N-doped graphene forming Mn−N_4 moieties, which was evidenced by HAADF-STEM and EXAFS measurements (Figure 16a−c). The resulting samples were then used as OER catalysts for water oxidation, displaying an $\eta_{10,OER}$ of +337 mV in 1.0 M KOH (Figure 16d). In DFT calculations, various coordination structures, including Mn−N_4, Mn−N_3, Mn−O_3, Mn_3N_7, and Mn phthalocyanine, were examined and compared in terms of the theoretical overpotential of the OER pathways. The results showed that the Mn center of Mn−N_4 had the lowest equilibrium potential (0.45 V) among these structures for the potential-determining step.

In another study of Mn SACs, Zhang et al.[227] showed that whereas bare Mn−N_4 moieties might not be suitable for the CO_2RR catalysis, an additional Cl^- that was axially attached to the Mn center could lead to an appreciable CO_2RR activity. The catalysts derived from pyrolysis of crystalline Mn-ethylenediamine-Cl polymer indeed were successfully embedded with Mn−N_4−Cl moieties (Figure 16e), as manifested in EXAFS measurements and exhibited a high activity toward CO_2RR with a FE_{CO} of 97% and a low potential of −0.49 V to reach 10 mA/cm^2 (Figure 16f), which was much better than Mn−N−C without the Cl dopants. In DFT calculations, Mn−N_4 and Mn−N_4Cl coordination structures were examined within the context of the adsorption energies of CO_2 and COOH* intermediate (Figure 16g). Mn−N_4−Cl was more favorable for COOH* adsorption, exhibited a decrease of CO desorption free energy and hence was more effective than

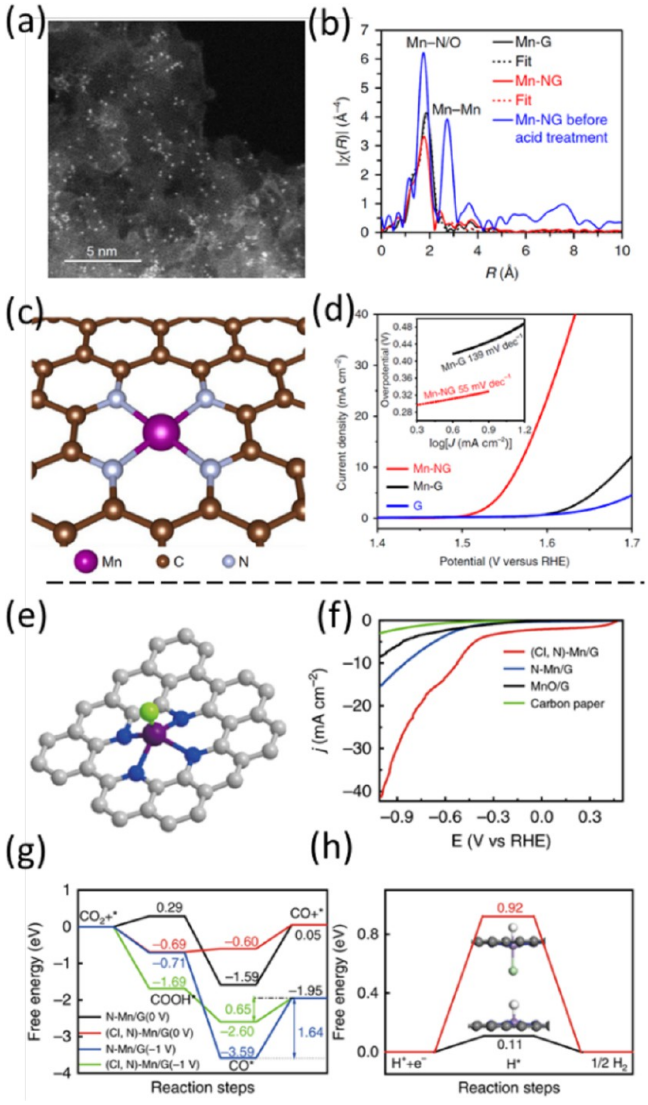

Figure 16. (a) HAADF-STEM image of Mn-NG. (b) EXAFS spectra and fitting data of Mn-NG samples. (c) Atomic model of Mn−N_4 moiety. (d) OER LSV curves of Mn-NG and compared samples in 1.0 M KOH at the scan rate of 5 mV/s, with Tafel plots shown in the inset. Adopted with permission from ref 226. Copyright 2018 Elsevier Ltd. (e) Schematic model of (Cl, N)-Mn/G: Mn (purple), Cl (green), N (blue), and C (gray). (f) CO_2RR LSV curves of (Cl, N)-Mn/G catalyst and compared samples in a CO_2-saturated 0.5 M $KHCO_3$ solution at the potential scan rate of 10 mV/s. (g) Calculated free energy of CO_2RR and (h) calculated free energy of hydrogen adsorption for Mn−N with/without axial Cl atom. Adopted with permission from ref 227. Copyright 2019 Springer Nature.

Mn−N_4 toward CO_2RR. Further calculations (Figure 16h) revealed that Mn−N_4Cl was less favorable for H* adsorption than Mn−N_4, suggesting that the HER interference was less significant on the former than on the latter. From the results of the electronic structure, it was found that the coordination of Cl shifted the d-band center of the Mn−N_4 moiety and hence varied the electron-transfer property.

One may note that nearly all cases discussed above are SACs based on transition metals because of their unique d-orbitals. Interestingly, SACs based on select main-group metals can also exhibit apparent ORR cactivity.[229,230] For example, Qin et al.[229] annealed an Al-hydroxyquinoline complex with N-doped graphene to fabricate an Al−N−C catalyst, whose ORR

https://dx.doi.org/10.1021/acscatal.0c01950
ACS Catal. 2020, 10, 7584−7618

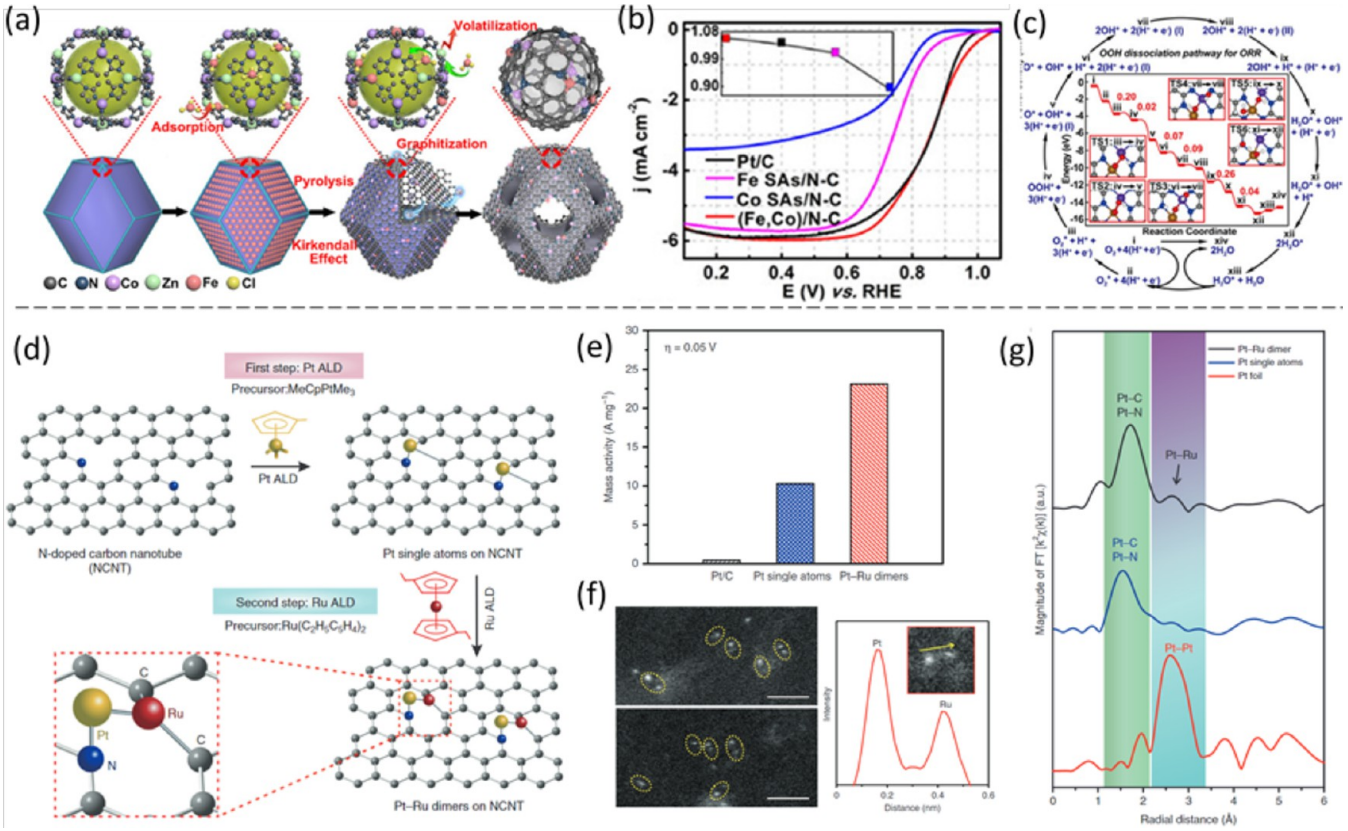

Figure 17. (a) Schematic of the preparation of (Fe,Co)/N−C. (b) ORR polarization curves of (Fe,Co)/N−C and compared samples in O_2-saturated 0.1 M $HClO_4$ at the potential sweep rate of 10 mV/s and rotation speed of 1600 rpm. Inset lists the onset potentials of the varied catalysts. (c) Calculated energies of intermediates and transition states in ORR at (Fe,Co)/N−C. Adopted with permission from ref 231. Copyright 2017 American Chemical Society. (d) Schematic illustration of ALD synthesis of Pt−Ru dimers on N-doped CNTs. (e) Normalized mass activity at 0.05 V of Pt−Ru dimers, Pt SAs and commercial Pt/C in 0.5 M H_2SO_4. (f) HAADF-STEM images of Pt−Ru dimers/NCNTs (scale bar 1 nm) and the EDS intensity profile obtained on one Pt−Ru dimer. (g) FT-EXAFS spectra of the Pt−Ru dimers, Pt SAs and Pt foil. Adopted with permission from ref 240. Copyright 2019 Springer Nature.

activity even rivaled that of Pt/C with an $E_{1/2}$ of +0.85 V in 0.1 M KOH. Although structural characterization of the atomic structures remained incomplete, DFT calculations probed 10 structures, including Al−N_4, Al−C_4, Al−C_3N_1, and Al−C_3N_1 with a pore defect. The results suggested that the Al center of Al−C_3N_1 coordination with the defect was the most promising one to account for the ORR activity. In another study, Liu et al.[230] first carried out DFT simulations to inspect Mg, Ca, and Al coordinated with various numbers of pyridinic N atoms (M-N_xC, where x varied from 1 to 4) for ORR. It was found that transformation from O_2 to OOH* on Mg and Al sites was exothermic, and adsorption of OH* on Al and Ca was much stronger than that of Mg, meaning that Mg might be the most suitable one for ORR. Further trials to optimize Mg−N_xC coordination revealed that Mg−N_2 (two diagonal pyridinic N) had an onset potential of +0.77 V, close to that of Pt(111) (+0.83 V). Unlike other Mg−N_xC coordination structures, when OH* was adsorbed onto Mg−N_2, the p-band center became closer to the Fermi level, resulting in weaker adsorption of *OH. Based on these theoretical results, they synthesized Mg−N−C catalysts by direct pyrolysis of a Mg-based MOF and measured the ORR activity in 0.1 M KOH, which showed an excellent $E_{1/2}$ of +0.91 V, and only a negligible decline after 5000 CV cycles.

The electrocatalytic performances of these non-noble SACs toward water splitting and CO_2RR are summarized in Table S7 and Table S8, respectively.

4. DUAL METAL CENTERS

The activity of atomically dispersed metal catalysts can be further enhanced by the incorporation of a second metal atom to form a dual-metal site, where the electronic interactions between the two metal centers can be exploited to manipulate the interactions with important reaction intermediates and hence the electrocatalytic activity.

As mentioned above, a range of SACs have been demonstrated for alkaline ORR, such as Fe, Co, and Cu. However, the catalytic activity in acid remains subpar, as compared with commercial Pt/C. To tackle this issue, dual metal catalysts, such as Fe−Co,[231,232] Co−Co,[233] Fe−Fe,[234] Fe−Mn,[235,236] Co−Pt,[237] and Zn−Co,[238,239] have been developed. For example, Wang et al.[231] prepared N_3−Fe−Co−N_3 dual-metal moieties based on bimetal ZIF using a host−guest strategy (Figure 17a). The resulting dual-atom catalysts showed an ORR activity in alkaline media that was comparable to that of commercial Pt/C but markedly higher ($E_{1/2}$ = +0.863, Figure 17b) than that of Fe−N_x-C and Co−N_x-C. DFT calculations (Figure 17c) showed that the bridge-like adsorption of O_2 molecules was the preferable mode on the Fe−Co atom pair, leading to an enhanced dissociation of

https://dx.doi.org/10.1021/acscatal.0c01950
ACS Catal. 2020, 10, 7584−7618

Scheme 1. Jacob's Ladder of the Development of SACs toward Electrochemical Reactions

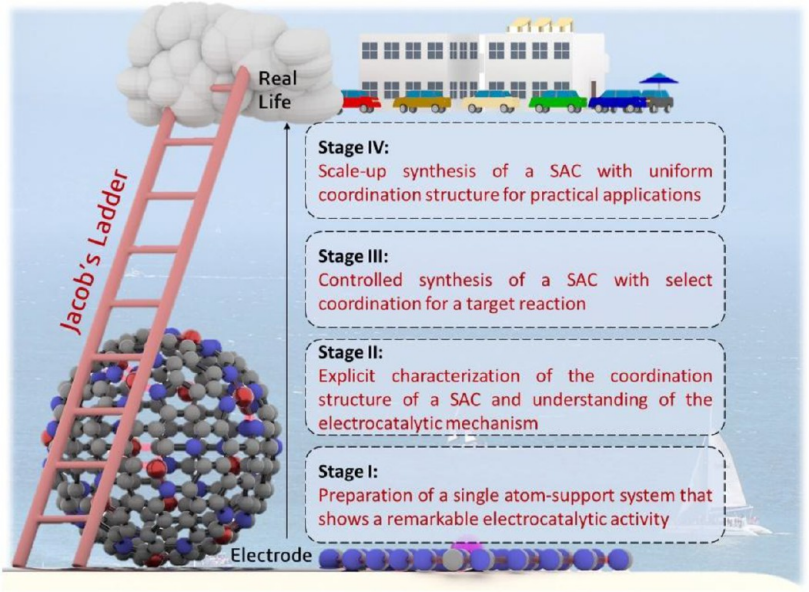

the O atoms and the $4e^-$ reduction pathway. Similarly, by using bi/trinuclear Fe complexes, Ye et al.[234] synthesized precisely paired N_3−Fe−Fe−N_3 moieties on N-doped carbon, which also exhibited a better ORR performance than the corresponding Fe SACs. Low-temperature infrared spectroscopic measurement showed that the number of Fe sites influenced O_2 adsorption, where the Fe_2−N moieties showed a bridge-like oxo configuration and Fe_1−N had a superoxide-like mode. The calculations also showed easier cleavage of O_2 on dual sites than on the single ones because of the elongation of the O−O bonds. Similar behaviors were observed with Co_2−N_5 dual-atom moieties by Xiao et al.[233] and N_3−Zn−Co−N_3 coordination by Lu et al.[238]

For water-splitting electrocatalysis, dual-atom catalysts also exhibit apparent enhancement. In a recent study, Zhang et al.[240] assembled Pt−Ru dual-metal dimers onto N-doped CNTs by two steps of ALD (Figure 17d), and observed a much higher HER mass activity (23 100 A/g at the overpotential of −0.05 V, Figure 17e) than that of Pt SAC (ca. 10 000 A/g) or commercial Pt/C (430 A/g). The dimer was argued to have a coordination of N−Pt−Ru−C_2, based on HAADF-STEM and EXAFS measurements (Figure 17f,g). Calculations of this coordination revealed that the Pt−Ru dimer facilitated the adsorption of H atoms, as compared with conventional nanoparticles, which remain stable even after the adsorption of six H atoms to form a Pt(3H)-Ru(3H) structure. It was found that such a high H coverage was favorable for the further desorption of H_2 with a low ΔG_H of 0.01 eV because of the interaction between the d_{xz} orbital of the Ru atom and the adsorbed H atom, while the Pt−Pt dimer (close to bulk Pt) was inferior with a ΔG_H of −0.14 eV. Moreover, the Pt−Ru dimer was found to have more unoccupied states that would reduce ΔG_H, another factor for enhanced HER activity.

Dual atom catalysts have also been used for the OER. In a combined experiment−theory study, Han et al.[241] observed that the N_3−Co−Ni−N_3 coordination was better than Ni−N_4 or Co−N_4 toward OER because of a reduced energy barrier of OH* adsorption. In another study with Co−Fe double-atom catalysts, Bai et al.[242] found that the overpotential of Co−N−C catalysts was lowered after activation because of the trace amount of Fe ions in commercial KOH, which formed oxo-like Co−O_2−Fe coordination (two separate O atoms bridging Co and Fe), as confirmed by operando XAS measurements. Despite no direct bond between Fe and Co, the catalyst still demonstrated a superior OER activity with an $\eta_{10,OER}$ of +309 mV in Fe-containing KOH, which was much better than that of Co−N−C in Fe-free KOH (+443 mV).

The design of dual-atom catalysts is also indispensable for the development CO_2RR catalysts.[243−245] Note that Ni−N_x exhibits a high current density for CO production from CO_2 reduction, but it has sluggish kinetics for the first proton-coupled step of reduction. In contrast, Fe−N_x has a low onset potential, but a poor desorption ability of CO*. Ren et al.[243] thus complementarily combined Fe and Ni into diatomic Ni−Fe moieties with a possible coordination of N_3−Ni−Fe−N_3, which indeed showed a higher FE_{CO} across the entire potential window (maximum 98%) and higher current density of CO generation (7.4 mA/cm at −0.7 V) than Ni−N−C (1.5 times lower) and Fe−N−C (4.6 times lower). Further mechanistic study showed that although Ni−Fe dual sites might be passivated by one CO* at first like Fe−N−C, the metal center that remained free could still provide an adsorption site for the second CO_2 activation by the geometric effect of the dual sites to the adsorbed species, leading to a lower theoretical overpotential than the Fe or Ni single sites. In a latest study, Zhu et al.[244] constructed neighboring Zn/Co monomers in a coordination of N_2−Zn-N_2−Co−N_2 (without direct Zn−Co bonding), and showed that the Zn site of the N_2−Zn-N_2−Co-N_2 moiety was the key active site for the reduction of CO_2, which could overcome the difficulty of COOH* adsorption on Zn single sites, and CO* desorption and HER competition on Co single sites, thus leading to a better performance than that by Zn−N−C or Co−N−C single-site catalysts.

The ORR activities of select dual-metal SACs are summarized in Table S9.

5. SUMMARY AND PERSPECTIVES

Thus far, significant progress has been made where SACs based on noble and non-noble metals on a variety of supporting substrates can be readily prepared as viable

https://dx.doi.org/10.1021/acscatal.0c01950
ACS Catal. 2020, 10, 7584−7618

candidates to rival conventional nanoparticle-based catalysts in diverse electrochemical energy technologies. One key result is that the SAC active sites, and hence electrocatalytic activity and selectivity, are dictated by the atomic configuration of the metal site coordination structure. Such fundamental insights are critical in the further enhancement of the electrocatalytic performance of SACs.[246−249] The roadmap can be schematically illustrated with a Jacob's ladder (Scheme 1).

The current progress on SAC research is mostly on stage I and II. On stage I, the concept of SACs has been demonstrated with a select group of metal species that can be prepared by facile procedures, such as pyrolysis, coprecipitation, wet impregnation, etc. To understand the mechanistic origin of the electrocatalytic activity, identification of the atomic configuration of the coordination moieties represents a critical first step. This is the focus of stage II. However, most SAC samples involve very complex coordination structures, making it challenging to unambiguously correlate the electrocatalytic activity with specific coordination structures. Indeed this has created uncertainties, and sometimes conflicting results, in unraveling the catalytic active sites.

Therefore, to progress into stage III, new chemistries need to be developed so that SACs with a relatively defined or controllable coordination structure can be obtained. Toward this end, the choice of metal precursors is an important factor. In a number of prior studies, a metal−porphyrin complex is used as a precursor to prepare M−N_4 sites in the carbon matrix.[96,122−125,142] With a deliberate selection of the metal precursors, it becomes possible to retain the coordination structure in the final products after pyrolysis treatment.[234] Construction of a structural vacancy of the supporting substrates represents another key variable, as vacancies and defects are the preferred sites for the capturing and stabilization of the metal centers.[59,250,251] Furthermore, engineering of the specific morphologies near the single-atom sites may be an effective strategy in manipulating the structure and activity of SACs.[23,127,252] With a clearly defined coordination configuration, the electronic structure of the SACs can be accurately examined by first-principles quantum calculations, where the interactions of various atomic sites with important reaction intermediates can be evaluated, leading to an unambiguous identification of the reaction pathway and mechanism. It is noticeable that a metal SA is usually chelated to atoms of high electronegativity in the supporting substrate, where the ensuing charge transfer is analogous to the conventional metal−ligand charge transfer (MLCT). This is the driving force in activating the metal centers and adjacent (nonmetal) atoms for electrocatalytic reactions.[19,22,95,97,155]

Success of stage III will render it possible to prepare SACs with a specific coordination structure for select reactions. Such designer chemistry will drastically enhance the utilization efficiency of catalyst materials,[75,121,253] and lay a solid foundation for large-scale synthesis of SACs for specific applications (stage IV).

Certainly, climbing up the Jacob's ladder will necessitate significant advances and breakthroughs from both the experimental and theoretical perspectives, where their deliberate integration is key to the rational design and engineering of next-generation SACs. In particular, operando characterization of SACs will be of critical importance to unravel the dynamic nature of the atomic configurations of the coordination moieties during electrochemical reactions, such that the reaction mechanism and catalyst stability can be evaluated in real time.[164] In addition, new computational methods and enhanced capacity are needed to accommodate a structural model that mimics the actual catalyst sample, such that the energetic characteristics of important reaction intermediates and transition states can be accurately analyzed, and the impacts of electrolyte solvation and electrochemical potential on the electrocatalytic activity can be fully addressed.[254]

■ ASSOCIATED CONTENT

Supporting Information

The Supporting Information is available free of charge at https://pubs.acs.org/doi/10.1021/acscatal.0c01950.

Nine tables to summarize the electrocatalytic activities toward varied reactions (PDF)

■ AUTHOR INFORMATION

Corresponding Author

Shaowei Chen − *Department of Chemistry and Biochemistry, University of California, Santa Cruz, California 95064, United States;* orcid.org/0000-0002-3668-8551; Email: shaowei@ucsc.edu

Authors

Bingzhang Lu − *Department of Chemistry and Biochemistry, University of California, Santa Cruz, California 95064, United States*

Qiming Liu − *Department of Chemistry and Biochemistry, University of California, Santa Cruz, California 95064, United States;* orcid.org/0000-0001-5839-5453

Complete contact information is available at: https://pubs.acs.org/10.1021/acscatal.0c01950

Author Contributions

†(B.L., Q.L.) These authors contributed equally to this work. The manuscript was written through contributions of all authors. All authors have given approval to the final version of the manuscript.

Notes

The authors declare no competing financial interest.

■ ACKNOWLEDGMENTS

This work was supported in part by the National Science Foundation (CHE-1900235 and CBET-1848841). B.Z.L. acknowledges support of a Sigma Xi student grant-in-aid (G201903158663319) and a UCSC Chancellor's Dissertation Year Fellowship.

■ REFERENCES

(1) Jin, H.; Guo, C.; Liu, X.; Liu, J.; Vasileff, A.; Jiao, Y.; Zheng, Y.; Qiao, S. Z. Emerging Two-Dimensional Nanomaterials for Electrocatalysis. *Chem. Rev.* **2018**, *118*, 6337−6408.

(2) Li, W.; Liu, J.; Zhao, D. Mesoporous Materials for Energy Conversion and Storage Devices. *Nat. Rev. Mater.* **2016**, *1*, 16023.

(3) Ramaswamy, N.; Mukerjee, S. Alkaline Anion-Exchange Membrane Fuel Cells: Challenges in Electrocatalysis and Interfacial Charge Transfer. *Chem. Rev.* **2019**, *119*, 11945−11979.

(4) Hwang, J.; Rao, R. R.; Giordano, L.; Katayama, Y.; Yu, Y.; Shao-Horn, Y. Perovskites in Catalysis and Electrocatalysis. *Science* **2017**, *358*, 751−756.

(5) Seh, Z. W.; Kibsgaard, J.; Dickens, C. F.; Chorkendorff, I.; Norskov, J. K.; Jaramillo, T. F. Combining Theory and Experiment in

Electrocatalysis: Insights into Materials Design. *Science* **2017**, *355*, No. eaad4998.
(6) Xia, Z.; Guo, S. Strain Engineering of Metal-Based Nanomaterials for Energy Electrocatalysis. *Chem. Soc. Rev.* **2019**, *48*, 3265−3278.
(7) Gu, J.; Hsu, C. S.; Bai, L.; Chen, H. M.; Hu, X. Atomically Dispersed Fe(3+) Sites Catalyze Efficient CO_2 Electroreduction to Co. *Science* **2019**, *364*, 1091−1094.
(8) Shao, M.; Chang, Q.; Dodelet, J. P.; Chenitz, R. Recent Advances in Electrocatalysts for Oxygen Reduction Reaction. *Chem. Rev.* **2016**, *116*, 3594−657.
(9) Shi, Y.; Zhang, B. Recent Advances in Transition Metal Phosphide Nanomaterials: Synthesis and Applications in Hydrogen Evolution Reaction. *Chem. Soc. Rev.* **2016**, *45*, 1529−1541.
(10) Guo, S. J.; Zhang, S.; Sun, X. L.; Sun, S. H. Synthesis of Ultrathin Feptpd Nanowires and Their Use as Catalysts for Methanol Oxidation Reaction. *J. Am. Chem. Soc.* **2011**, *133*, 15354−15357.
(11) Boronat-Gonzalez, A.; Herrero, E.; Feliu, J. M. Heterogeneous Electrocatalysis of Formic Acid Oxidation on Platinum Single Crystal Electrodes. *Curr. Opin. Electrochem.* **2017**, *4*, 26−31.
(12) Peng, Y.; Lu, B. Z.; Chen, S. W. Carbon-Supported Single Atom Catalysts for Electrochemical Energy Conversion and Storage. *Adv. Mater.* **2018**, *30*, 1801995.
(13) Yang, X. F.; Wang, A. Q.; Qiao, B. T.; Li, J.; Liu, J. Y.; Zhang, T. Single-Atom Catalysts: A New Frontier in Heterogeneous Catalysis. *Acc. Chem. Res.* **2013**, *46*, 1740−1748.
(14) Chen, Y. J.; Ji, S. F.; Chen, C.; Peng, Q.; Wang, D. S.; Li, Y. D. Single-Atom Catalysts: Synthetic Strategies and Electrochemical Applications. *Joule* **2018**, *2*, 1242−1264.
(15) Shen, R.; Chen, W.; Peng, Q.; Lu, S.; Zheng, L.; Cao, X.; Wang, Y.; Zhu, W.; Zhang, J.; Zhuang, Z.; Chen, C.; Wang, D.; Li, Y. High-Concentration Single Atomic Pt Sites on Hollow Cusx for Selective O2 Reduction to H_2O_2 in Acid Solution. *Chem.* **2019**, *5*, 2099−2110.
(16) Lin, L. L.; Zhou, W.; Gao, R.; Yao, S. Y.; Zhang, X.; Xu, W. Q.; Zheng, S. J.; Jiang, Z.; Yu, Q. L.; Li, Y. W.; Shi, C.; Wen, X. D.; Ma, D. Low-Temperature Hydrogen Production from Water and Methanol Using Pt/Alpha-MoC Catalysts. *Nature* **2017**, *544*, 80−83.
(17) Gao, C.; Chen, S. M.; Wang, Y.; Wang, J. W.; Zheng, X. S.; Zhu, J. F.; Song, L.; Zhang, W. K.; Xiong, Y. J. Heterogeneous Single-Atom Catalyst for Visible-Light-Driven High-Turnover CO_2 Reduction: The Role of Electron Transfer. *Adv. Mater.* **2018**, *30*, 1704624.
(18) Qiao, B. T.; Wang, A. Q.; Yang, X. F.; Allard, L. F.; Jiang, Z.; Cui, Y. T.; Liu, J. Y.; Li, J.; Zhang, T. Single-Atom Catalysis of Co Oxidation Using Pt-1/FeO_x. *Nat. Chem.* **2011**, *3*, 634−641.
(19) Li, J. C.; Maurya, S.; Kim, Y. S.; Li, T.; Wang, L. G.; Shi, Q. R.; Liu, D.; Feng, S.; Lin, Y. H.; Shao, M. H. Stabilizing Single-Atom Iron Electrocatalysts for Oxygen Reduction Via Ceria Confining and Trapping. *ACS Catal.* **2020**, *10*, 2452−2458.
(20) Chen, P. Z.; Zhou, T. P.; Xing, L. L.; Xu, K.; Tong, Y.; Xie, H.; Zhang, L. D.; Yan, W. S.; Chu, W. S.; Wu, C. Z.; Xie, Y. Atomically Dispersed Iron-Nitrogen Species as Electrocatalysts for Bifunctional Oxygen Evolution and Reduction Reactions. *Angew. Chem., Int. Ed.* **2017**, *56*, 610−614.
(21) Chen, Y. J.; Ji, S. F.; Wang, Y. G.; Dong, J. C.; Chen, W. X.; Li, Z.; Shen, R. A.; Zheng, L. R.; Zhuang, Z. B.; Wang, D. S.; Li, Y. D. Isolated Single Iron Atoms Anchored on N-Doped Porous Carbon as an Efficient Electrocatalyst for the Oxygen Reduction Reaction. *Angew. Chem., Int. Ed.* **2017**, *56*, 6937−6941.
(22) Lu, B. Z.; Smart, T. J.; Qin, D. D.; Lu, J. E.; Wang, N.; Chen, L. M.; Peng, Y.; Ping, Y.; Chen, S. W. Nitrogen and Iron-Codoped Carbon Hollow Nanotubules as High-Performance Catalysts toward Oxygen Reduction Reaction: A Combined Experimental and Theoretical Study. *Chem. Mater.* **2017**, *29*, 5617−5628.
(23) He, T.; Zhang, Y. Q.; Chen, Y.; Zhang, Z. Z.; Wang, H. Y.; Hu, Y. F.; Liu, M.; Pao, C. W.; Chen, J. L.; Chang, L. Y.; Sun, Z. F.; Xiang, J.; Zhang, Y.; Chen, S. W. Single Iron Atoms Stabilized by Microporous Defects of Biomass-Derived Carbon Aerogels as High-Performance Cathode Electrocatalysts for Aluminum-Air Batteries. *J. Mater. Chem. A* **2019**, *7*, 20840−20846.
(24) Chen, Y. X.; Huang, Z. W.; Ma, Z.; Chen, J. M.; Tang, X. F. Fabrication, Characterization, and Stability of Supported Single-Atom Catalysts. *Catal. Sci. Technol.* **2017**, *7*, 4250−4258.
(25) Tang, Y.; Zhao, S.; Long, B.; Liu, J. C.; Li, J. On the Nature of Support Effects of Metal Dioxides MO_2 (M = Ti, Zr, Hf, Ce, Th) in Single-Atom Gold Catalysts: Importance of Quantum Primogenic Effect. *J. Phys. Chem. C* **2016**, *120*, 17514−17526.
(26) Wang, Q.; Huang, X.; Zhao, Z. L.; Wang, M. Y.; Xiang, B.; Li, J.; Feng, Z. X.; Xu, H.; Gu, M. Ultrahigh-Loading of Ir Single Atoms on Nio Matrix to Dramatically Enhance Oxygen Evolution Reaction. *J. Am. Chem. Soc.* **2020**, *142*, 7425−7433.
(27) Shi, Q.; Hwang, S.; Yang, H.; Ismail, F.; Su, D.; Higgins, D.; Wu, G. Supported and Coordinated Single Metal Site Electrocatalysts. *Mater. Today* **2020**, DOI: 10.1016/j.mattod.2020.02.019.
(28) Zhu, Y. Z.; Sokolowski, J.; Song, X. C.; He, Y. H.; Mei, Y.; Wu, G. Engineering Local Coordination Environments of Atomically Dispersed and Heteroatom-Coordinated Single Metal Site Electrocatalysts for Clean Energy-Conversion. *Adv. Energy Mater.* **2020**, *10*, 1902844.
(29) Chen, M. J.; He, Y. H.; Spendelow, J. S.; Wu, G. Atomically Dispersed Metal Catalysts for Oxygen Reduction. *ACS Energy Lett.* **2019**, *4*, 1619−1633.
(30) He, Y.; Liu, S.; Priest, C.; Shi, Q.; Wu, G. Atomically Dispersed Metal-Nitrogen-Carbon Catalysts for Fuel Cells: Advances in Catalyst Design, Electrode Performance, and Durability Improvement. *Chem. Soc. Rev.* **2020**, *49*, 3484.
(31) Zhao, C. X.; Li, B. Q.; Liu, J. N.; Zhang, Q. Intrinsic Electrocatalytic Activity Regulation of M-N-C Single-Atom Catalysts for Oxygen Reduction Reaction. *Angew. Chem., Int. Ed.* **2020**, DOI: 10.1002/anie.202003917.
(32) Zhu, C. Z.; Fu, S. F.; Shi, Q. R.; Du, D.; Lin, Y. H. Single-Atom Electrocatalysts. *Angew. Chem., Int. Ed.* **2017**, *56*, 13944−13960.
(33) Ji, S.; Chen, Y.; Wang, X.; Zhang, Z.; Wang, D.; Li, Y. Chemical Synthesis of Single Atomic Site Catalysts. *Chem. Rev.* **2020**, DOI: 10.1021/acs.chemrev.9b00818.
(34) Lin, C.; Zhao, Y. H.; Zhang, H. J.; Xie, S. H.; Li, Y. F.; Li, X. P.; Jiang, Z.; Liu, Z. P. Accelerated Active Phase Transformation of Nio Powered by Pt Single Atoms for Enhanced Oxygen Evolution Reaction. *Chem. Sci.* **2018**, *9*, 6803−6812.
(35) Pu, Z. H.; Amiinu, I. S.; Cheng, R. L.; Wang, P. Y.; Zhang, C. T.; Mu, S. C.; Zhao, W. Y.; Su, F. M.; Zhang, G. X.; Liao, S. J.; Sun, S. H. Single-Atom Catalysts for Electrochemical Hydrogen Evolution Reaction: Recent Advances and Future Perspectives. *Nano-Micro Lett.* **2020**, *12*, 29.
(36) Liu, H. X.; Peng, X. Y.; Liu, X. J. Single-Atom Catalysts for the Hydrogen Evolution Reaction. *ChemElectroChem* **2018**, *5*, 2963−2974.
(37) Yin, X. P.; Wang, H. J.; Tang, S. F.; Lu, X. L.; Shu, M.; Si, R.; Lu, T. B. Engineering the Coordination Environment of Single-Atom Platinum Anchored on Graphdiyne for Optimizing Electrocatalytic Hydrogen Evolution. *Angew. Chem., Int. Ed.* **2018**, *57*, 9382−9386.
(38) Li, T. F.; Liu, J. J.; Song, Y.; Wang, F. Photochemical Solid-Phase Synthesis of Platinum Single Atoms on Nitrogen-Doped Carbon with High Loading as Bifunctional Catalysts for Hydrogen Evolution and Oxygen Reduction Reactions. *ACS Catal.* **2018**, *8*, 8450−8458.
(39) Liu, W.; Xu, Q.; Yan, P. F.; Chen, J.; Du, Y.; Chu, S. Q.; Wang, J. O. Fabrication of a Single-Atom Platinum Catalyst for the Hydrogen Evolution Reaction: A New Protocol by Utilization of H_xMo_{3-x} with Plasmon Resonance. *ChemCatChem* **2018**, *10*, 946−950.
(40) Chen, Y. N.; Zhang, X.; Zhou, Z. Carbon-Based Substrates for Highly Dispersed Nanoparticle and Even Single-Atom Electrocatalysts. *Small Methods* **2019**, *3*, 1900050.
(41) Lei, Y.; Wang, Y.; Liu, Y.; Song, C.; Li, Q.; Wang, D.; Li, Y. Realizing the Atomic Active Center for Hydrogen Evolution Electrocatalysts. *Angew. Chem., Int. Ed.* **2020**, DOI: 10.1002/anie.201914647.

(42) Fei, H. L.; Dong, J. C.; Chen, D. L.; Hu, T. D.; Duan, X. D.; Shakir, I. R.; Huang, Y.; Duan, X. F. Single Atom Electrocatalysts Supported on Graphene or Graphene-Like Carbons. *Chem. Soc. Rev.* **2019**, *48*, 5207−5241.
(43) Cheng, N. C.; Stambula, S.; Wang, D.; Banis, M. N.; Liu, J.; Riese, A.; Xiao, B. W.; Li, R. Y.; Sham, T. K.; Liu, L. M.; Botton, G. A.; Sun, X. L. Platinum Single-Atom and Cluster Catalysis of the Hydrogen Evolution Reaction. *Nat. Commun.* **2016**, *7*, 13638.
(44) Liu, D. B.; Li, X. Y.; Chen, S. M.; Yan, H.; Wang, C. D.; Wu, C. Q.; Haleem, Y. A.; Duan, S.; Lu, J. L.; Ge, B. H.; Ajayan, P. M.; Luo, Y.; Jiang, J.; Song, L. Atomically Dispersed Platinum Supported on Curved Carbon Supports for Efficient Electrocatalytic Hydrogen Evolution. *Nat. Energy* **2019**, *4*, 512−518.
(45) Ji, J. P.; Zhang, Y. P.; Tang, L. B.; Liu, C. Y.; Gao, X. H.; Sun, M. H.; Zheng, J. C.; Ling, M.; Liang, C. D.; Lin, Z. Platinum Single-Atom and Cluster Anchored on Functionalized MWCNTs with Ultrahigh Mass Efficiency for Electrocatalytic Hydrogen Evolution. *Nano Energy* **2019**, *63*, 103849.
(46) Yan, Q. Q.; Wu, D. X.; Chu, S. Q.; Chen, Z. Q.; Lin, Y.; Chen, M. X.; Zhang, J.; Wu, X. J.; Liang, H. W. Reversing the Charge Transfer between Platinum and Sulfur-Doped Carbon Support for Electrocatalytic Hydrogen Evolution. *Nat. Commun.* **2019**, *10*, 4977.
(47) Kwon, H. C.; Kim, M.; Grote, J. P.; Cho, S. J.; Chung, M. W.; Kim, H.; Won, D. H.; Zeradjanin, A. R.; Mayrhofer, K. J. J.; Choi, M.; Kim, H.; Choi, C. H. Carbon Monoxide as a Promoter of Atomically Dispersed Platinum Catalyst in Electrochemical Hydrogen Evolution Reaction. *J. Am. Chem. Soc.* **2018**, *140*, 16198−16205.
(48) Zhang, J. Q.; Zhao, Y. F.; Guo, X.; Chen, C.; Dong, C. L.; Liu, R. S.; Han, C. P.; Li, Y. D.; Gogotsi, Y.; Wang, G. X. Single Platinum Atoms Immobilized on an Mxene as an Efficient Catalyst for the Hydrogen Evolution Reaction. *Nat. Catal.* **2018**, *1*, 985−992.
(49) Zhang, L.; Liu, H. S.; Liu, S. H.; Banis, M. N.; Song, Z. X.; Li, J. J.; Yang, L. J.; Markiewicz, M.; Zhao, Y.; Li, R. Y.; Zheng, M.; Ye, S. Y.; Zhao, Z. J.; Botton, G. A.; Sun, X. L. Pt/Pd Single-Atom Alloys as Highly Active Electrochemical Catalysts and the Origin of Enhanced Activity. *ACS Catal.* **2019**, *9*, 9350−9358.
(50) Chao, T. T.; Luo, X.; Chen, W. X.; Jiang, B.; Ge, J. J.; Lin, Y.; Wu, G.; Wang, X. Q.; Hu, Y. M.; Zhuang, Z. B.; Wu, Y. E.; Hong, X.; Li, Y. D. Atomically Dispersed Copper-Platinum Dual Sites Alloyed with Palladium Nanorings Catalyze the Hydrogen Evolution Reaction. *Angew. Chem., Int. Ed.* **2017**, *56*, 16047−16051.
(51) Gao, J. J.; Du, P.; Zhang, Q. H.; Shen, X.; Chiang, F. K.; Wen, Y. R.; Lin, X.; Liu, X. J.; Qiu, H. J. Platinum Single Atoms/Clusters Stabilized in Transition Metal Oxides for Enhanced Electrocatalysis. *Electrochim. Acta* **2019**, *297*, 155−162.
(52) Guan, Y. X.; Feng, Y. Y.; Wan, J.; Yang, X. H.; Fang, L.; Gu, X.; Liu, R. R.; Huang, Z. Y.; Li, J.; Luo, J.; Li, C. M.; Wang, Y. Ganoderma-Like MoS_2/NiS_2 with Single Platinum Atoms Doping as an Efficient and Stable Hydrogen Evolution Reaction Catalyst. *Small* **2018**, *14*, 1800697.
(53) Feng, Y. Y.; Guan, Y. X.; Zhang, H. J.; Huang, Z. Y.; Li, J.; Jiang, Z. Q.; Gu, X.; Wang, Y. Selectively Anchoring Pt Single Atoms at Hetero-Interfaces of Gamma-Al_2O_3/NiS to Promote the Hydrogen Evolution Reaction. *J. Mater. Chem. A* **2018**, *6*, 11783−11789.
(54) Jiang, K.; Liu, B. Y.; Luo, M.; Ning, S. C.; Peng, M.; Zhao, Y.; Lu, Y. R.; Chan, T. S.; de Groot, F. M. F.; Tan, Y. W. Single Platinum Atoms Embedded in Nanoporous Cobalt Selenide as Electrocatalyst for Accelerating Hydrogen Evolution Reaction. *Nat. Commun.* **2019**, *10*, 1743.
(55) Zhang, L. H.; Han, L. L.; Liu, H. X.; Liu, X. J.; Luo, J. Potential-Cycling Synthesis of Single Platinum Atoms for Efficient Hydrogen Evolution in Neutral Media. *Angew. Chem., Int. Ed.* **2017**, *56*, 13694−13698.
(56) Liu, J.; Jiao, M. G.; Lu, L. L.; Barkholtz, H. M.; Li, Y. P.; Wang, Y.; Jiang, L. H.; Wu, Z. J.; Liu, D. J.; Zhuang, L.; Ma, C.; Zeng, J.; Zhang, B. S.; Su, D. S.; Song, P.; Xing, W.; Xu, W. L.; Wang, Y.; Jiang, Z.; Sun, G. Q. High Performance Platinum Single Atom Electrocatalyst for Oxygen Reduction Reaction. *Nat. Commun.* **2017**, *8*, 15938.
(57) Choi, C. H.; Kim, M.; Kwon, H. C.; Cho, S. J.; Yun, S.; Kim, H. T.; Mayrhofer, K. J. J.; Kim, H.; Choi, M. Tuning Selectivity of Electrochemical Reactions by Atomically Dispersed Platinum Catalyst. *Nat. Commun.* **2016**, *7*, 10922.
(58) Song, X. Z.; Li, N.; Zhang, H.; Wang, H.; Wang, L. Y.; Bian, Z. Y. Promotion of Hydrogen Peroxide Production on Graphene-Supported Atomically Dispersed Platinum: Effects of Size on Oxygen Reduction Reaction Pathway. *J. Power Sources* **2019**, *435*, 226771.
(59) Liu, J.; Jiao, M. G.; Mei, B. B.; Tong, Y. X.; Li, Y. P.; Ruan, M. B.; Song, P.; Sun, G. Q.; Jiang, L. H.; Wang, Y.; Jiang, Z.; Gu, L.; Zhou, Z.; Xu, W. L. Carbon-Supported Divacancy-Anchored Platinum Single-Atom Electrocatalysts with Superhigh Pt Utilization for the Oxygen Reduction Reaction. *Angew. Chem., Int. Ed.* **2019**, *58*, 1163−1167.
(60) Lai, W. H.; Zhang, B. W.; Hu, Z. P.; Qu, X. M.; Jiang, Y. X.; Wang, Y. X.; Wang, J. Z.; Liu, H. K.; Chou, S. L. The Quasi-Pt-Allotrope Catalyst: Hollow PtCo@Single-Atom Pt-1 on Nitrogen-Doped Carbon toward Superior Oxygen Reduction. *Adv. Funct. Mater.* **2019**, *29*, 1807340.
(61) Yang, S.; Kim, J.; Tak, Y. J.; Soon, A.; Lee, H. Single-Atom Catalyst of Platinum Supported on Titanium Nitride for Selective Electrochemical Reactions. *Angew. Chem., Int. Ed.* **2016**, *55*, 2058−2062.
(62) Yang, S.; Tak, Y. J.; Kim, J.; Soon, A.; Lee, H. Support Effects in Single-Atom Platinum Catalysts for Electrochemical Oxygen Reduction. *ACS Catal.* **2017**, *7*, 1301−1307.
(63) Kim, J.; Roh, C. W.; Sahoo, S. K.; Yang, S.; Bae, J.; Han, J. W.; Lee, H. Highly Durable Platinum Single-Atom Alloy Catalyst for Electrochemical Reactions. *Adv. Energy Mater.* **2018**, *8*, 1701476.
(64) Yang, S.; Lee, H. Atomically Dispersed Platinum on Gold Nano-Octahedra with High Catalytic Activity on Formic Acid Oxidation. *ACS Catal.* **2013**, *3*, 437−443.
(65) Mahmood, J.; Li, F.; Jung, S. M.; Okyay, M. S.; Ahmad, I.; Kim, S. J.; Park, N.; Jeong, H. Y.; Baek, J. B. An Efficient and Ph-Universal Ruthenium-Based Catalyst for the Hydrogen Evolution Reaction. *Nat. Nanotechnol.* **2017**, *12*, 441−446.
(66) Zheng, Y.; Jiao, Y.; Zhu, Y. H.; Li, L. H.; Han, Y.; Chen, Y.; Jaroniec, M.; Qiao, S. Z. High Electrocatalytic Hydrogen Evolution Activity of an Anomalous Ruthenium Catalyst. *J. Am. Chem. Soc.* **2016**, *138*, 16174−16181.
(67) Peng, Y.; Lu, B. Z.; Chen, L. M.; Wang, N.; Lu, J. E.; Ping, Y.; Chen, S. W. Hydrogen Evolution Reaction Catalyzed by Ruthenium Ion-Complexed Graphitic Carbon Nitride Nanosheets. *J. Mater. Chem. A* **2017**, *5*, 18261−18269.
(68) Zhang, J.; Liu, P.; Wang, G.; Zhang, P. P.; Zhuang, X. D.; Chen, M. W.; Weidinger, I. M.; Feng, X. L. Ruthenium/Nitrogen-Doped Carbon as an Electrocatalyst for Efficient Hydrogen Evolution in Alkaline Solution. *J. Mater. Chem. A* **2017**, *5*, 25314−25318.
(69) Lu, B. Z.; Guo, L.; Wu, F.; Peng, Y.; Lu, J. E.; Smart, T. J.; Wang, N.; Finfrock, Y. Z.; Morris, D.; Zhang, P.; Li, N.; Gao, P.; Ping, Y.; Chen, S. W. Ruthenium Atomically Dispersed in Carbon Outperforms Platinum toward Hydrogen Evolution in Alkaline Media. *Nat. Commun.* **2019**, *10*, 631.
(70) Yang, J.; Chen, B. X.; Liu, X. K.; Liu, W.; Li, Z. J.; Dong, J. C.; Chen, W. X.; Yan, W. S.; Yao, T.; Duan, X. Z.; Wu, Y.; Li, Y. D. Efficient and Robust Hydrogen Evolution: Phosphorus Nitride Imide Nanotubes as Supports for Anchoring Single Ruthenium Sites. *Angew. Chem., Int. Ed.* **2018**, *57*, 9495−9500.
(71) Ramalingam, V.; Varadhan, P.; Fu, H. C.; Kim, H.; Zhang, D. L.; Chen, S. M.; Song, L.; Ma, D.; Wang, Y.; Alshareef, H. N.; He, J. H. Heteroatom-Mediated Interactions between Ruthenium Single Atoms and an Mxene Support for Efficient Hydrogen Evolution. *Adv. Mater.* **2019**, *31*, 1903841.
(72) Zhang, J. M.; Xu, X. P.; Yang, L.; Cheng, D. J.; Cao, D. P. Single-Atom Ru Doping Induced Phase Transition of MoS_2 and S Vacancy for Hydrogen Evolution Reaction. *Small Methods* **2019**, *3*, 1900653.
(73) Li, P. S.; Wang, M. Y.; Duan, X. X.; Zheng, L. R.; Cheng, X. P.; Zhang, Y. F.; Kuang, Y.; Li, Y. P.; Ma, Q.; Feng, Z. X.; Liu, W.; Sun, X.

https://dx.doi.org/10.1021/acscatal.0c01950
ACS Catal. 2020, 10, 7584−7618

M. Boosting Oxygen Evolution of Single-Atomic Ruthenium through Electronic Coupling with Cobalt-Iron Layered Double Hydroxides. *Nat. Commun.* **2019**, *10*, 1711.
(74) Cao, L. L.; Luo, Q. Q.; Chen, J. J.; Wang, L.; Lin, Y.; Wang, H. J.; Liu, X. K.; Shen, X. Y.; Zhang, W.; Liu, W.; Qi, Z. M.; Jiang, Z.; Yang, J. L.; Yao, T. Dynamic Oxygen Adsorption on Single-Atomic Ruthenium Catalyst with High Performance for Acidic Oxygen Evolution Reaction. *Nat. Commun.* **2019**, *10*, 4849.
(75) Yao, Y. C.; Hu, S. L.; Chen, W. X.; Huang, Z. Q.; Wei, W. C.; Yao, T.; Liu, R. R.; Zang, K. T.; Wang, X. Q.; Wu, G.; Yuan, W. J.; Yuan, T. W.; Zhu, B. Q.; Liu, W.; Li, Z. J.; He, D. S.; Xue, Z. G.; Wang, Y.; Zheng, X. S.; Dong, J. C.; Chang, C. R.; Chen, Y. X.; Hong, X.; Luo, J.; Wei, S. Q.; Li, W. X.; Strasser, P.; Wu, Y. E.; Li, Y. D. Engineering the Electronic Structure of Single Atom Ru Sites Via Compressive Strain Boosts Acidic Water Oxidation Electrocatalysis. *Nat. Catal.* **2019**, *2*, 304−313.
(76) Geng, Z. G.; Liu, Y.; Kong, X. D.; Li, P.; Li, K.; Liu, Z. Y.; Du, J. J.; Shu, M.; Si, R.; Zeng, J. Achieving a Record-High Yield Rate of 120.9 $7g_{NH3}$ mg_{Cat}^{-1}. h^{-1} for N_2 Electrochemical Reduction over Ru Single-Atom Catalysts. *Adv. Mater.* **2018**, *30*, 1870301.
(77) Tao, H. C.; Choi, C.; Ding, L. X.; Jiang, Z.; Han, Z. S.; Jia, M. W.; Fan, Q.; Gao, Y. N.; Wang, H. H.; Robertson, A. W.; Hong, S.; Jung, Y. S.; Liu, S. Z.; Sun, Z. Y. Nitrogen Fixation by Ru Single-Atom Electrocatalytic Reduction. *Chem.* **2019**, *5*, 204−214.
(78) Wang, Z. L.; Xu, S. M.; Xu, Y. Q.; Tan, L.; Wang, X.; Zhao, Y. F.; Duan, H. H.; Song, Y. F. Single Ru Atoms with Precise Coordination on a Monolayer Layered Double Hydroxide for Efficient Electrooxidation Catalysis. *Chem. Sci.* **2019**, *10*, 378−384.
(79) Zhang, C. H.; Sha, J. W.; Fei, H. L.; Liu, M. J.; Yazdi, S.; Zhang, J. B.; Zhong, Q. F.; Zou, X. L.; Zhao, N. Q.; Yu, H. S.; Jiang, Z.; Ringe, E.; Yakobson, B. I.; Dong, J. C.; Chen, D. L.; Tour, J. M. Single-Atomic Ruthenium Catalytic Sites on Nitrogen-Doped Graphene for Oxygen Reduction Reaction in Acidic Medium. *ACS Nano* **2017**, *11*, 6930−6941.
(80) Zhang, Y. K.; Wu, C. Q.; Jiang, H. L.; Lin, Y. X.; Liu, H. J.; He, Q.; Chen, S. M.; Duan, T.; Song, L. Atomic Iridium Incorporated in Cobalt Hydroxide for Efficient Oxygen Evolution Catalysis in Neutral Electrolyte. *Adv. Mater.* **2018**, *30*, 1707522.
(81) Xiao, M. L.; Zhu, J. B.; Li, G. R.; Li, N.; Li, S.; Cano, Z. P.; Ma, L.; Cui, P. X.; Xu, P.; Jiang, G. P.; Jin, H. L.; Wang, S.; Wu, T. P.; Lu, J.; Yu, A. P.; Su, D.; Chen, Z. W. A Single-Atom Iridium Heterogeneous Catalyst in Oxygen Reduction Reaction. *Angew. Chem., Int. Ed.* **2019**, *58*, 9640−9645.
(82) Zhang, J. F.; Liu, J. Y.; Xi, L. F.; Yu, Y. F.; Chen, N.; Sun, S. H.; Wang, W. C.; Lange, K. M.; Zhang, B. Single-Atom Au/NiFe Layered Double Hydroxide Electrocatalyst: Probing the Origin of Activity for Oxygen Evolution Reaction. *J. Am. Chem. Soc.* **2018**, *140*, 3876−3879.
(83) Youk, S.; Hwang, J.; Lee, S.; Kim, M. S.; Lee, J. Controlled Leaching Derived Synthesis of Atomically Dispersed/Clustered Gold on Mesoporous Cobalt Oxide for Enhanced Oxygen Evolution Reaction Activity. *Small Methods* **2019**, *3*, 1800293.
(84) Cai, C.; Han, S. B.; Wang, Q.; Gu, M. Direct Observation of Yolk-Shell Transforming to Gold Single Atoms and Clusters with Superior Oxygen Evolution Reaction Efficiency. *ACS Nano* **2019**, *13*, 8865−8871.
(85) Zhao, X.; Gao, P. F.; Yan, Y.; Li, X. Q.; Xing, Y. L.; Li, H. L.; Peng, Z. M.; Yang, J. L.; Zeng, J. Gold Atom-Decorated Cose2 Nanobelts with Engineered Active Sites for Enhanced Oxygen Evolution. *J. Mater. Chem. A* **2017**, *5*, 20202−20207.
(86) Chen, C. H.; Wu, D. Y.; Li, Z.; Zhang, R.; Kuai, C. G.; Zhao, X. R.; Dong, C. K.; Qiao, S. Z.; Liu, H.; Du, X. W. Ruthenium-Based Single-Atom Alloy with High Electrocatalytic Activity for Hydrogen Evolution. *Adv. Energy Mater.* **2019**, *9*, 1803913.
(87) Wang, X. Q.; Wang, W. Y.; Qiao, M.; Wu, G.; Chen, W. X.; Yuan, T. W.; Xu, Q.; Chen, M.; Zhang, Y.; Wang, X.; Wang, J.; Ge, J. J.; Hong, X.; Li, Y. F.; Wu, Y.; Li, Y. D. Atomically Dispersed Au-1 Catalyst Towards Efficient Electrochemical Synthesis of Ammonia. *Sci. Bull.* **2018**, *63*, 1246−1253.
(88) Xiang, W. K.; Zhao, Y. H.; Jiang, Z.; Li, X. P.; Zhang, H.; Sun, Y.; Ning, Z. J.; Du, F. P.; Gao, P.; Qian, J.; Kato, K.; Yamauchi, M.; Sun, Y. H. Palladium Single Atoms Supported by Interwoven Carbon Nanotube and Manganese Oxide Nanowire Networks for Enhanced Electrocatalysis. *J. Mater. Chem. A* **2018**, *6*, 23366−23377.
(89) Li, J.; Cheng, Y.; Zhang, J. N.; Fu, J. W.; Yan, W. F.; Xu, Q. Confining Pd Nanoparticles and Atomically Dispersed Pd into Defective MoO_3 Nanosheet for Enhancing Electro- and Photocatalytic Hydrogen Evolution Performances. *ACS Appl. Mater. Interfaces* **2019**, *11*, 27798−27804.
(90) Kim, H. E.; Lee, I. H.; Cho, J.; Shin, S.; Ham, H. C.; Kim, J. Y.; Lee, H. Palladium Single-Atom Catalysts Supported on $C@C_3N_4$ for Electrochemical Reactions. *ChemElectroChem* **2019**, *6*, 4757−4764.
(91) Xiong, Y.; Dong, J. C.; Huang, Z. Q.; Xin, P. Y.; Chen, W. X.; Wang, Y.; Li, Z.; Jin, Z.; Xing, W.; Zhuang, Z. B.; Ye, J. Y.; Wei, X.; Cao, R.; Gu, L.; Sun, S. G.; Zhuang, L.; Chen, X. Q.; Yang, H.; Chen, C.; Peng, Q.; Chang, C. R.; Wang, D. S.; Li, Y. D. Single-Atom Rh/N-Doped Carbon Electrocatalyst for Formic Acid Oxidation. *Nat. Nanotechnol.* **2020**, *15*, 390−397.
(92) Jiang, K.; Back, S.; Akey, A. J.; Xia, C.; Hu, Y. F.; Liang, W. T.; Schaak, D.; Stavitski, E.; Norskov, J. K.; Siahrostami, S.; Wang, H. T. Highly Selective Oxygen Reduction to Hydrogen Peroxide on Transition Metal Single Atom Coordination. *Nat. Commun.* **2019**, *10*, 3997.
(93) Sahraie, N. R.; Kramm, U. I.; Steinberg, J.; Zhang, Y. J.; Thomas, A.; Reier, T.; Paraknowitsch, J. P.; Strasser, P. Quantifying the Density and Utilization of Active Sites in Non-Precious Metal Oxygen Electroreduction Catalysts. *Nat. Commun.* **2015**, *6*, 8618.
(94) Mun, Y.; Lee, S.; Kim, K.; Kim, S.; Lee, S.; Han, J. W.; Lee, J. Versatile Strategy for Tuning ORR Activity of a Single Fe-N-4 Site by Controlling Electron-Withdrawing/Donating Properties of a Carbon Plane. *J. Am. Chem. Soc.* **2019**, *141*, 6254−6262.
(95) Qi, K.; Cui, X. Q.; Gu, L.; Yu, S. S.; Fan, X. F.; Luo, M. C.; Xu, S.; Li, N. B.; Zheng, L. R.; Zhang, Q. H.; Ma, J. Y.; Gong, Y.; Lv, F.; Wang, K.; Huang, H. H.; Zhang, W.; Guo, S. J.; Zheng, W. T.; Liu, P. Single-Atom Cobalt Array Bound to Distorted 1T MoS_2 with Ensemble Effect for Hydrogen Evolution Catalysis. *Nat. Commun.* **2019**, *10*, 5231.
(96) Sa, Y. J.; Park, S. O.; Jung, G. Y.; Shin, T. J.; Jeong, H. Y.; Kwak, S. K.; Joo, S. H. Heterogeneous Co-N/C Electrocatalysts with Controlled Cobalt Site Densities for the Hydrogen Evolution Reaction: Structure-Activity Correlations and Kinetic Insights. *ACS Catal.* **2019**, *9*, 83−97.
(97) Zhang, H. B.; Yu, L.; Chen, T.; Zhou, W.; Lou, X. W. Surface Modulation of Hierarchical MoS_2 Nanosheets by Ni Single Atoms for Enhanced Electrocatalytic Hydrogen Evolution. *Adv. Funct. Mater.* **2018**, *28*, 1807086.
(98) Vasudevan, P.; Santosh; Mann, N.; Tyagi, S. Transition-Metal Complexes of Porphyrins and Phthalocyanines as Electrocatalysts for Dioxygen Reduction. *Transition Met. Chem.* **1990**, *15*, 81−90.
(99) Ponce, I.; Silva, J. F.; Onate, R.; Rezende, M. C.; Paez, M. A.; Zagal, J. H.; Pavez, J.; Mendizabal, F.; Miranda-Rojas, S.; Munoz-Castro, A.; Arratia-Perez, R. Enhancement of the Catalytic Activity of Fe Phthalocyanine for the Reduction of O-2 Anchored to Au(111) Via Conjugated Self-Assembled Mono Layers of Aromatic Thiols as Compared to Cu Phthalocyanine. *J. Phys. Chem. C* **2012**, *116*, 15329−15341.
(100) Bezerra, C. W. B.; Zhang, L.; Lee, K. C.; Liu, H. S.; Marques, A. L. B.; Marques, E. P.; Wang, H. J.; Zhang, J. J. A Review of Fe-N/C and Co-N/C Catalysts for the Oxygen Reduction Reaction. *Electrochim. Acta* **2008**, *53*, 4937−4951.
(101) Chen, R. R.; Li, H. X.; Chu, D.; Wang, G. F. Unraveling Oxygen Reduction Reaction Mechanisms on Carbon-Supported Fe-Phthalocyanine and Co-Phthalocyanine Catalysts in Alkaline Solutions. *J. Phys. Chem. C* **2009**, *113*, 20689−20697.
(102) Bae, I. T.; Tryk, D. A.; Scherson, D. A. Effect of Heat Treatment on the Redox Properties of Iron Porphyrins Adsorbed on High Area Carbon in Acid Electrolytes: An in Situ Fe K-Edge X-Ray

https://dx.doi.org/10.1021/acscatal.0c01950
ACS Catal. 2020, 10, 7584−7618

Absorption near-Edge Structure Study. *J. Phys. Chem. B* **1998**, *102*, 4114−4117.
(103) Lefevre, M.; Dodelet, J. P.; Bertrand, P. Molecular Oxygen Reduction in Pem Fuel Cells: Evidence for the Simultaneous Presence of Two Active Sites in Fe-Based Catalysts. *J. Phys. Chem. B* **2002**, *106*, 8705−8713.
(104) Bouwkamp-Wijnoltz, A. L.; Visscher, W.; van Veen, J. A. R.; Boellaard, E.; van der Kraan, A. M.; Tang, S. C. On Active-Site Heterogeneity in Pyrolyzed Carbon-Supported Iron Porphyrin Catalysts for the Electrochemical Reduction of Oxygen: An in Situ Mossbauer Study. *J. Phys. Chem. B* **2002**, *106*, 12993−13001.
(105) Lee, D. H.; Lee, W. J.; Lee, W. J.; Kim, S. O.; Kim, Y. H. Theory, Synthesis, and Oxygen Reduction Catalysis of Fe-Porphyrin-Like Carbon Nanotube. *Phys. Rev. Lett.* **2011**, *106*, 175502.
(106) Yang, L.; Cheng, D.; Xu, H.; Zeng, X.; Wan, X.; Shui, J.; Xiang, Z.; Cao, D. Unveiling the High-Activity Origin of Single-Atom Iron Catalysts for Oxygen Reduction Reaction. *Proc. Natl. Acad. Sci. U. S. A.* **2018**, *115*, 6626−6631.
(107) Zhu, Y. S.; Zhang, B. S.; Liu, X.; Wang, D. W.; Su, D. S. Unravelling the Structure of Electrocatalytically Active Fe-N Complexes in Carbon for the Oxygen Reduction Reaction. *Angew. Chem., Int. Ed.* **2014**, *53*, 10673−10677.
(108) Wang, Q.; Zhou, Z. Y.; Lai, Y. J.; You, Y.; Liu, J. G.; Wu, X. L.; Terefe, E.; Chen, C.; Song, L.; Rauf, M.; Tian, N.; Sun, S. G. Phenylenediamine-Based FeN_x/C Catalyst with High Activity for Oxygen Reduction in Acid Medium and Its Active-Site Probing. *J. Am. Chem. Soc.* **2014**, *136*, 10882−10885.
(109) Niu, W. H.; Li, L. G.; Liu, X. J.; Wang, N.; Liu, J.; Zhou, W. J.; Tang, Z. H.; Chen, S. W. Mesoporous N-Doped Carbons Prepared with Thermally Removable Nanoparticle Templates: An Efficient Electrocatalyst for Oxygen Reduction Reaction. *J. Am. Chem. Soc.* **2015**, *137*, 5555−5562.
(110) Jiang, W. J.; Gu, L.; Li, L.; Zhang, Y.; Zhang, X.; Zhang, L. J.; Wang, J. Q.; Hu, J. S.; Wei, Z. D.; Wan, L. J. Understanding the High Activity of Fe-N-C Electrocatalysts in Oxygen Reduction: Fe/Fe_3C Nanoparticles Boost the Activity of Fe-N-X. *J. Am. Chem. Soc.* **2016**, *138*, 3570−3578.
(111) Fu, X. G.; Li, N.; Ren, B. H.; Jiang, G. P.; Liu, Y. R.; Hassan, F. M.; Su, D.; Zhu, J. B.; Yang, L.; Bai, Z. Y.; Cano, Z. P.; Yu, A. P.; Chen, Z. W. Tailoring FeN_4 Sites with Edge Enrichment for Boosted Oxygen Reduction Performance in Proton Exchange Membrane Fuel Cell. *Adv. Energy Mater.* **2019**, *9*, 1803737.
(112) Thorum, M. S.; Hankett, J. M.; Gewirth, A. A. Poisoning the Oxygen Reduction Reaction on Carbon-Supported Fe and Cu Electrocatalysts: Evidence for Metal-Centered Activity. *J. Phys. Chem. Lett.* **2011**, *2*, 295−298.
(113) Li, Y. C.; Liu, X. F.; Zheng, L. R.; Shang, J. X.; Wan, X.; Hu, R. M.; Guo, X.; Hong, S.; Shui, J. L. Preparation of Fe-N-C Catalysts with FeN_x (X = 1, 3, 4) Active Sites and Comparison of Their Activities for the Oxygen Reduction Reaction and Performances in Proton Exchange Membrane Fuel Cells. *J. Mater. Chem. A* **2019**, *7*, 26147−26153.
(114) Lai, Q. X.; Zheng, L. R.; Liang, Y. Y.; He, J. P.; Zhao, J. X.; Chen, J. H. Meta-Organic-Framework-Derived Fe-N/C Electrocatalyst with Five-Coordinated Fe-N-X), Sites for Advanced Oxygen Reduction in Acid Media. *ACS Catal.* **2017**, *7*, 1655−1663.
(115) Zhao, Y. M.; Zhang, P. C.; Xu, C.; Zhou, X. Y.; Liao, L. M.; Wei, P. J.; Liu, E.; Chen, H. Q.; He, Q. G.; Liu, J. G. Design and Preparation of Fe-N-5 Catalytic Sites in Single-Atom Catalysts for Enhancing the Oxygen Reduction Reaction in Fuel Cells. *ACS Appl. Mater. Interfaces* **2020**, *12*, 17334−17342.
(116) Huang, J. S.; Lu, Q. Q.; Ma, X.; Yang, X. R. Bio-Inspired FeN_5 Moieties Anchored on a Three-Dimensional Graphene Aerogel to Improve Oxygen Reduction Catalytic Performance. *J. Mater. Chem. A* **2018**, *6*, 18488−18497.
(117) Zheng, Y.; Yang, D. S.; Kweun, J. M.; Li, C.; Tan, K.; Kong, F. T.; Liang, C. P.; Chabal, Y. J.; Kim, Y. Y.; Cho, M.; Yu, J. S.; Cho, K. Rational Design of Common Transition Metal-Nitrogen-Carbon Catalysts for Oxygen Reduction Reaction in Fuel Cells. *Nano Energy* **2016**, *30*, 443−449.
(118) Lin, Y. C.; Liu, P. Y.; Velasco, E.; Yao, G.; Tian, Z. Q.; Zhang, L. J.; Chen, L. Fabricating Single-Atom Catalysts from Chelating Metal in Open Frameworks. *Adv. Mater.* **2019**, *31*, 1808193.
(119) Shen, H. J.; Gracia-Espino, E.; Ma, J. Y.; Tang, H. D.; Mamat, X.; Wagberg, T.; Hu, G. Z.; Guo, S. J. Atomically FeN_2 Moieties Dispersed on Mesoporous Carbon: A New Atomic Catalyst for Efficient Oxygen Reduction Catalysis. *Nano Energy* **2017**, *35*, 9−16.
(120) Zhu, C. Z.; Shi, Q. R.; Xu, B. Z.; Fu, S. F.; Wan, G.; Yang, C.; Yao, S. Y.; Song, J. H.; Zhou, H.; Du, D.; Beckman, S. P.; Su, D.; Lin, Y. H. Hierarchically Porous M-N-C (M = Co and Fe) Single-Atom Electrocatalysts with Robust MN_x Active Moieties Enable Enhanced ORR Performance. *Adv. Energy Mater.* **2018**, *8*, 1801956.
(121) Zhang, N.; Zhou, T. P.; Chen, M. L.; Feng, H.; Yuan, R. L.; Zhong, C. A.; Yan, W. S.; Tian, Y. C.; Wu, X. J.; Chu, W. S.; Wu, C. Z.; Xie, Y. High-Purity Pyrrole-Type FeN_4 Sites as a Superior Oxygen Reduction Electrocatalyst. *Energy Environ. Sci.* **2020**, *13*, 111−118.
(122) Peng, P.; Shi, L.; Huo, F.; Zhang, S. J.; Mi, C. X.; Cheng, Y. H.; Xiang, Z. H. In Situ Charge Exfoliated Soluble Covalent Organic Framework Directly Used for Zn-Air Flow Battery. *ACS Nano* **2019**, *13*, 878−884.
(123) Peng, P.; Shi, L.; Huo, F.; Mi, C. X.; Wu, X. H.; Zhang, S. J.; Xiang, Z. H. A Pyrolysis-Free Path toward Superiorly Catalytic Nitrogen-Coordinated Single Atom. *Sci. Adv.* **2019**, *5*, No. eaaw2322.
(124) Liu, K. X.; Wu, G.; Wang, G. F. Role of Local Carbon Structure Surrounding FeN_4 Sites in Boosting the Catalytic Activity for Oxygen Reduction. *J. Phys. Chem. C* **2017**, *121*, 11319−11324.
(125) Jiang, R.; Li, L.; Sheng, T.; Hu, G. F.; Chen, Y. G.; Wang, L. Y. Edge-Site Engineering of Atomically Dispersed Fe-N-4 by Selective C-N Bond Cleavage for Enhanced Oxygen Reduction Reaction Activities. *J. Am. Chem. Soc.* **2018**, *140*, 11594−11598.
(126) Wang, X.; Jia, Y.; Mao, X.; Liu, D. B.; He, W. X.; Li, J.; Liu, J. G.; Yan, X. C.; Chen, J.; Song, L.; Du, A. J.; Yao, X. D. Edge-Rich Fe-N-4 Active Sites in Defective Carbon for Oxygen Reduction Catalysis. *Adv. Mater.* **2020**, *32*, 2000966.
(127) He, T.; Lu, B.; Chen, Y.; Wang, Y.; Zhang, Y.; Davenport, J. L.; Chen, A. P.; Pao, C.-W.; Liu, M.; Sun, Z.; Stram, A.; Mordaunt, A.; Velasco, J.; Ping, Y.; Zhang, Y.; Chen, S. Nanowrinkled Carbon Aerogels Embedded with FeN Sites as Effective Oxygen Electrodes for Rechargeable Zinc-Air Battery. *Research* **2019**, *2019*, 6813585.
(128) Shen, H. J.; Gracia-Espino, E.; Ma, J. Y.; Zang, K. T.; Luo, J.; Wang, L.; Gao, S. S.; Mamat, X.; Hu, G. Z.; Wagberg, T.; Guo, S. J. Synergistic Effects between Atomically Dispersed Fe-N-C and C-S-C for the Oxygen Reduction Reaction in Acidic Media. *Angew. Chem., Int. Ed.* **2017**, *56*, 13800−13804.
(129) Li, Q. H.; Chen, W. X.; Xiao, H.; Gong, Y.; Li, Z.; Zheng, L. R.; Zheng, X. S.; Yan, W. S.; Cheong, W. C.; Shen, R. A.; Fu, N. H.; Gu, L.; Zhuang, Z. B.; Chen, C.; Wang, D. S.; Peng, Q.; Li, J.; Li, Y. D. Fe Isolated Single Atoms on S, N Codoped Carbon by Copolymer Pyrolysis Strategy for Highly Efficient Oxygen Reduction Reaction. *Adv. Mater.* **2018**, *30*, 1800588.
(130) Zhang, J. T.; Zhang, M.; Zeng, Y.; Chen, J. S.; Qiu, L. X.; Zhou, H.; Sun, C. J.; Yu, Y.; Zhu, C. Z.; Zhu, Z. H. Single Fe Atom on Hierarchically Porous S, N-Codoped Nanocarbon Derived from Porphyra Enable Boosted Oxygen Catalysis for Rechargeable Zn-Air Batteries. *Small* **2019**, *15*, 1900307.
(131) Wu, K. L.; Chen, X.; Liu, S. J.; Pan, Y.; Cheong, W. C.; Zhu, W.; Cao, X.; Shen, R. A.; Chen, W. X.; Luo, J.; Yan, W. S.; Zheng, L. R.; Chen, Z.; Wang, D. S.; Peng, Q.; Chen, C.; Li, Y. D. Porphyrin-Like Fe-N-4 Sites with Sulfur Adjustment on Hierarchical Porous Carbon for Different Rate-Determining Steps in Oxygen Reduction Reaction. *Nano Res.* **2018**, *11*, 6260−6269.
(132) Yuan, K.; Lutzenkirchen-Hecht, D.; Li, L. B.; Shuai, L.; Li, Y. Z.; Cao, R.; Qiu, M.; Zhuang, X. D.; Leung, M. K. H.; Chen, Y. W.; Scherf, U. Boosting Oxygen Reduction of Single Iron Active Sites Via Geometric and Electronic Engineering: Nitrogen and Phosphorus Dual Coordination. *J. Am. Chem. Soc.* **2020**, *142*, 2404−2412.

https://dx.doi.org/10.1021/acscatal.0c01950
ACS Catal. 2020, 10, 7584−7618

(133) Zhang, C. H.; Yang, S. Z.; Wu, J. J.; Liu, M. J.; Yazdi, S.; Ren, M. Q.; Sha, J. W.; Zhong, J.; Nie, K. Q.; Jalilov, A. S.; Li, Z. Y.; Li, H. M.; Yakobson, B. I.; Wu, Q.; Ringe, E. L.; Xu, H.; Ajayan, P. M.; Tour, J. M. Electrochemical CO_2 Reduction with Atomic Iron-Dispersed on Nitrogen-Doped Graphene. *Adv. Energy Mater.* **2018**, *8*, 1703487.
(134) Varela, A. S.; Sahraie, N. R.; Steinberg, J.; Ju, W.; Oh, H. S.; Strasser, P. Metal-Doped Nitrogenated Carbon as an Efficient Catalyst for Direct CO_2 Electroreduction to CO and Hydrocarbons. *Angew. Chem., Int. Ed.* **2015**, *54*, 10758−10762.
(135) Leonard, N.; Ju, W.; Sinev, I.; Steinberg, J.; Luo, F.; Varela, A. S.; Roldan Cuenya, B.; Strasser, P. The Chemical Identity, State and Structure of Catalytically Active Centers During the Electrochemical CO_2 Reduction on Porous Fe-Nitrogen-Carbon (Fe-N-C) Materials. *Chem. Sci.* **2018**, *9*, 5064−5073.
(136) Cheng, Q. Q.; Mao, K.; Ma, L. S.; Yang, L. J.; Zou, L. L.; Zou, Z. Q.; Hu, Z.; Yang, H. Encapsulation of Iron Nitride by Fe-N-C Shell Enabling Highly Efficient Electroreduction of CO_2 to CO. *ACS Energy Lett.* **2018**, *3*, 1205−1211.
(137) Ye, Y. F.; Cai, F.; Li, H. B.; Wu, H. H.; Wang, G. X.; Li, Y. S.; Miao, S.; Xie, S. H.; Si, R.; Wang, J.; Bao, X. H. Surface Functionalization of ZIF-8 with Ammonium Ferric Citrate toward High Exposure of Fe-N Active Sites for Efficient Oxygen and Carbon Dioxide Electroreduction. *Nano Energy* **2017**, *38*, 281−289.
(138) Sheng, T.; Sun, S. G. Free Energy Landscape of Electrocatalytic CO_2 Reduction to CO on Aqueous FeN_4 Center Embedded Graphene Studied by Ab Initio Molecular Dynamics Simulations. *Chem. Phys. Lett.* **2017**, *688*, 37−42.
(139) Huan, T. N.; Ranjbar, N.; Rousse, G.; Sougrati, M.; Zitolo, A.; Mougel, V.; Jaouen, F.; Fontecave, M. Electrochemical Reduction of CO_2 Catalyzed by Fe-N-C Materials: A Structure-Selectivity Study. *ACS Catal.* **2017**, *7*, 1520−1525.
(140) Qin, X. P.; Zhu, S. Q.; Xiao, F.; Zhang, L. L.; Shao, M. H. Active Sites on Heterogeneous Single-Iron-Atom Electrocatalysts in CO_2 Reduction Reaction. *ACS Energy Lett.* **2019**, *4*, 1778−1783.
(141) Zhang, H. N.; Li, J.; Xi, S. B.; Du, Y. H.; Hai, X.; Wang, J. Y.; Xu, H. M.; Wu, G.; Zhang, J.; Lu, J.; Wang, J. Z. A Graphene-Supported Single-Atom FeN_5 Catalytic Site for Efficient Electrochemical CO_2 Reduction. *Angew. Chem., Int. Ed.* **2019**, *58*, 14871−14876.
(142) Yuasa, M.; Yamaguchi, A.; Itsuki, H.; Tanaka, K.; Yamamoto, M.; Oyaizu, K. Modifying Carbon Particles with Polypyrrole for Adsorption of Cobalt Ions as Electrocatatytic Site for Oxygen Reduction. *Chem. Mater.* **2005**, *17*, 4278−4281.
(143) Ziegelbauer, J. M.; Olson, T. S.; Pylypenko, S.; Alamgir, F.; Jaye, C.; Atanassov, P.; Mukerjee, S. Direct Spectroscopic Observation of the Structural Origin of Peroxide Generation from Co-Based Pyrolyzed Porphyrins for ORR Applications. *J. Phys. Chem. C* **2008**, *112*, 8839−8849.
(144) Zitolo, A.; Ranjbar-Sahraie, N.; Mineva, T.; Li, J. K.; Jia, Q. Y.; Stamatin, S.; Harrington, G. F.; Lyth, S. M.; Krtil, P.; Mukerjee, S.; Fonda, E.; Jaouen, F. Identification of Catalytic Sites in Cobalt-Nitrogen-Carbon Materials for the Oxygen Reduction Reaction. *Nat. Commun.* **2017**, *8*, 957.
(145) Kattel, S.; Atanassov, P.; Kiefer, B. Catalytic Activity of Co-N-X/C Electrocatalysts for Oxygen Reduction Reaction: A Density Functional Theory Study. *Phys. Chem. Chem. Phys.* **2013**, *15*, 148−153.
(146) Sun, X. X.; Li, K.; Yin, C.; Wang, Y.; Jiao, M. G.; He, F.; Bai, X. W.; Tang, H.; Wu, Z. J. Dual-Site Oxygen Reduction Reaction Mechanism on CoN_4 and CoN_2 Embedded Graphene: Theoretical Insights. *Carbon* **2016**, *108*, 541−550.
(147) Yin, P. Q.; Yao, T.; Wu, Y.; Zheng, L. R.; Lin, Y.; Liu, W.; Ju, H. X.; Zhu, J. F.; Hong, X.; Deng, Z. X.; Zhou, G.; Wei, S. Q.; Li, Y. D. Single Cobalt Atoms with Precise N-Coordination as Superior Oxygen Reduction Reaction Catalysts. *Angew. Chem., Int. Ed.* **2016**, *55*, 10800−10805.
(148) Amiinu, I. S.; Liu, X. B.; Pu, Z. H.; Li, W. Q.; Li, Q. D.; Zhang, J.; Tang, H. L.; Zhang, H. N.; Mu, S. C. From 3d ZIF Nanocrystals to Co-N-X/C Nanorod Array Electrocatalysts for ORR, OER, and Zn-Air Batteries. *Adv. Funct. Mater.* **2018**, *28*, 1704638.
(149) Cheng, Q. Q.; Yang, L. J.; Zou, L. L.; Zou, Z. Q.; Chen, C.; Hu, Z.; Yang, H. Single Cobalt Atom and N Codoped Carbon Nanofibers as Highly Durable Electrocatalyst for Oxygen Reduction Reaction. *ACS Catal.* **2017**, *7*, 6864−6871.
(150) Sun, X.; Li, K.; Yin, C.; Wang, Y.; He, F.; Tang, H.; Wu, Z. J. CoN_3 Embedded Graphene, a Potential Catalyst for the Oxygen Reduction Reaction from a Theoretical Perspective. *Phys. Chem. Chem. Phys.* **2017**, *19*, 17670−17676.
(151) Sun, X. P.; Sun, S. X.; Gu, S. Q.; Liang, Z. F.; Zhang, J. X.; Yang, Y. Q.; Deng, Z.; Wei, P.; Peng, J.; Xu, Y.; Fang, C.; Li, Q.; Han, J. T.; Jiang, Z.; Huang, Y. H. High-Performance Single Atom Bifunctional Oxygen Catalysts Derived from ZIF-67 Superstructures. *Nano Energy* **2019**, *61*, 245−250.
(152) Sun, T. T.; Zhao, S.; Chen, W. X.; Zhai, D.; Dong, J. C.; Wang, Y.; Zhang, S. L.; Han, A. J.; Gu, L.; Yu, R.; Wen, X. D.; Ren, H. L.; Xu, L. B.; Chen, C.; Peng, Q.; Wang, D. S.; Li, Y. D. Single-Atomic Cobalt Sites Embedded in Hierarchically Ordered Porous Nitrogen-Doped Carbon as a Superior Bifunctional Electrocatalyst. *Proc. Natl. Acad. Sci. U. S. A.* **2018**, *115*, 12692−12697.
(153) Han, Y. H.; Wang, Y. G.; Chen, W. X.; Xu, R. R.; Zheng, L. R.; Zhang, J.; Luo, J.; Shen, R. A.; Zhu, Y. Q.; Cheong, W. C.; Chen, C.; Peng, Q.; Wang, D. S.; Li, Y. D. Hollow N-Doped Carbon Spheres with Isolated Cobalt Single Atomic Sites: Superior Electrocatalysts for Oxygen Reduction. *J. Am. Chem. Soc.* **2017**, *139*, 17269−17272.
(154) Han, X. P.; Ling, X. F.; Wang, Y.; Ma, T. Y.; Zhong, C.; Hu, W. B.; Deng, Y. D. Generation of Nanoparticle, Atomic-Cluster, and Single-Atom Cobalt Catalysts from Zeolitic Imidazole Frameworks by Spatial Isolation and Their Use in Zinc-Air Batteries. *Angew. Chem., Int. Ed.* **2019**, *58*, 5359−5364.
(155) Wan, G.; Yu, P. F.; Chen, H. R.; Wen, J. G.; Sun, C. J.; Zhou, H.; Zhang, N.; Li, Q. R.; Zhao, W. P.; Xie, B.; Li, T.; Shi, J. L. Engineering Single-Atom Cobalt Catalysts toward Improved Electrocatalysis. *Small* **2018**, *14*, 1704319.
(156) He, Y. H.; Hwang, S.; Cullen, D. A.; Uddin, M. A.; Langhorst, L.; Li, B. Y.; Karakalos, S.; Kropf, A. J.; Wegener, E. C.; Sokolowski, J.; Chen, M. J.; Myers, D.; Su, D.; More, K. L.; Wang, G. F.; Litster, S.; Wu, G. Highly Active Atomically Dispersed CoN_4 Fuel Cell Cathode Catalysts Derived from Surfactant-Assisted MOFs: Carbon-Shell Confinement Strategy. *Energy Environ. Sci.* **2019**, *12*, 250−260.
(157) Zhang, J. Q.; Zhao, Y. F.; Chen, C.; Huang, Y. C.; Dong, C. L.; Chen, C. J.; Liu, R. S.; Wang, C. Y.; Yan, K.; Li, Y. D.; Wang, G. X. Tuning the Coordination Environment in Single-Atom Catalysts to Achieve Highly Efficient Oxygen Reduction Reactions. *J. Am. Chem. Soc.* **2019**, *141*, 20118−20126.
(158) Li, Y. Z.; Cao, R.; Li, L. B.; Tang, X. N.; Chu, T. L.; Huang, B. Y.; Yuan, K.; Chen, Y. W. Simultaneously Integrating Single Atomic Cobalt Sites and Co_9S_8 Nanoparticles into Hollow Carbon Nanotubes as Trifunctional Electrocatalysts for Zn-Air Batteries to Drive Water Splitting. *Small* **2020**, *16*, 1906735.
(159) Jung, E.; Shin, H.; Lee, B. H.; Efremov, V.; Lee, S.; Lee, H. S.; Kim, J.; Hooch Antink, W.; Park, S.; Lee, K. S.; Cho, S. P.; Yoo, J. S.; Sung, Y. E.; Hyeon, T. Atomic-Level Tuning of Co-N-C Catalyst for High-Performance Electrochemical H_2O_2 Production. *Nat. Mater.* **2020**, *19*, 436−442.
(160) Li, B. Q.; Zhao, C. X.; Liu, J. N.; Zhang, Q. Electrosynthesis of Hydrogen Peroxide Synergistically Catalyzed by Atomic Co-N-X-C Sites and Oxygen Functional Groups in Noble-Metal-Free Electrocatalysts. *Adv. Mater.* **2019**, *31*, 1808173.
(161) Zou, X. X.; Huang, X. X.; Goswami, A.; Silva, R.; Sathe, B. R.; Mikmekova, E.; Asefa, T. Cobalt-Embedded Nitrogen-Rich Carbon Nanotubes Efficiently Catalyze Hydrogen Evolution Reaction at All Ph Values. *Angew. Chem., Int. Ed.* **2014**, *53*, 4372−4376.
(162) Fei, H. L.; Dong, J. C.; Arellano-Jimenez, M. J.; Ye, G. L.; Kim, N. D.; Samuel, E. L. G.; Peng, Z. W.; Zhu, Z.; Qin, F.; Bao, J. M.; Yacaman, M. J.; Ajayan, P. M.; Chen, D. L.; Tour, J. M. Atomic Cobalt on Nitrogen-Doped Graphene for Hydrogen Generation. *Nat. Commun.* **2015**, *6*, 8668.

https://dx.doi.org/10.1021/acscatal.0c01950
ACS Catal. 2020, 10, 7584−7618

(163) Fei, H. L.; Dong, J. C.; Feng, Y. X.; Allen, C. S.; Wan, C. Z.; Volosskiy, B.; Li, M. F.; Zhao, Z. P.; Wang, Y. L.; Sun, H. T.; An, P. F.; Chen, W. X.; Guo, Z. Y.; Lee, C.; Chen, D. L.; Shakir, I.; Liu, M. J.; Hu, T. D.; Li, Y. D.; Kirkland, A. I.; Duan, X. F.; Huang, Y. General Synthesis and Definitive Structural Identification of MN_4C_4 Single-Atom Catalysts with Tunable Electrocatalytic Activities. *Nat. Catal.* **2018**, *1*, 63−72.
(164) Cao, L. L.; Luo, Q. Q.; Liu, W.; Lin, Y. K.; Liu, X. K.; Cao, Y. J.; Zhang, W.; Wu, Y.; Yang, J. L.; Yao, T.; Wei, S. Q. Identification of Single-Atom Active Sites in Carbon-Based Cobalt Catalysts During Electrocatalytic Hydrogen Evolution. *Nat. Catal.* **2019**, *2*, 134−141.
(165) Kuznetsov, D. A.; Chen, Z. X.; Kumar, P. V.; Tsoukalou, A.; Kierzkowska, A.; Abdala, P. M.; Safonova, O. V.; Fedorov, A.; Muller, C. R. Single Site Cobalt Substitution in 2d Molybdenum Carbide (Mxene) Enhances Catalytic Activity in the Hydrogen Evolution Reaction. *J. Am. Chem. Soc.* **2019**, *141*, 17809−17816.
(166) Zhang, Q. Q.; Duan, Z. Y.; Li, M.; Guan, J. Q. Atomic Cobalt Catalysts for the Oxygen Evolution Reaction. *Chem. Commun.* **2020**, *56*, 794−797.
(167) Dilpazir, S.; He, H. Y.; Li, Z. H.; Wang, M.; Lu, P. L.; Liu, R. J.; Xie, Z. J.; Gao, D. L.; Zhang, G. J. Cobalt Single Atoms Immobilized N-Doped Carbon Nanotubes for Enhanced Bifunctional Catalysis toward Oxygen Reduction and Oxygen Evolution Reactions. *ACS Appl. Energy Mater.* **2018**, *1*, 3283−3291.
(168) Dou, S.; Dong, C. L.; Hu, Z.; Huang, Y. C.; Chen, J. L.; Tao, L.; Yan, D. F.; Chen, D. W.; Shen, S. H.; Chou, S. L.; Wang, S. Y. Atomic-Scale Coox Species in Metal-Organic Frameworks for Oxygen Evolution Reaction. *Adv. Funct. Mater.* **2017**, *27*, 1702546.
(169) Wang, X. Q.; Chen, Z.; Zhao, X. Y.; Yao, T.; Chen, W. X.; You, R.; Zhao, C. M.; Wu, G.; Wang, J.; Huang, W. X.; Yang, J. L.; Hong, X.; Wei, S. Q.; Wu, Y.; Li, Y. D. Regulation of Coordination Number over Single Co Sites: Triggering the Efficient Electroreduction of CO_2. *Angew. Chem., Int. Ed.* **2018**, *57*, 1944−1948.
(170) Su, P. P.; Iwase, K.; Harada, T.; Kamiya, K.; Nakanishi, S. Covalent Triazine Framework Modified with Coordinatively-Unsaturated Co or Ni Atoms for CO_2 Electrochemical Reduction. *Chem. Sci.* **2018**, *9*, 3941−3947.
(171) Zhou, H. Q.; Zou, X. L.; Wu, X.; Yang, X.; Li, J. Coordination Engineering in Cobalt-Nitrogen-Functionalized Materials for CO_2 Reduction. *J. Phys. Chem. Lett.* **2019**, *10*, 6551−6557.
(172) Pan, Y.; Lin, R.; Chen, Y. J.; Liu, S. J.; Zhu, W.; Cao, X.; Chen, W. X.; Wu, K. L.; Cheong, W. C.; Wang, Y.; Zheng, L. R.; Luo, J.; Lin, Y.; Liu, Y. Q.; Liu, C. G.; Li, J.; Lu, Q.; Chen, X.; Wang, D. S.; Peng, Q.; Chen, C.; Li, Y. D. Design of Single-Atom Co-N-5 Catalytic Site: A Robust Electrocatalyst for CO_2 Reduction with Nearly 100% CO Selectivity and Remarkable Stability. *J. Am. Chem. Soc.* **2018**, *140*, 4218−4221.
(173) Zhang, L. Z.; Jia, Y.; Gao, G. P.; Yan, X. C.; Chen, N.; Chen, J.; Soo, M. T.; Wood, B.; Yang, D. J.; Du, A. J.; Yao, X. D. Graphene Defects Trap Atomic Ni Species for Hydrogen and Oxygen Evolution Reactions. *Chem.* **2018**, *4*, 285−297.
(174) Zhao, S. Y.; Cheng, Y.; Veder, J. P.; Johannessen, B.; Saunders, M.; Zhang, L. J.; Liu, C.; Chisholm, M. F.; De Marco, R.; Liu, J.; Yang, S. Z.; Jiang, S. P. One-Pot Pyrolysis Method to Fabricate Carbon Nanotube Supported Ni Single-Atom Catalysts with Ultrahigh Loading. *ACS Appl. Energy Mater.* **2018**, *1*, 5286−5297.
(175) Qiu, H. J.; Ito, Y.; Cong, W. T.; Tan, Y. W.; Liu, P.; Hirata, A.; Fujita, T.; Tang, Z.; Chen, M. W. Nanoporous Graphene with Single-Atom Nickel Dopants: An Efficient and Stable Catalyst for Electrochemical Hydrogen Production. *Angew. Chem., Int. Ed.* **2015**, *54*, 14031−14035.
(176) Tran, P. D.; Le Goff, A.; Heidkamp, J.; Jousselme, B.; Guillet, N.; Palacin, S.; Dau, H.; Fontecave, M.; Artero, V. Noncovalent Modification of Carbon Nanotubes with Pyrene-Functionalized Nickel Complexes: Carbon Monoxide Tolerant Catalysts for Hydrogen Evolution and Uptake. *Angew. Chem., Int. Ed.* **2011**, *50*, 1371−1374.
(177) Zhao, Y. Q.; Ling, T.; Chen, S. M.; Jin, B.; Vasileff, A.; Jiao, Y.; Song, L.; Luo, J.; Qiao, S. Z. Non-Metal Single-Iodine-Atom Electrocatalysts for the Hydrogen Evolution Reaction. *Angew. Chem., Int. Ed.* **2019**, *58*, 12252−12257.
(178) Ouyang, T.; Chen, A. N.; He, Z. Z.; Liu, Z. Q.; Tong, Y. X. Rational Design of Atomically Dispersed Nickel Active Sites in 1-Mo_2C for the Hydrogen Evolution Reaction at All pH Values. *Chem. Commun.* **2018**, *54*, 9901−9904.
(179) Wang, Q.; Zhao, Z. L.; Dong, S.; He, D. S.; Lawrence, M. J.; Han, S. B.; Cai, C.; Xiang, S. H.; Rodriguez, P.; Xiang, B.; Wang, Z. G.; Liang, Y. Y.; Gu, M. Design of Active Nickel Single-Atom Decorated MoS_2 as a pH-Universal Catalyst for Hydrogen Evolution Reaction. *Nano Energy* **2018**, *53*, 458−467.
(180) Fan, L. L.; Liu, P. F.; Yan, X. C.; Gu, L.; Yang, Z. Z.; Yang, H. G.; Qiu, S. L.; Yao, X. D. Atomically Isolated Nickel Species Anchored on Graphitized Carbon for Efficient Hydrogen Evolution Electrocatalysis. *Nat. Commun.* **2016**, *7*, 10667.
(181) Li, M. F.; Duanmu, K. N.; Wan, C. Z.; Cheng, T.; Zhang, L.; Dai, S.; Chen, W. X.; Zhao, Z. P.; Li, P.; Fei, H. L.; Zhu, Y. M.; Yu, R.; Luo, J.; Zang, K. T.; Lin, Z. Y.; Ding, M. N.; Huang, J.; Sun, H. T.; Guo, J. H.; Pan, X. Q.; Goddard, W. A.; Sautet, P.; Huang, Y.; Duan, X. F. Single-Atom Tailoring of Platinum Nanocatalysts for High-Performance Multifunctional Electrocatalysis. *Nat. Catal.* **2019**, *2*, 495−503.
(182) Xue, Y. R.; Huang, B. L.; Yi, Y. P.; Guo, Y.; Zuo, Z. C.; Li, Y. J.; Jia, Z. Y.; Liu, H. B.; Li, Y. L. Anchoring Zero Valence Single Atoms of Nickel and Iron on Graphdiyne for Hydrogen Evolution. *Nat. Commun.* **2018**, *9*, 1460.
(183) Subbaraman, R.; Tripkovic, D.; Strmcnik, D.; Chang, K. C.; Uchimura, M.; Paulikas, A. P.; Stamenkovic, V.; Markovic, N. M. Enhancing Hydrogen Evolution Activity in Water Splitting by Tailoring Li+-Ni(OH)(2)-Pt Interfaces. *Science* **2011**, *334*, 1256−1260.
(184) Lei, C. J.; Wang, Y.; Hou, Y.; Liu, P.; Yang, J.; Zhang, T.; Zhuang, X. D.; Chen, M. W.; Yang, B.; Lei, L. C.; Yuan, C.; Qiu, M.; Feng, X. L. Efficient Alkaline Hydrogen Evolution on Atomically Dispersed Ni-N_x Species Anchored Porous Carbon with Embedded Ni Nanoparticles by Accelerating Water Dissociation Kinetics. *Energy Environ. Sci.* **2019**, *12*, 149−156.
(185) Zhang, H. B.; Liu, Y. Y.; Chen, T.; Zhang, J. T.; Zhang, J.; Lou, X. W. Unveiling the Activity Origin of Electrocatalytic Oxygen Evolution over Isolated Ni Atoms Supported on a N-Doped Carbon Matrix. *Adv. Mater.* **2019**, *31*, 1904548.
(186) Hou, Y.; Qiu, M.; Kim, M. G.; Liu, P.; Nam, G. T.; Zhang, T.; Zhuang, X. D.; Yang, B.; Cho, J.; Chen, M. W.; Yuan, C.; Lei, L. C.; Feng, X. L. Atomically Dispersed Nickel-Nitrogen-Sulfur Species Anchored on Porous Carbon Nanosheets for Efficient Water Oxidation. *Nat. Commun.* **2019**, *10*, 1392.
(187) Li, Y. G.; Wu, Z. S.; Lu, P. F.; Wang, X.; Liu, W.; Liu, Z. B.; Ma, J. Y.; Ren, W. C.; Jiang, Z.; Bao, X. H. High-Valence Nickel Single-Atom Catalysts Coordinated to Oxygen Sites for Extraordinarily Activating Oxygen Evolution Reaction. *Adv. Sci.* **2020**, *7*, 1903089.
(188) Xu, Y. Q.; Zhang, W. F.; Li, Y. G.; Lu, P. F.; Wu, Z. S. A General Bimetal-Ion Adsorption Strategy to Prepare Nickel Single Atom Catalysts Anchored on Graphene for Efficient Oxygen Evolution Reaction. *J. Energy Chem.* **2020**, *43*, 52−57.
(189) Bi, W. T.; Li, X. G.; You, R.; Chen, M. L.; Yuan, R. L.; Huang, W. X.; Wu, X. J.; Chu, W. S.; Wu, C. Z.; Xie, Y. Surface Immobilization of Transition Metal Ions on Nitrogen-Doped Graphene Realizing High-Efficient and Selective CO_2 Reduction. *Adv. Mater.* **2018**, *30*, 1706617.
(190) Cheng, Y.; Zhao, S. Y.; Johannessen, B.; Veder, J. P.; Saunders, M.; Rowles, M. R.; Cheng, M.; Liu, C.; Chisholm, M. F.; De Marco, R.; Cheng, H. M.; Yang, S. Z.; Jiang, S. P. Atomically Dispersed Transition Metals on Carbon Nanotubes with Ultrahigh Loading for Selective Electrochemical Carbon Dioxide Reduction. *Adv. Mater.* **2018**, *30*, 1706287.
(191) Jeong, H. Y.; Balamurugan, M.; Choutipalli, V. S. K.; Jeong, E. S.; Subramanian, V.; Sim, U.; Nam, K. T. Achieving Highly Efficient CO_2 to Co Electroreduction Exceeding 300 mA cm^{-2} with Single-

https://dx.doi.org/10.1021/acscatal.0c01950
ACS Catal. 2020, 10, 7584−7618

Atom Nickel Electrocatalysts. *J. Mater. Chem. A* **2019**, *7*, 10651−10661.
(192) Jiang, K.; Siahrostami, S.; Zheng, T. T.; Hu, Y. F.; Hwang, S.; Stavitski, E.; Peng, Y. D.; Dynes, J.; Gangisetty, M.; Su, D.; Attenkofer, K.; Wang, H. T. Isolated Ni Single Atoms in Graphene Nanosheets for High-Performance CO_2 Reduction. *Energy Environ. Sci.* **2018**, *11*, 893−903.
(193) Ju, W.; Bagger, A.; Hao, G. P.; Varela, A. S.; Sinev, I.; Bon, V.; Roldan Cuenya, B.; Kaskel, S.; Rossmeisl, J.; Strasser, P. Understanding Activity and Selectivity of Metal-Nitrogen-Doped Carbon Catalysts for Electrochemical Reduction of CO_2. *Nat. Commun.* **2017**, *8*, 944.
(194) Li, X. G.; Bi, W. T.; Chen, M. L.; Sun, Y. X.; Ju, H. X.; Yan, W. S.; Zhu, J. F.; Wu, X. J.; Chu, W. S.; Wu, C. Z.; Xie, Y. Exclusive Ni-N-4 Sites Realize near-Unity CO Selectivity for Electrochemical CO_2 Reduction. *J. Am. Chem. Soc.* **2017**, *139*, 14889−14892.
(195) Lu, C. B.; Yang, J.; Wei, S.; Bi, S.; Xia, Y.; Chen, M. X.; Hou, Y.; Qiu, M.; Yuan, C.; Su, Y. Z.; Zhang, F.; Liang, H. W.; Zhuang, X. D. Atomic Ni Anchored Covalent Triazine Framework as High Efficient Electrocatalyst for Carbon Dioxide Conversion. *Adv. Funct. Mater.* **2019**, *29*, 1806884.
(196) Yan, C. C.; Li, H. B.; Ye, Y. F.; Wu, H. H.; Cai, F.; Si, R.; Xiao, J. P.; Miao, S.; Xie, S. H.; Yang, F.; Li, Y. S.; Wang, G. X.; Bao, X. H. Coordinatively Unsaturated Nickel-Nitrogen Sites Towards Selective and High-Rate CO_2 Electroreduction. *Energy Environ. Sci.* **2018**, *11*, 1204−1210.
(197) Yang, H. B.; Hung, S. F.; Liu, S.; Yuan, K. D.; Miao, S.; Zhang, L. P.; Huang, X.; Wang, H. Y.; Cai, W. Z.; Chen, R.; Gao, J. J.; Yang, X. F.; Chen, W.; Huang, Y. Q.; Chen, H. M.; Li, C. M.; Zhang, T.; Liu, B. Atomically Dispersed Ni(I) as the Active Site for Electrochemical CO_2 Reduction. *Nat. Energy* **2018**, *3*, 140−147.
(198) Zhao, C. M.; Dai, X. Y.; Yao, T.; Chen, W. X.; Wang, X. Q.; Wang, J.; Yang, J.; Wei, S. Q.; Wu, Y. E.; Li, Y. D. Ionic Exchange of Metal Organic Frameworks to Access Single Nickel Sites for Efficient Electroreduction of CO_2. *J. Am. Chem. Soc.* **2017**, *139*, 8078−8081.
(199) Zheng, T. T.; Jiang, K.; Ta, N.; Hu, Y. F.; Zeng, J.; Liu, J. Y.; Wang, H. T. Large-Scale and Highly Selective CO_2 Electrocatalytic Reduction on Nickel Single-Atom Catalyst. *Joule* **2019**, *3*, 265−278.
(200) Cheng, Y.; Zhao, S. Y.; Li, H. B.; He, S.; Veder, J. P.; Johannessen, B.; Xiao, J. P.; Lu, S. F.; Pan, J.; Chisholm, M. F.; Yang, S. Z.; Liu, C.; Chen, J. G.; Jiang, S. P. Unsaturated Edge-Anchored Ni Single Atoms on Porous Microwave Exfoliated Graphene Oxide for Electrochemical CO_2. *Appl. Catal., B* **2019**, *243*, 294−303.
(201) Proshlyakov, D. A.; Pressler, M. A.; Babcock, G. T. Dioxygen Activation and Bond Cleavage by Mixed-Valence Cytochrome C Oxidase. *Proc. Natl. Acad. Sci. U. S. A.* **1998**, *95*, 8020−8025.
(202) Collman, J. P.; Wagenknecht, P. S.; Hutchison, J. E. Molecular Catalysts for Multielectron Redox Reactions of Small Molecules - the Cofacial Metallodiporphyrin Approach. *Angew. Chem., Int. Ed. Engl.* **1994**, *33*, 1537−1554.
(203) Mirica, L. M.; Ottenwaelder, X.; Stack, T. D. P. Structure and Spectroscopy of Copper-Dioxygen Complexes. *Chem. Rev.* **2004**, *104*, 1013−1045.
(204) Solomon, E. I.; Heppner, D. E.; Johnston, E. M.; Ginsbach, J. W.; Cirera, J.; Qayyum, M.; Kieber-Emmons, M. T.; Kjaergaard, C. H.; Hadt, R. G.; Tian, L. Copper Active Sites in Biology. *Chem. Rev.* **2014**, *114*, 3659−3853.
(205) Mano, N.; Soukharev, V.; Heller, A. A Laccase-Wiring Redox Hydrogel for Efficient Catalysis of O_2 Electroreduction. *J. Phys. Chem. B* **2006**, *110*, 11180−11187.
(206) Collman, J. P.; Devaraj, N. K.; Decreau, R. A.; Yang, Y.; Yan, Y. L.; Ebina, W.; Eberspacher, T. A.; Chidsey, C. E. D. A Cytochrome C Oxidase Model Catalyzes Oxygen to Water Reduction under Rate-Limiting Electron Flux. *Science* **2007**, *315*, 1565−1568.
(207) Thorum, M. S.; Yadav, J.; Gewirth, A. A. Oxygen Reduction Activity of a Copper Complex of 3,5-Diamino-1,2,4-Triazole Supported on Carbon Black. *Angew. Chem., Int. Ed.* **2009**, *48*, 165−167.
(208) Thorseth, M. A.; Letko, C. S.; Tse, E. C. M.; Rauchfuss, T. B.; Gewirth, A. A. Ligand Effects on the Overpotential for Dioxygen Reduction by Tris(2-Pyridylmethyl)Amine Derivatives. *Inorg. Chem.* **2013**, *52*, 628−634.
(209) Dias, V. L. N.; Fernandes, E. N.; da Silva, L. M. S.; Marques, E. P.; Zhang, J. J.; Marques, A. L. B. Electrochemical Reduction of Oxygen and Hydrogen Peroxide Catalyzed by a Surface Copper(II)-2,4,6-Tris(2-Piridil)-1,3,5-Triazine Complex Adsorbed on a Graphite Electrode. *J. Power Sources* **2005**, *142*, 10−17.
(210) McCrory, C. C. L.; Ottenwaelder, X.; Stack, T. D. P.; Chidsey, C. E. D. Kinetic and Mechanistic Studies of the Electrocatalytic Reduction of O_2 to H_2O with Mononuclear Cu Complexes of Substituted 1,10-Phenanthrolines. *J. Phys. Chem. A* **2007**, *111*, 12641−12650.
(211) Thorseth, M. A.; Tornow, C. E.; Tse, E. C. M.; Gewirth, A. A. Cu Complexes That Catalyze the Oxygen Reduction Reaction. *Coord. Chem. Rev.* **2013**, *257*, 130−139.
(212) Iwase, K.; Yoshioka, T.; Nakanishi, S.; Hashimoto, K.; Kamiya, K. Copper-Modified Covalent Triazine Frameworks as Non-Noble-Metal Electrocatalysts for Oxygen Reduction. *Angew. Chem., Int. Ed.* **2015**, *54*, 11068−11072.
(213) Savy, M.; Andro, P.; Bernard, C.; Magner, G. Etude De La Reduction De L'oxygene Sur Les Phtalocyanines Monomeres Et Polymeres—I. Principes Fondamentaux, Choix De L'ion Central. *Electrochim. Acta* **1973**, *18*, 191−197.
(214) Monzani, E.; Battaini, G.; Perotti, A.; Casella, L.; Gullotti, M.; Santagostini, L.; Nardin, G.; Randaccio, L.; Geremia, S.; Zanello, P.; Opromolla, G. Mechanistic, Structural, and Spectroscopic Studies on the Catecholase Activity of a Dinuclear Copper Complex by Dioxygen. *Inorg. Chem.* **1999**, *38*, 5359−5369.
(215) Gentil, S.; Serre, D.; Philouze, C.; Holzinger, M.; Thomas, F.; Le Goff, A. Electrocatalytic O_2 Reduction at a Bio-Inspired Mononuclear Copper Phenolato Complex Immobilized on a Carbon Nanotube Electrode. *Angew. Chem., Int. Ed.* **2016**, *55*, 2517−2520.
(216) Xie, X.; Liu, J. J.; Li, T. F.; Song, Y.; Wang, F. Post-Formation Copper-Nitrogen Species on Carbon Black: Their Chemical Structures and Active Sites for Oxygen Reduction Reaction. *Chem. - Eur. J.* **2018**, *24*, 9968−9975.
(217) Wu, H. H.; Li, H. B.; Zhao, X. F.; Liu, Q. F.; Wang, J.; Xiao, J. P.; Xie, S. H.; Si, R.; Yang, F.; Miao, S.; Guo, X. G.; Wang, G. X.; Bao, X. H. Highly Doped and Exposed Cu(I)-N Active Sites within Graphene Towards Efficient Oxygen Reduction for Zinc-Air Batteries. *Energy Environ. Sci.* **2016**, *9*, 3736−3745.
(218) Li, F.; Han, G. F.; Noh, H. J.; Kim, S. J.; Lu, Y. L.; Jeong, H. Y.; Fu, Z. P.; Baek, J. B. Boosting Oxygen Reduction Catalysis with Abundant Copper Single Atom Active Sites. *Energy Environ. Sci.* **2018**, *11*, 2263−2269.
(219) Wang, D. H.; Ao, C. C.; Liu, X. K.; Fang, S.; Lin, Y.; Liu, W.; Zhang, W.; Zheng, X. S.; Zhang, L. D.; Yao, T. Coordination-Engineered Cu-N-X Single-Site Catalyst for Enhancing Oxygen Reduction Reaction. *ACS Appl. Energy Mater.* **2019**, *2*, 6497−6504.
(220) Qu, Y. T.; Li, Z. J.; Chen, W. X.; Lin, Y.; Yuan, T. W.; Yang, Z. K.; Zhao, C. M.; Wang, J.; Zhao, C.; Wang, X.; Zhou, F. Y.; Zhuang, Z. B.; Wu, Y.; Li, Y. D. Direct Transformation of Bulk Copper into Copper Single Sites Via Emitting and Trapping of Atoms. *Nat. Catal.* **2018**, *1*, 781−786.
(221) Yang, Z. K.; Chen, B. X.; Chen, W. X.; Qu, Y. T.; Zhou, F. Y.; Zhao, C. M.; Xu, Q.; Zhang, Q. H.; Duan, X. Z.; Wu, Y. Directly Transforming Copper (I) Oxide Bulk into Isolated Single-Atom Copper Sites Catalyst through Gas-Transport Approach. *Nat. Commun.* **2019**, *10*, 3734.
(222) Song, P.; Luo, M.; Liu, X. Z.; Xing, W.; Xu, W. L.; Jiang, Z.; Gu, L. Zn Single Atom Catalyst for Highly Efficient Oxygen Reduction Reaction. *Adv. Funct. Mater.* **2017**, *27*, 1700802.
(223) Li, J.; Chen, S. G.; Yang, N.; Deng, M. M.; Ibraheem, S.; Deng, J. H.; Li, J.; Li, L.; Wei, Z. D. Ultrahigh-Loading Zinc Single-Atom Catalyst for Highly Efficient Oxygen Reduction in Both Acidic and Alkaline Media. *Angew. Chem., Int. Ed.* **2019**, *58*, 7035−7039.

https://dx.doi.org/10.1021/acscatal.0c01950
ACS Catal. 2020, 10, 7584−7618

(224) Luo, E. G.; Zhang, H.; Wang, X.; Gao, L. Q.; Gong, L. Y.; Zhao, T.; Jin, Z.; Ge, J. J.; Jiang, Z.; Liu, C. P.; Xing, W. Single-Atom Cr-N-4 Sites Designed for Durable Oxygen Reduction Catalysis in Acid Media. *Angew. Chem., Int. Ed.* **2019**, *58*, 12469−12475.
(225) Tang, C.; Jiao, Y.; Shi, B. Y.; Liu, J. N.; Xie, Z. H.; Chen, X.; Zhang, Q.; Qiao, S. Z. Coordination Tunes Selectivity: Two-Electron Oxygen Reduction on High-Loading Molybdenum Single-Atom Catalysts. *Angew. Chem., Int. Ed.* **2020**, *59*, 9171.
(226) Guan, J. Q.; Duan, Z. Y.; Zhang, F. X.; Kelly, S. D.; Si, R.; Dupuis, M.; Huang, Q. G.; Chen, J. Q.; Tang, C. H.; Li, C. Water Oxidation on a Mononuclear Manganese Heterogeneous Catalyst. *Nat. Catal.* **2018**, *1*, 870−877.
(227) Zhang, B. X.; Zhang, J. L.; Shi, J. B.; Tan, D. X.; Liu, L. F.; Zhang, F. Y.; Lu, C.; Su, Z. Z.; Tan, X. N.; Cheng, X. Y.; Han, B. X.; Zheng, L. R.; Zhang, J. Manganese Acting as a High-Performance Heterogeneous Electrocatalyst in Carbon Dioxide Reduction. *Nat. Commun.* **2019**, *10*, 2980.
(228) Li, J. Z.; Chen, M. J.; Cullen, D. A.; Hwang, S.; Wang, M. Y.; Li, B. Y.; Liu, K. X.; Karakalos, S.; Lucero, M.; Zhang, H. G.; Lei, C.; Xu, H.; Sterbinsky, G. E.; Feng, Z. X.; Su, D.; More, K. L.; Wang, G. F.; Wang, Z. B.; Wu, G. Atomically Dispersed Manganese Catalysts for Oxygen Reduction in Proton-Exchange Membrane Fuel Cells. *Nat. Catal.* **2018**, *1*, 935−945.
(229) Qin, Y.; Wu, H. H.; Zhang, L. A.; Zhou, X.; Bu, Y. F.; Zhang, W.; Chu, F. Q.; Li, Y. T.; Kong, Y.; Zhang, Q.; Ding, D. B.; Tao, Y. X.; Li, Y. X.; Liu, M. L.; Zeng, X. C. Aluminum and Nitrogen Codoped Graphene: Highly Active and Durable Electrocatalyst for Oxygen Reduction Reaction. *ACS Catal.* **2019**, *9*, 610−619.
(230) Liu, S.; Li, Z.; Wang, C.; Tao, W.; Huang, M.; Zuo, M.; Yang, Y.; Yang, K.; Zhang, L.; Chen, S.; Xu, P.; Chen, Q. Turning Main-Group Element Magnesium into a Highly Active Electrocatalyst for Oxygen Reduction Reaction. *Nat. Commun.* **2020**, *11*, 938.
(231) Wang, J.; Huang, Z. Q.; Liu, W.; Chang, C. R.; Tang, H. L.; Li, Z. J.; Chen, W. X.; Jia, C. J.; Yao, T.; Wei, S. Q.; Wu, Y.; Li, Y. D. Design of N-Coordinated Dual-Metal Sites: A Stable and Active Pt-Free Catalyst for Acidic Oxygen Reduction Reaction. *J. Am. Chem. Soc.* **2017**, *139*, 17281−17284.
(232) Zhang, D. Y.; Chen, W. X.; Li, Z.; Chen, Y. J.; Zheng, L. R.; Gong, Y.; Li, Q. H.; Shen, R. A.; Han, Y. H.; Cheong, W. C.; Gu, L.; Li, Y. D. Isolated Fe and Co Dual Active Sites on Nitrogen-Doped Carbon for a Highly Efficient Oxygen Reduction Reaction. *Chem. Commun.* **2018**, *54*, 4274−4277.
(233) Xiao, M. L.; Zhang, H.; Chen, Y. T.; Zhu, J. B.; Gao, L. Q.; Jin, Z.; Ge, J. J.; Jiang, Z.; Chen, S. L.; Liu, C. P.; Xing, W. Identification of Binuclear Co_2N_5 Active Sites for Oxygen Reduction Reaction with More Than One Magnitude Higher Activity Than Single Atom CoN_4 Site. *Nano Energy* **2018**, *46*, 396−403.
(234) Ye, W.; Chen, S. M.; Lin, Y.; Yang, L.; Chen, S. J.; Zheng, X. S.; Qi, Z. M.; Wang, C. M.; Long, R.; Chen, M.; Zhu, J. F.; Gao, P.; Song, L.; Jiang, J.; Xiong, Y. J. Precisely Tuning the Number of Fe Atoms in Clusters on N-Doped Carbon toward Acidic Oxygen Reduction Reaction. *Chem.* **2019**, *5*, 2865−2878.
(235) Wang, B. W.; Zou, J. X.; Shen, X. C.; Yang, Y. C.; Hu, G. Z.; Li, W.; Peng, Z. M.; Banham, D.; Dong, A. G.; Zhao, D. Y. Nanocrystal Supracrystal-Derived Atomically Dispersed Mn-Fe Catalysts with Enhanced Oxygen Reduction Activity. *Nano Energy* **2019**, *63*, 103851.
(236) Gong, S. P.; Wang, C. L.; Jiang, P.; Hu, L.; Lei, H.; Chen, Q. W. Designing Highly Efficient Dual-Metal Single-Atom Electrocatalysts for the Oxygen Reduction Reaction Inspired by Biological Enzyme Systems. *J. Mater. Chem. A* **2018**, *6*, 13254−13262.
(237) Zhang, L. Z.; Fischer, J. M. T. A.; Jia, Y.; Yan, X. C.; Xu, W.; Wang, X. Y.; Chen, J.; Yang, D. J.; Liu, H. W.; Zhuang, L. Z.; Hankel, M.; Searles, D. J.; Huang, K. K.; Feng, S. H.; Brown, C. L.; Yao, X. D. Coordination of Atomic Co-Pt Coupling Species at Carbon Defects as Active Sites for Oxygen Reduction Reaction. *J. Am. Chem. Soc.* **2018**, *140*, 10757−10763.
(238) Lu, Z. Y.; Wang, B. F.; Hu, Y. F.; Liu, W.; Zhao, Y. F.; Yang, R. O.; Li, Z. P.; Luo, J.; Chi, B.; Jiang, Z.; Li, M. S.; Mu, S. C.; Liao, S. J.; Zhang, J. J.; Sun, X. L. An Isolated Zinc-Cobalt Atomic Pair for Highly Active and Durable Oxygen Reduction. *Angew. Chem., Int. Ed.* **2019**, *58*, 2622−2626.
(239) Liu, D. X.; Wang, B.; Li, H. G.; Huang, S. F.; Liu, M. M.; Wang, J.; Wang, Q. J.; Zhang, J. J.; Zhao, Y. F. Distinguished Zn, Co-N_x-C-S_y Active Sites Confined in Dentric Carbon for Highly Efficient Oxygen Reduction Reaction and Flexible Zn-Air Batteries. *Nano Energy* **2019**, *58*, 277−283.
(240) Zhang, L.; Si, R. T.; Liu, H. S.; Chen, N.; Wang, Q.; Adair, K.; Wang, Z. Q.; Chen, J. T.; Song, Z. X.; Li, J. J.; Banis, M. N.; Li, R. Y.; Sham, T. K.; Gu, M.; Liu, L. M.; Botton, G. A.; Sun, X. L. Atomic Layer Deposited Pt-Ru Dual-Metal Dimers and Identifying Their Active Sites for Hydrogen Evolution Reaction. *Nat. Commun.* **2019**, *10*, 4936.
(241) Han, X. P.; Ling, X. F.; Yu, D. S.; Xie, D. Y.; Li, L. L.; Peng, S. J.; Zhong, C.; Zhao, N. Q.; Deng, Y. D.; Hu, W. B. Atomically Dispersed Binary Co-Ni Sites in Nitrogen-Doped Hollow Carbon Nanocubes for Reversible Oxygen Reduction and Evolution. *Adv. Mater.* **2019**, *31*, 1905622.
(242) Bai, L. C.; Hsu, C. S.; Alexander, D. T. L.; Chen, H. M.; Hu, X. L. A Cobalt-Iron Double-Atom Catalyst for the Oxygen Evolution Reaction. *J. Am. Chem. Soc.* **2019**, *141*, 14190−14199.
(243) Ren, W. H.; Tan, X.; Yang, W. F.; Jia, C.; Xu, S. M.; Wang, K. X.; Smith, S. C.; Zhao, C. Isolated Diatomic Ni-Fe Metal-Nitrogen Sites for Synergistic Electroreduction of CO_2. *Angew. Chem., Int. Ed.* **2019**, *58*, 6972−6976.
(244) Zhu, W.; Zhang, L.; Liu, S.; Li, A.; Yuan, X.; Hu, C.; Zhang, G.; Deng, W.; Zang, K.; Luo, J.; Zhu, Y.; Gu, M.; Zhao, Z.-J.; Gong, J. Enhanced CO_2 Electroreduction on Neighboring Zn/Co Monomers by Electronic Effect. *Angew. Chem., Int. Ed.*, **2020** DOI: 10.1002/anie.201916218.
(245) Lin, L.; Li, H. B.; Yan, C. C.; Li, H. F.; Si, R.; Li, M. R.; Xiao, J. P.; Wang, G. X.; Bao, X. H. Synergistic Catalysis over Iron-Nitrogen Sites Anchored with Cobalt Phthalocyanine for Efficient CO_2 Electroreduction. *Adv. Mater.* **2019**, *31*, 1903470.
(246) Alarawi, A.; Ramalingam, V.; He, J. H. Recent Advances in Emerging Single Atom Confined Two-Dimensional Materials for Water Splitting Applications. *Mater. Today Energy* **2019**, *11*, 1−23.
(247) Gawande, M. B.; Fornasiero, P.; Zboril, R. Carbon-Based Single-Atom Catalysts for Advanced Applications. *ACS Catal.* **2020**, *10*, 2231−2259.
(248) Wang, A. Q.; Li, J.; Zhang, T. Heterogeneous Single-Atom Catalysis. *Nat. Rev. Chem.* **2018**, *2*, 65−81.
(249) Ding, S. P.; Hulsey, M. J.; Perez-Ramirez, J.; Yan, N. Transforming Energy with Single-Atom Catalysts. *Joule* **2019**, *3*, 2897−2929.
(250) Wan, J. W.; Chen, W. X.; Jia, C. Y.; Zheng, L. R.; Dong, J. C.; Zheng, X. S.; Wang, Y.; Yan, W. S.; Chen, C.; Peng, Q.; Wang, D. S.; Li, Y. D. Defect Effects on TiO_2 Nanosheets: Stabilizing Single Atomic Site Au and Promoting Catalytic Properties. *Adv. Mater.* **2018**, *30*, 1705369.
(251) Liu, G. L.; Robertson, A. W.; Li, M. M. J.; Kuo, W. C. H.; Darby, M. T.; Muhieddine, M. H.; Lin, Y. C.; Suenaga, K.; Stamatakis, M.; Warner, J. H.; Tsang, S. C. E. MoS_2 Monolayer Catalyst Doped with Isolated Co Atoms for the Hydrodeoxygenation Reaction. *Nat. Chem.* **2017**, *9*, 810−816.
(252) Hou, C. C.; Zou, L. L.; Sun, L. M.; Zhang, K. X.; Liu, Z.; Li, Y. W.; Li, C. X.; Zou, R. Q.; Yu, J. H.; Xu, Q. Single-Atom Iron Catalysts on Overhang-Eave Carbon Cages for High-Performance Oxygen Reduction Reaction. *Angew. Chem., Int. Ed.* **2020**, *59*, 7384−7389.
(253) Gao, J. J.; Yang, H. B.; Huang, X.; Hung, S. F.; Cai, W. Z.; Jia, C. M.; Miao, S.; Chen, H. M.; Yang, X. F.; Huang, Y. Q.; Zhang, T.; Liu, B. Enabling Direct H_2O_2 Production in Acidic Media through Rational Design of Transition Metal Single Atom Catalyst. *Chem.* **2020**, *6*, 658−674.
(254) Xiao, H.; Shin, H.; Goddard, W. A. Synergy between Fe and Ni in the Optimal Performance of (Ni, Fe)OOH Catalysts for the Oxygen Evolution Reaction. *Proc. Natl. Acad. Sci. U. S. A.* **2018**, *115*, 5872−5877.

https://dx.doi.org/10.1021/acscatal.0c01950
ACS Catal. 2020, 10, 7584−7618